TAMPEREEN TEKNILLINEN YLIOPISTO
TAMPERE UNIVERSITY OF TECHNOLOGY

Anssi Mäkinen

Investigations and Real-Time Testing of Variable Speed Wind Turbine Control during Grid Faults

Julkaisu 1484• Publication 1484

Tampere 2017

Tampereen teknillinen yliopisto. Julkaisu 1484
Tampere University of Technology. Publication 1484

Anssi Mäkinen

Investigations and Real-Time Testing of Variable Speed Wind Turbine Control during Grid Faults

Thesis for the degree of Doctor of Science in Technology to be presented with due permission for public examination and criticism in Rakennustalo Building, Auditorium RG202, at Tampere University of Technology, on the 4th of August 2017, at 12 noon.

Tampereen teknillinen yliopisto - Tampere University of Technology
Tampere 2017

Doctoral candidate: Anssi Mäkinen
Laboratory of Electrical Energy Engineering
Faculty of Computing and Electrical Engineering
Tampere University of Technology
Finland

Supervisors: Teuvo Suntio, Professor
Laboratory of Electrical Energy Engineering
Faculty of Computing and Electrical Engineering
Tampere University of Technology
Finland

Sami Repo, Professor
Laboratory of Electrical Energy Engineering
Faculty of Computing and Electrical Engineering
Tampere University of Technology
Finland

Pre-examiners: Frede Blaabjerg, Professor
Faculty of Engineering and Science, Department of Energy Technology, Power Electronic Systems
Aalborg University
Denmark

Olli Pyrhönen, Professor
Electrical Engineering
Lappeenranta University of Technology
Finland

Opponent: Jorma Kyyrä, Professor
Electrical Engineering and Automation
Aalto University
Finland

ISBN 978-952-15-3978-7 (printed)
ISBN 978-952-15-3981-7 (PDF)
ISSN 1459-2045

Abstract

The amount of wind turbines connected to electricity grid has increased significantly in recent years due to the increased awareness of the environmental impacts of fossil energy sources. The penetration of wind generation has increased in many areas significantly and the power system is becoming more dependent on the operation of wind turbines. The stable operation of the power system must not be endangered due to the connection of wind turbines. Therefore, the power system operators have created grid codes, which determine how the wind turbines should operate during the grid disturbances. For example, the wind turbines should be able to remain in operation during the disturbances in order to prevent cascade tripping of large number of wind turbines. In addition, the wind turbines should be designed to inject reactive power to the grid to support the decreased network voltage.

In this thesis, the operation of variable-speed wind turbines during the grid disturbances is studied. The main focus is on the low voltage ride-through (LVRT) of the full-power converter and doubly fed induction generator (DFIG) wind turbine concepts. Real-time simulators are utilized extensively in the research. The main research areas of this thesis are the operation of wind turbine synchronization during the grid disturbances, the operation of DFIG during symmetrical voltage dips and the feasibility of the constructed real-time simulation environment as well as real-time-simulator-based laboratory test environment for LVRT studies.

It is revealed that the synchronization of the control system has significant impact on the wind turbine performance under the grid disturbances. It is also shown that the incorrect synchronization design may cause the wind turbine to generate DC currents to the AC network during the symmetrical grid voltage dip. The real-time simulation environment, which consists of RTDS and dSPACE real-time simulators, is constructed and its operation is verified against respective simulations carried out with Matlab/Simulink. The environment is used to represent how the reactive power injection of DFIG during the symmetrical voltage dip can be enhanced by using a transient flux compensation control. In addition, it is pointed out that the voltage recovery after the grid fault may be significantly delayed due to the connection of a low-resistance crowbar protection device. Finally, the laboratory test setup consisting of a small-scale wind turbine prototype and RTDS-controlled grid emulator is constructed. The performance of the laboratory setup is analyzed in time and frequency domains and the main performance limitations are revealed.

Preface

The research work was primarly carried out at the Department of Electrical Engineering of Tampere University of Technology (TUT) where I worked from 2008 to 2013. The work was primarly funded by TUT and Fortum Foundation. The grants provided by Fortum foundation, Finnish Foundation for Technology Promotion, Ulla Tuominen Foundation, Kaute Foundation and Finnish Cultural Foundation are greatly appreciated.

I´m grateful to Professors Sami Repo and Teuvo Suntio for their invaluable help and constructive comments that opened my mind and enabled to finalize the manuscript.

I would like to thank the preliminary examiners, Professor Frede Blaabjerg of Aalborg University and Professor Olli Pyrhönen of Lappeenranta University of Technology, for their constructive comments on how to improve the manuscript.

I am thankful to Professor Heikki Tuusa for giving me the opportunity to take part in interesting research projects and international conferences.

I wish to thank Mr. Antti Virtanen, Dr. Panu Lauttamus, Mr. Jarno Alahuhtala, Dr. Perttu Parkatti for lively discussions and their advice. Assistant Professor Tuomas Messo, Dr. Jenni Rekola and Mr. Ontrei Rapala deserve special thanks for their collaboration in the research and friendship. I am also thankful to Mr. Joni Markkula and Dr. Juha Jokipii for friendship during the research. Mr. Pentti Kivinen and Mr. Pekka Nousiainen deserve special thanks for their craftsmanship in building experimental devices. I wish also to thank Mr. Teemu Nevamäki and Mr. Mika Lammi from GE Grid Solutions for giving me the opportunity to have study leave in order to finish this thesis.

Finally, I wish to thank everyone who has supported me during this process.

Tampere 15.04. 2017

Anssi Mäkinen

Contents

Nomenclature

Abbreviations

AC	alternating current
AD	analogue to digital
DA	digital to analogue
dB	decibel
DC	direct current
DDSRF-PLL	decoupled double synchronous reference frame – phase locked loop
DFIG	doubly fed induction generator
DSOGI-FLL	dual second order generalized integrator – frequency locked loop
DSOGI-PLL	dual second order generalized integrator – phase locked loop
dSPACE	real-time simulator
DVR	dynamic voltage restorer
EN	European Norm
EWEA	European Wind Energy Association
FLL	frequency locked loop
FPC	full power converter
FRT	fault ride through
GE	grid emulator
GM	gain margin
GSC	generator-side converter
GTAI	giga-transceiver analogue input
GTAO	giga-transceiver analogue output
GTO	gate turn off thyristor
IGBT	insulated gate bipolar transistor
LCL	inductor – capacitor – inductor
LPF	low pass filter
LVRT	low voltage ride through
MCCF-PLL	multiple complex coefficient filter – phase locked loop
MSOGI-FLL	multiple second order generalized integrator – frequency locked loop
NSC	network-side converter
NF	notch filter
PCC	point of common coupling
PHIL	power hardware-in-the-loop
PI	proportional – integral
PLL	phase locked loop
PM	phase margin

PMSG	permanent magnet synchronous generator
PV	photovoltaic
PWM	pulse width modulation
RMS	root-mean square
RSC	rotor-side converter
RSCAD	software for real time simulator
RTDS	Real Time Digital Simulator
SCIG	squirrel cage induction generator
SDR	series dynamic resistor
SOGI	second order generalized integrator
SRF-PLL	synchronous reference frame – phase locked loop
STATCOM	static synchronous compensator
SVC	static var compensator
SWPWM	space vector pulse width modulation
THD	total harmonic distortion
TUT	Tampere University of Technology
UCTE	Union for the Co-ordination of Transmission of Electricity
UPS	uninterruptible power supply
VDG	voltage dip generator
V-control	closed loop voltage control
VC-control	closed loop cascaded voltage and current control
WRIG	wound rotor induction generator
WRSG	wound rotor synchronous generator
WWEA	World Wind Energy Association

Symbols

A	wind turbine rotor swept area
B	friction loss term, susceptance
c_p	performance coefficient
c_{pmax}	maximum of performance coefficient
C_{dc}	DC-link capacitance
C_f	filter capacitance
duty	duty cycle
e	Neper number
f_{res}	resonant frequency

f_{sw}	switching frequency
$i_{dc,g}$	generator-side DC current
$i_{dc,n}$	network-side DC current
I_f	field excitation current, fundamental frequency current RMS value
i_{grid}	DFIG transformer secondary current
i_{gs}	generator stator current
I_h	harmonic current RMS value
i_{L1}	network-side converter current
i_{L2}	filter network-side inductor current
i_{ms}	stator magnetizing current
I_n	nominal current
i_r	rotor current
i_{rmax}	current capacity of RSC
i_{rtf}	transient rotor current
i_s	stator current
i_{wt}	current source representing generator side converter current
j	complex variable
J	inertia of wind turbine system
k_i	gain of current controller
k_{LF}	loop filter gain
k_{PLL}	gain of PLL
k_q	gain of reactive power controller
k_{SOGI}	gain of second order generalized integrator
k_t	gain of torque controller
k_{udc}	gain of DC-link voltage controller
k_w	gain of speed controller
K_T	constant used in torque control of grid side converter
L	inductance
L_d	direct axis self-inductance
L_{Lf}	sum of filter inductor inductances
L_{ld}	direct axis leakage inductance
L_{lq}	quadrature axis leakage inductance
L_m	magnetizing inductance

L_{md}	direct axis magnetizing inductance
L_{mq}	quadrature axis magnetizing inductance
L_q	quadrature axis self-inductance
L_r	rotor self-inductance
L_{rl}	rotor leakage inductance
L_s	stator self-inductance
L_{sl}	stator leakage inductance
L_1	converter side inductance
L_2	network-side inductance
$L_{\sigma TF}$	transformer short circuit inductance
n	gearbox transmission ratio
N	generator rotor to stator turns ratio
p	generator pole pair
p	instantaneous active power
p_{ac}	active power of AC side
p_{dc}	active power of DC side
p_{gen}	generator active power
p_{net}	instantaneous active power measured from synchronizing point
P_t	wind turbine rotor power
q	instantaneous reactive power, 90 degrees phase shift
qu’	SOGI output voltage in quadrature-phase with input voltage
R	rotor radius
R_{Cf}	filter damping resistance
R_{crow}	crowbar resistance
R_{damp}	damping resistance
R_{dc}	DC-link chopper resistance
R_{Lf}	sum of filter inductors resistance
R_r	rotor resistance
R_s	stator resistance
R_1	resistance of converter-side inductor
R1	crowbar resistance
R_2	resistance of network-side inductor
R2	crowbar resistance
$R_{\sigma TF}$	transformer short circuit resistance

s	Laplace operator
S	apparent power
S_n	nominal apparent power
S1	crowbar switch
S2	crowbar switch
t_e	electromagnetic torque
t_g	mechanical torque
T_i	integration time
T_{i_i}	current controller integration time
T_{i_q}	reactive power controller integration time
T_{i_t}	torque controller integration time
T_{i_udc}	DC-link controller integration time
T_{i_w}	speed controller integration time
T_n	nominal torque
T_{s_i}	sampling time of current controller
T_{s_q}	sampling time of reactive power controller
T_{s_t}	sampling time of torque controller
T_{s_udc}	sampling time of DC-link voltage controller
T_{s_w}	sampling time of speed controller
T_t	anti-windup tracking time constant
u_{a1}	low pass filtered a-phase voltage
u_{cc}	cross-coupling voltage
u_{ctrl}	current controller output voltage
u_{conv}	network-side converter voltage
u_{dc}	DC-link voltage
u_{fC}	voltage over filter capacitor
u_{GE}	grid emulator voltage
u_{gs}	generator stator voltage
u_{inj}	injection voltage
u_{Lf}	voltage over filter inductors
$u_{PCC,CTRL}$	control reference voltage
u_r	rotor voltage

u_s	stator voltage
u_{sync}	synchronizing point voltage
u'	SOGI output voltage in-phase with input voltage
$\hat{u}$	voltage peak value
U	voltage, voltage after decoupling network
U_n	nominal voltage
$\overline{U}$	voltage after low pass filter
$V_{l\text{-}l}$	line-to-line voltage
v_{tip}	blade tip speed
v_w	wind speed
X	reactance
$\lvert i_{L1dmax} \rvert$	maximum NSC d-axis current
$\lvert i_{L1qmax} \rvert$	maximum NSC q-axis current
$\lvert u_{Lmax} \rvert$	maximum voltage over filter inductors
ΔI	difference from nominal current
ΔU	difference from nominal voltage
Δt	time difference
$\Delta\theta_{ua,1}$	angle increment
α	Fortesque operator
β	blade angle
β_{opt}	optimal blade angle
ε	error measure
ε_{FLL}	average of FLL error measures
ε_{SOGI}	SOGI error measure
γ	gain of frequency locked loop
θ	angle
θ_{inj}	injection angle
θ_{re}	rotor electric angle
θ_{sf}	stator flux angle
θ_{sync}	angle of synchronous reference frame
$\theta_{ua,1}$	estimated a-phase angle
$\Delta\theta$	transformer phase shift feedforward angle
λ	tip speed ratio
λ_*	optimal tip speed ratio

π	pi
ρ	air density
σ	leakage factor, leakage
σL_r	rotor transient inductance
ψ	flux linkage
ψ_d	direct axis flux linkage
ψ_{pm}	permanent magnet flux linkage
ψ_q	quadrature axis flux linkage
ψ_r	rotor flux linkage
ψ_{rtf}	transient rotor flux linkage
ψ_s	stator flux linkage
ψ_{stf}	transient stator flux linkage
ω	angular frequency
ω_{ctrl}	loop filter output angular frequency
ω_f	cut-off frequency of low-pass filter
ω_{ff}	feedforward angular frequency
ω_{inj}	injection angular frequency
ω_{ms}	angular frequency of stator flux reference frame
ω_n	undamped natural frequency
ω_r	angular frequency of generator rotor
ω_{re}	electrical angular frequency of generator rotor
ω_{sl}	slip angular frequency
ω_{sync}	angular frequency of synchronous reference frame
ω_t	angular frequency of wind turbine rotor
ω_z	angular frequency of zero
ω'	resonant frequency of frequency locked loop
$\bar{\omega}'$	averaged resonant frequency of frequency locked loop
Γ	normalized gain of frequency locked loop
ς	damping factor
φ	initial angle

Subscripts

a	phase a
ac	alternating current
b	phase b
c	phase c
cw	refers to wire capacitive susceptance
d	refers to direct axis
dc	direct current
grid	refers to grid
load	refers to load
lw	refers to wire inductive reactance
meas	measured value
peak	peak value
q	refers to quadrature axis
rms	root-mean square
rw	refers to wire resistance
RTDS	refers to RTDS reference
w	refers to wire
x	real axis component in stator flux reference frame
y	imaginary axis component in stator flux reference frame
α	real component of stationary reference frame
β	imaginary component of stationary reference frame
+	positive sequence reference frame
-	negative sequence reference frame

Superscripts

*	reference signal
‘	reduced to stator
g	refers to general reference frame, refers to grid
n	refers to order number
r	refers to rotor reference frame
s	refers to stator reference frame
sψ	stator flux reference frame
+	positive sequence
-	negative sequence

Notations

Im	imaginary component
Int	interrupt signal
Re	real component
TF	transformer
λ_i	equation related to tip speed ratio

1. Introduction

Global warming, air pollution and upcoming shortage of fossil energy resources are the key factors, which promote the generation of electrical energy from renewables such as wind or solar. As a result, the amount of wind turbine installations has increased rapidly in recent years. According to World Wind Energy Association (WWEA), global wind power capacity reached 371.559 GW at the end of 2014 from which 52.654 GW was installed during 2014. This capacity generates approximately 800 TWh/a, which is more than 4% of global electricity demand. It is fair to say that the wind energy business is global as the number of countries using wind energy reached 105 in 2014. WWEA has predicted that the global wind power capacity will increase further in future: in 2020, the capacity is expected to be approximately 700 GW, and the capacity of 2000 GW will be reached by 2030. [1]

As a result of the technology development in recent years, the size of individual turbines has increased: a nominal power of a state of the art wind turbine in 1989 was 300 kW with rotor diameter of 30 meter. [2] After ten years, many manufacturers provided 2 MW wind turbines, whose rotor diameter was increased to around 80 meters. Nowadays, wind turbines with 7-8 MW power range are available on market with rotor diameter reaching 160 meters. [3-4] Accoring to European Wind Energy Association (EWEA), 15 MW wind turbines are in planning stage and 20 MW turbines are expected in the near future. [5-6]

Utilized wind turbine concepts has also evolved: in 1980s, the mainstream concept, depicted in Fig. 1.1, exploited a squirrel cage induction generator (SCIG), which is directly connected to the grid through a step-up transformer. [4] The concept is also called as a fixed speed concept, because the generator rotational frequency deviates from the network voltage frequency only by the amount of a slip frequency. Due to the direct connection of the generator inductive stator to the grid, the generator consumes reactive power. In order to improve power factor, the capacitor banks are connected in parallel with the generator. A soft starter is used to decrease the inrush current of the generator during start-up. Benefits of the concept are low price and simple structure. However, significant mechanical stresses experienced by the wind turbine components and high flicker

emissions motivated the manufacturers to develop wind turbine concepts with the capability of variable speed operation. [2]

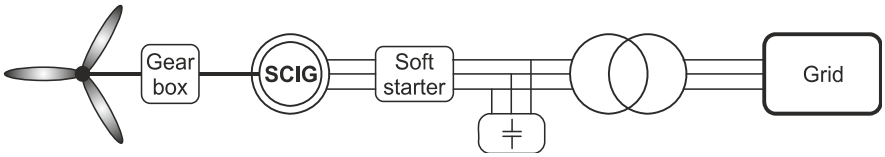

Fig. 1.1. Fixed speed wind turbine concept with SCIG.

The limited variable speed wind turbine concept, shown in Fig. 1.2, was introduced in 1990s. Utilization of a wound rotor induction generator (WRIG) and a controllable rotor resistance enabled a speed range of approximately 0-10% above the synchronous speed. The mechanical stresses and flicker emissions are decreased, because part of the fluctuating power from wind is absorbed by the inertial mass of the wind turbine rotor. However, the efficiency of the concept is decreased as the generator slip is increased because the variable speed operation is achieved by dissipating energy in the rotor resistance. [7]

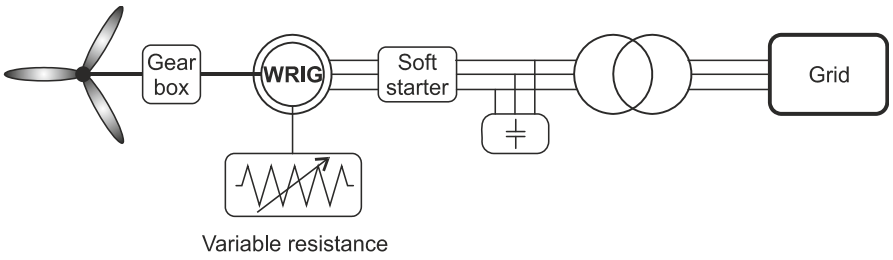

Fig. 1.2. Limited variable speed wind turbine concept with WRIG.

Next step in the development of the mainstream wind turbine technology was an addition of back-to-back frequency converter to the rotor circuit as shown in Fig. 1.3. In this so called a doubly fed induction generator (DFIG) wind turbine concept, the stator of the WRIG is directly connected to the grid while the rotor is connected to the rotor-side converter (RSC). RSC is used to control the slip and the reactive power output of the generator. A typical slip range is approximately from -0.3 to +0.3. A network-side converter (NSC) is connected to the generator stator circuit or to a tertiary winding of the wind turbine transformer. The main task of NSC is to maintain constant DC-link voltage. In addition, NSC can be used to provide reactive power during a grid voltage dip in order to support the grid voltage. This wind turbine concept is economically attractive, because the frequency converter is rated approximately to 30% of the wind turbine nominal power. [4, 8] This implies small converter and filter sizes as well as losses. Need of slip rings and

complex control and protection of the wind turbine during grid faults are the main drawbacks.

A market share of the DFIG concept in 2011 was approximately 50% making the concept to be a market leader. [6, 9] However, an inevitable use of a gearbox, slip rings and brushes require frequent maintenance making DFIG to be rather inconvenient for logistically hard wind turbine applications such as offshore wind parks. [10]

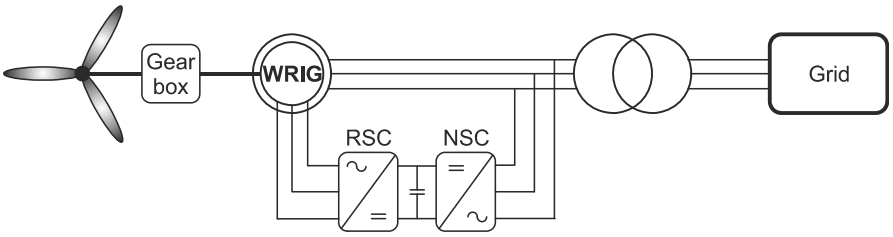

Fig. 1.3. DFIG wind turbine concept.

A full power converter (FPC) wind turbine concept is shown in Fig. 1.4. A generator-side converter (GSC) controls the rotational frequency of the generator, which can be either a wound rotor synchronous generator (WRSG), a permanent magnet synchronous generator (PMSG) or SCIG. NSC maintains the constant DC-link voltage and controls the reactive power output of the wind turbine. All generated power is transferred through the frequency converter. Thus, the converter needs to be rated to a whole wind turbine capacity, which causes increased size, losses and costs compared to DFIG design. However, the elimination of the slip rings and improved grid support capability are advantages. It is also possible to use a multipole generator, which decreases the size of the gearbox or even eliminates the need of it. Due to the location of the frequency converter, the stator of the generator is decoupled from the grid. This is a significant benefit considering the operation during grid faults. The better controllability, increased reliability and compliance to the more demanding grid codes in future are the key factors, why it is anticipated that the FPC concept will take over the wind turbine markets in the future. [4, 6]

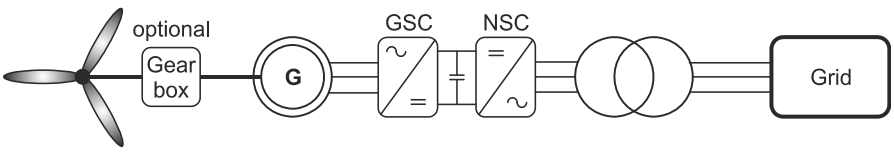

Fig. 1.4. FPC wind turbine concept.

1.1 Background

1.1.1 Grid codes

In the beginning of the utilization of wind energy for electricity generation, the number of wind turbines connected to the grid was small. Due to a low penetration of the wind generation, a sudden loss of an individual wind turbine or even wind farm did not endanger the power system stability. In other words, the loss of wind generation was compensated by increasing the active power generation of other generators in the grid. As mentioned earlier, the wind turbines during the early stages of wind power utilization consisted of SCIGs connected directly to the grid. During a grid fault, it was reasonable to disconnect the wind turbine from the grid in order to protect the wind turbine prime mover and to avoid the grid voltage instability during voltage recovery caused by the induction machines. [11]

As the penetration of the wind generation increases in many areas to a significant level, the power system becomes more dependent on the operation of the wind turbines. If a cluster of wind turbines operating at nominal power is suddenly disconnected from the grid as a result of the grid fault, the loss of active power generation may be significant enough to endanger the power system stability. This was seen on 4th of November 2006 in the UCTE disturbance, which began from overloading of transmission line and escalated due to the sudden disconnection of significant amount of distributed generation including wind generation. At the end of the day, more than 15 million European households suffered from the interruption of electricity supply. [12-13]

The increased wind penetration should not endanger the power system stability. Thus, the power system operators of different countries have created grid codes, which determine how wind turbines should operate during the steady state and grid disturbances. As an example of the operation during the disturbance, the grid code of E.ON Netz regarding the symmetrical voltage dips are illustrated in Fig. 1.5a. [14] The wind turbines are not allowed to disconnect if the grid voltage exceeds a pre-defined limit in order to prevent the cascade tripping of large number of wind turbines. In other words, the wind turbines should have a low voltage ride-through (LVRT) capability. In addition, it is required that the wind turbines should be able to inject reactive current during the fault in order to support the violated grid voltage. The wind turbines should inject nominal reactive current if the voltage is lower than 50% of the nominal value as can be seen from Fig. 1.5b. [14] In addition, the grid codes typically instructs how the wind turbine should contribute to the power system voltage and frequency control. [2,15-19]

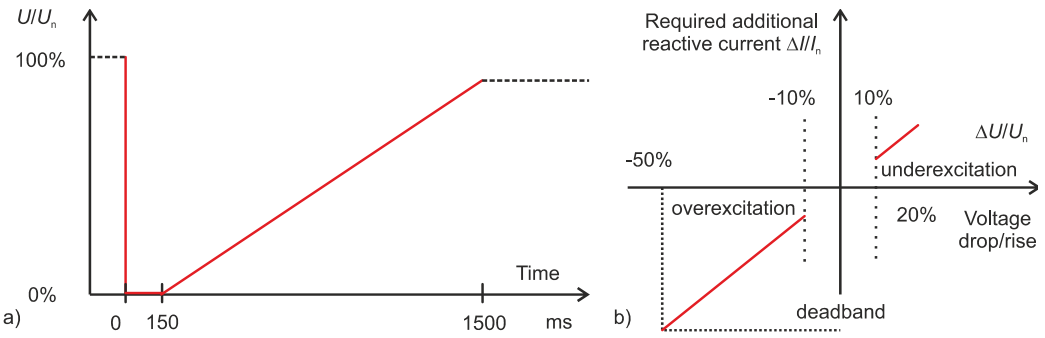

Fig. 1.5. E.ON Nezt grid code: a) LVRT requirement, b) reactive current injection / absorption during abnormal network voltage.

1.1.2 Low voltage ride-through of variable speed wind turbines

In this thesis, LVRT and reactive power injection capability is assessed for the DFIG and FPC wind turbine concepts. The response to the grid voltage dip is different between the concepts. In FPC design, the generator is hidden behind the frequency converter so the generator itself does not directly recognize the dip. However, in case of DFIG, the direct connection of the generator stator to the grid complicates the controlling of DFIG during the grid faults.

1.1.2.1 FPC wind turbine

When the FPC wind turbine is subjected to the deep grid voltage dip, the active power generated from the wind cannot be transferred into the grid as a whole. As a consequence, the generated power, which is not transferred into the grid, is stored into the DC-link of the frequency converter causing the DC-link voltage to increase. This may damage the DC-link capacitor or converter switching components without any countermeasures.

One possible solution to avoid the damage is the use of a very large capacitor or to install a battery-based uninterruptible power supply (UPS) in the DC-link, which absorbs the imbalance energy. However, an energy storage that should be installed in megawatt class wind turbine would be extremely large making the solution to be impractical and expensive. [20-24] It is also possible to oversize the NSC in order to increase the current and power transfer capability to the grid. However, this would increase costs of the converter and still the expensive energy storage needs to be installed to the DC-link for the case of a very deep voltage dip. [20-21, 25] Thus, a typical way to obtain the LVRT capability is to install a braking chopper to the DC-link. When the DC-link voltage exceeds a pre-defined limit, the braking chopper is activated and the excess energy is dissipated in a chopper resistance. [25-27] The drawback of this solution is the generated heat during a deep and long lasting voltage dip, especially, in case of megawatt class wind turbines. [20]

The LVRT capability is enhanced if a combination of the braking chopper, an intelligent GSC control and a pitch control is used. [25, 28-29] When the voltage dip is sensed, GSC may reduce the generator active current reference (generator torque) or set it to zero. [30] When the generator electrical torque is reduced, more kinetic energy from the wind is stored into the rotating mass of a wind turbine rotor causing the rotor to accelerate. The duration of the voltage dip is usually in the range of some hundreds of milliseconds. Because the inertia of the rotor is significant, the speed of the rotor does not increase notably. [31] However, during long lasting voltage dips, the pitch control can be used to reduce the power extracted from the wind in order to avoid rotor over-speeding. After the voltage dip is detected, the relatively slow pitch control can be turned into an emergency mode, where the rate of increase of the pitch angle is maximized [26]. Based on the discussion above, it can be stated that the FPC wind turbine can be protected from the detrimental effects, which appear due to the grid voltage dip. [29]

The grid codes regarding the reactive power injection during the voltage dip can be fulfilled by controlling the NSC reactive current reference to capacitive. The reactive current injection can be started as soon as the decrement of the grid voltage or its positive sequence component is detected. In addition, the capability of NSC to generate positive sequence reactive currents is dependent on how accurately NSC is able to extract the angle of the positive sequence voltage component. The detection of the positive sequence voltage magnitude and angle is done in the synchronization system of NSC. Thus, it can be stated that the dynamic response and quality of the generated currents during the grid disturbances are greatly dependent on the synchronization method used by the control system of NSC. [32-33]

The target of the synchronization system is the fast detection of the magnitude and angle of the fundamental frequency positive sequence grid component. Because the positive sequence component is a symmetrical component, the control reference frame rotates with a constant frequency. A simple way to determine the phase angle of the grid voltage is based on observing zero crossings of the grid voltage. A drawback of this synchronization method is that it cannot follow changes in the grid voltage angle in between the zero crossings. As a result, the phase tracking is slow leading to poor dynamic response. [34-35] More popular method is a synchronous reference frame – phase locked loop (SRF-PLL), where a frequency adaptive phase angle is attained utilizing a Park-transformation and loop filtering in a synchronous reference frame. A drawback of this method is the poor performance under the grid voltage harmonics and asymmetry, if high loop filter gain is selected to obtain satisfactory dynamic performance. [33, 36-37]

More advanced synchronization methods include specific circuit for cancelling the impact of negative sequence voltage from the synchronizing angle and magnitude. In a decoupled

double synchronous reference frame – phase locked loop (DDSRF-PLL), a decoupling network is used to cancel the impact of the negative sequence component from the positive sequence component estimation. [38] A dual second order generalized integrator – PLL (DSOGI-PLL) utilizes adaptive bandpass filtering and the theory of instantaneous symmetrical components to provide the positive sequence component. [39] Complex filters provide cancelling of selected harmonic components in addition to the negative sequence fundamental component from the grid voltage in a multiple complex coefficient filter PLL (MCCF-PLL). [40] The synchronization to the positive sequence grid voltage component is done by using SRF-PLL in the above mentioned methods. [38-40]. The synchronization methods using complex PLL and complex coefficient filters are presented in [41] and [42].

In the SOGI-based synchronization methods, the tuning of the bandpass filter resonant frequency can be carried out with a frequency locked loop (FLL) instead of PLL. The grid frequency is more stable variable than the grid angle. Therefore, the transient operation of FLL is smoother in nature compared to PLL. Typical FLL-based grid synchronizing methods are DSOGI-FLL [43-44] and multiple SOGI-FLL (MSOGI-FLL) [45]. MSOGI-FLL can remove specific harmonics in addition to the negative sequence fundamental component from the grid voltage.

1.1.2.2 DFIG wind turbine

The LVRT capability is more challenging task for the DFIG wind turbine than for the FPC wind turbine. The reasons are the lower rated converters and the direct connection of the generator stator to the grid. The voltage dip in the generator stator terminals causes high voltages to a rotor circuit due to a stator transient or natural flux as will be explained in Section 4.4.1. [46] The rotor voltages may exceed a level, where the rotor currents cannot be controlled and limited by using RSC. Thus, an insulated gate bipolar transistor (IGBT) based switches of RSC can be damaged due to over-currents caused by the voltage dip without any protection measures. [46-48]

One possibility to enhance the LVRT capability is to oversize the RSC voltage and current ratings. However, this solution is contradictive to the main benefit of DFIG, which is the small sized converters. [49] During a severe voltage dip, the RSC switches are typically blocked and an external resistor is connected to the rotor circuit in order to decrease the rotor currents and protect the converter. [48] This protection approach is known as a crowbar protection.

The crowbar protection can be categorized into passive and active methods. The passive crowbar is based on thyristor switches as shown in Fig. 1.6a. The crowbar protection is activated, when the rotor currents or the DC-link voltage exceed the trigger level by turning

on the thyristors. After the firing of the thyristors, DFIG continues its operation as an induction generator with the increased rotor resistance. The crowbar remains connected as long as the main circuit breaker disconnects DFIG from the grid. [50] The disconnection of the wind turbine in case of the grid fault is significant disadvantage and against the grid codes.

The active crowbar shown in Fig. 1.6b utilizes typically IGBT [51] or gate turn-off (GTO) [52] thyristor switches in order to make the crowbar to be controllable. [53] The crowbar protection can be implemented also by utilizing antiparallel thyristors with the external resistance as shown in Fig. 1.6c. [54] The main disadvantage of the crowbar protection is the inability to control RSC during the operation time of the crowbar activation. [55-57] However, the active crowbar can be disconnected after the rotor currents and voltages are reduced enough to allow the current control by using RSC. Thus, the wind turbine is able to ride-through the fault without disconnection. In addition, it can inject reactive current to the network after the crowbar deactivation. NSC can controlled to inject reactive current to the network during the whole time of the fault.

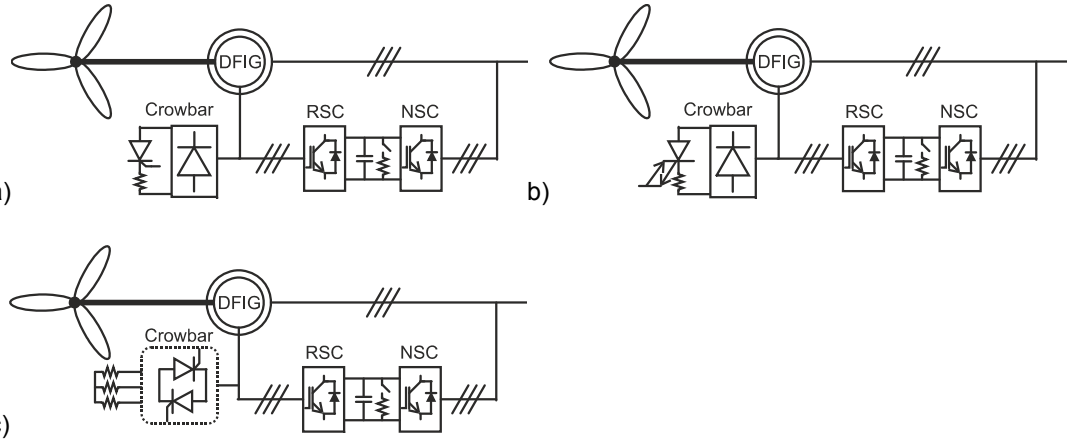

Fig. 1.6. DFIG wind turbine: a) passive crowbar protection, b) active crowbar protection with diode bridge, c) active crowbar protection with antiparallel thyristors.

An alternative DFIG protection method contains only the DC-link braking chopper. [49, 58] The rotor currents are allowed to flow to the DC-link during the voltage dip and the chopper prevents the DC-link overvoltage. In order to handle the increased rotor currents, anti-parallel diodes of RSC may need to be oversized. [49] A LVRT method can also be based on a series dynamic resistor (SDR) installed in the rotor circuit. [57] A drawback of the solution is the losses associated to a power electronic bypass switch. [57] In a LVRT method proposed in [59], the crowbar is connected after the voltage dip, while RSC is connected in parallel with NSC. Hence, both RSC and NSC can inject reactive current

during the voltage dip. A drawback of this solution is the uncontrollability of the wind turbine due to the crowbar connection.

A more expensive and complex solution to attain the LVRT capability is based on dynamic voltage restorer (DVR), which is a voltage source converter connected in series with the grid. [60] Also a shunt reactive power compensator such as a static synchronous compensator (STATCOM) or a static var compensator (SVC) can be used to minimize the voltage drop at the generator stator terminals. Thereby, the operation of DFIG during the voltage dip is enhanced. [61-62]

It is stated in [56] and [63] that the LVRT capability can be obtained using intelligent control strategies without using any external protection circuits such as the crowbar or DC-link chopper. In both references, the measured stator currents are set as references to a rotor current controller. It is reported that the stator and rotor windings overcurrents are prevented with the control method. However, a stator to rotor turns ratio in the generator in the experimental setup is one in [56], which makes the rotor voltages low enough to allow the current control of the RSC during the fault. It is concluded in [63] that RSC may not be able to control the rotor currents during the voltage dip, if the stator to rotor turns ratio is selected to 1/3, which is typical ratio in wind turbines due to the desire of low losses. Generally, it seems to be hard to implement a LVRT strategy for DFIG without additional resistance (e.g. crowbar or DC-link chopper) with normally rated RSC. [55]

The operation of DFIG during deep unsymmetrical voltage dip is challenging due to high rotor voltages caused by the negative sequence grid voltage component. The high rotor voltages may prevent the current control of RSC. Taking into account that the negative sequence voltage remains in the network throughout the fault duration the crowbar may need to be connected and, as a consequence, RSC may need to be blocked for the whole fault period. [64-65] Thus, the generator cannot be controlled during the severe unsymmetrical fault.

1.1.3 Utilization of real-time simulators in wind turbine LVRT studies

Understanding interactions between wind turbines and grid becomes essential as the number of installed wind turbines increases. [7, 66-68] The interactions appear in wide variety of time scales. Switching of the wind turbine converters appears in the time scale expressed using microseconds. On the other hand, the impact of fluctuating wind speed on the power system operation and control appears on the time scale from seconds to hours. If a transient offline simulator such as Matlab Simulink or PSCAD is used, the simulation of the interactions may become very time consuming. The simulation time can be decreased if the accuracy of a wind turbine model is decreased or a network model

representation is reduced. However, the decrement of the modeling accuracy may impair the utilization of the model to control system design or power system analysis. [69]

Real-time simulators such as Real Time Digital Simulator (RTDS) or dSPACE enable fast simulation of complex models in real-time thanks to their great computational power. A significant benefit of using the real-time simulators is the possibility to use real devices such as protection relays [29, 70-71], controllers [72-74], electric machines [75], power sources [76], energy storages [69] or real-time measurements as a part of the simulations [77]. RTDS is an electromagnetic transient simulator specifically designed for the power system simulation. It is utilized in wind turbine related studies mainly due to decreased simulation time [61, 78-80]. dSPACE is typically used as a simulation platform for control system implementations. [81-85] It runs automatically code based on Matlab Simulink model and provides a possibility for online parameter changing and monitoring.

The simulation step size in real-time simulations is fixed and the simulation accuracy increases as the step size decreases. However, if the complexity of the simulation model increases significantly, the simulation step size may need to be increased in order to avoid overrun, where the actual execution of the model exceeds the simulation step size. This may force to decrease the complexity and size of the model. However, the accuracy and size of the real-time simulated model can be increased significantly if an interconnection of real-time simulators is used. [66, 69, 86] For example, a combined real-time simulation environment constructed using RTDS and dSPACE enables simultaneous use of accurate grid and wind turbine or active power filter models due to the sharing of the computational power between two simulators. [29, 66-67, 86-88] The extend of the grid model depends on the number of RTDS processor cards and computational power of them, while the complexity of the wind turbine or filter model is dependent on the computational power of dSPACE.

1.1.4 Testing of wind turbine LVRT

Control features of wind turbines during the grid disturbances are typically designed by using offline or real-time simulations. However, the practical operation of the control functions should be comprehensively tested in a laboratory before the installation of the wind turbine [89]. For that purpose, a voltage dip generator (VDG) to operate as a grid emulator (GE) is needed to generate faulted voltages to a point of common coupling (PCC) of the laboratory wind turbine.

Considering only voltage dips, four different types of VDGs shown in Fig. 1.7 are typically used in testing of the LVRT capability of wind turbines. The VDG types are implemented by using a generator, a shunt impedance, a transformer or a power electronic converter

[90]. The main drawback of the generator-based VDG is the possibility to generate only symmetrical dips. In addition, the rate of decrease of voltage is too slow to represent realistically the grid voltage dip. The shunt-impedance-based VDG can be used to generate different kinds of voltage dips (1-phase, 2-phase, 3-phase). Tests of megawatt class DFIGs with the shunt impedance VDG are reported in [91-93]. A drawback of the shunt impedance VDG is the need of adjustable inductors and a lack of controllable generation of harmonics. The transformer-based VDG provides no savings in the amount of power electronic switches compared to the converter-based solution. The converter-based VDG provides possibility to emulate symmetrical and unsymmetrical voltage dips, voltage harmonics as well as voltage swells and flicker. In addition, only the converter-based emulator is able to generate rapid frequency deviations. [90]

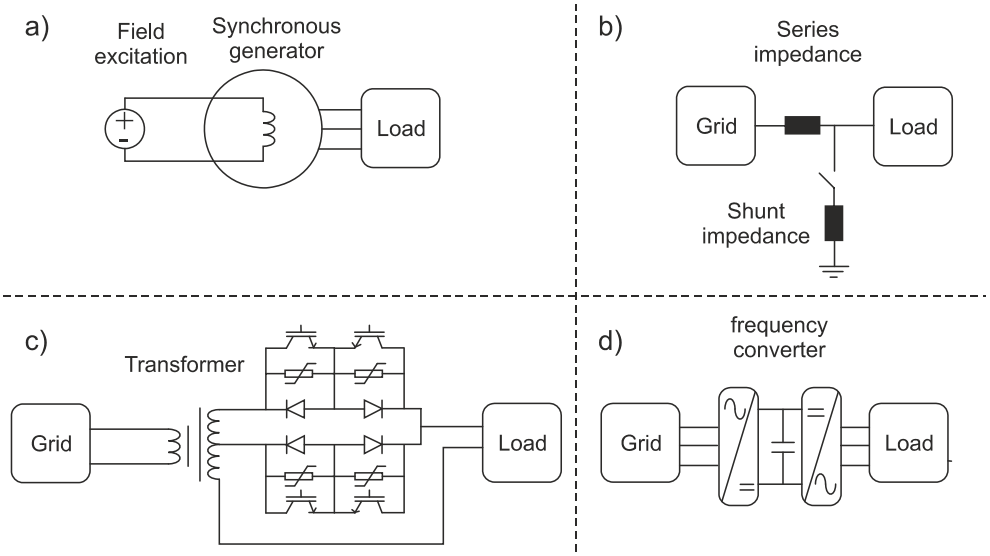

Fig. 1.7. Voltage dip generators: a) generator based, b) impedance based, c) transformer based, d) converter based. [89-90]

Although the performance of protection and control functions during the voltage dips can be tested from the wind turbine viewpoint, the impacts of the wind turbine operation to the power system operation cannot be investigated by using only the aforementioned VDGs. However, these impacts can be analyzed if, for example, a power system real-time simulator is included into the laboratory test setup. This type of environment, where real power is transferred through a tested device interconnected to the real-time simulation, is called as a power hardware-in-the-loop (PHIL) simulation environment. [94-95]

The PHIL test environment provides significant benefits from wind turbine manufacturer point of view. It is possible to test the grid code compliance and new or project specific control features by using a replica hardware of a nacelle of the wind turbine with increased

amount of measurements, which are useful in a performance validation process. In addition, weather and grid conditions do not have impact on the tests, which is often not the case in the tests carried out in-field. Furthermore, the measurements carried out by using the PHIL test bench are reproducible in contrast to field tests due to pre-selectable initial conditions. [96]

1.2 Research scope

This thesis focuses on the operation of the FPC and DFIG wind turbines during the grid disturbances. One of the main objectives is the extensive utilization of the real-time simulators in the research. The utilization is carried out in two stages. In the first stage, a real-time simulation environment is constructed at TUT laboratory by interconnecting RTDS and dSPACE simulators. In the second stage, the real-time environment is extended to PHIL environment, which includes a wind turbine laboratory prototype and converter-based GE.

Due to tremendous number of publications in the area of fault ride-through (FRT) of the variable speed wind turbines, the scope of this thesis is restricted to specific contributing investigations in the following research areas:

- FPC wind turbine LVRT and grid synchronization
- DFIG wind turbine LVRT
- real-time simulation environment for wind turbine LVRT studies
- RTDS-driven PHIL environment for wind turbine FRT studies

As mentioned above, the DFIG crowbar protection needs to be connected for a whole fault duration under severe unsymmetrical voltage dip. Because DFIG cannot be controlled during the time of crowbar connection, this subject is excluded from the scope of this thesis.

1.3 Research motivation and objective

FPC wind turbine LVRT and grid synchronization

The FPC wind turbine FRT capability has been investigated comprehensively in a literature. [26-27, 29, 33, 97] Due to the decoupling between the generator stator and the grid, this capability is reported to be straightforward to implement. [29] The performance of the wind turbine during the grid disturbances and the capability to give the voltage support by

injecting reactive current to the network is strongly related to the performance of the synchronization of the NSC control system. For example, if the synchronization is tuned to have a slow response, NSC is able to generate sinusoidal currents also during the grid disturbances and under network voltage harmonics. However, too slow operation has adverse effects. At first, the injection of the reactive power is delayed after the voltage dip due to the slow detection of the magnitude of the grid voltage positive sequence component. Secondly, the removal of the reactive power injection during a voltage recovery is delayed, which may cause unnecessary grid over-voltages especially in weak and light loaded networks. [98] Thus, it can be concluded that correct tuning of the synchronization is of great importance and it is one of the main objectives of this thesis.

A comparison of different synchronization methods has been carried out without clear information about the tuning parameter selection in [99] and [100] or with certain justified tuning parameters in [33]. The impact of the parameter selection is investigated more comprehensively in [41]. In the scope of this thesis, the objective is to analyze the performance of SRF-PLL, DDSRF-PLL and DSOGI-FLL during symmetrical and unsymmetrical voltage dips as well as under the presence of network voltage harmonics. Other NSC synchronization methods are excluded from the scope of this thesis. The research question is how the tuning of the synchronization methods affects the waveform of the output currents during the disturbances. This subject is analyzed in Investigation 2.

A structure and an operation principle of DDSRF-PLL are presented in detail in [38, 99-100]. A more advanced version of DDSRF-PLL is presented in [33] where the impact of a network voltage magnitude on the PLL control bandwidth is eliminated by using a gain normalization. This thesis extends the analysis of the advanced DDSRF-PLL structure. It is revealed that the synchronization method may operate hazardously, when it is subjected to a deep symmetrical voltage dip with certain tuning parameters. The malfunction is analyzed in detail and a solution to counteract the problem is provided in Investigation 1.

DFIG wind turbine LVRT

The operation of DFIG during the grid faults is different compared to FPC design due to the direct coupling of the generator stator to the grid. The requirements related to operation of NSC synchronization remain also for the DFIG wind turbine. However, the interactions between the grid voltage and WRIG characterize the DFIG response to the grid voltage dip significantly.

During the crowbar connection after the symmetrical voltage dip, the operation of WRIG cannot be controlled and it continues its operation as an induction machine with the increased rotor resistance. The active and reactive powers of the induction generator

depend on rotor speed, terminal voltage and rotor (crowbar) resistance. The rotor resistance determines the steepness of the generator slip-active power and slip-reactive power curves. [48] The smaller the resistance is the steeper are the curves. Thus, selection of small crowbar resistance leads to high rotor and grid currents, torque stresses and active power spikes as a result of the voltage dip. However, if too high crowbar resistance is selected the rotor voltages may become high enough to damage the rotor winding insulation. Furthermore, the rotor currents start to flow to the DC-link of the frequency converter through antiparallel diodes if the rotor voltages exceed the DC-link voltage. [101] This may damage the DC-link capacitor without any countermeasures.

The proper crowbar resistance selection depends on the generator parameters, and therefore, generic optimal resistance value cannot be defined. However, a range of proposed resistances in a literature is very wide. For example, the crowbar resistances sized in the middle of values 0.05 pu - 0.5 pu are reported in [48, 59, 101-102]. Crowbar resistances from 1 to 20 times the rotor resistance are proposed in [103-104].

The rotor currents tend to rise also during the voltage recovery which, depending on the protection strategy, may re-activate the crowbar protection. [48, 55, 105] If a small crowbar resistance is selected, the absorbed reactive current to magnetize the generator during the voltage recovery is significant due to the steep slip-reactive power curve. This may delay the voltage recovery and cause even a short-term voltage instability, especially in weak networks, if no reactive power sources such as STATCOM or SVC is installed near the wind turbine or wind farm. [11, 106] Thus, it is highlighted in [107] that the crowbar activation during the voltage recovery represents a worst case scenario from the grid viewpoint and it should be avoided. In a LVRT method proposed in [107], the crowbar is used in protection against the over-currents during the voltage dip but the DC-link chopper is used during the voltage recovery.

The operation of the active crowbar equipped DFIG during the network voltage recovery has received only limited amount of attention in literature [107]. Thus, the issue with the impact of crowbar resistance selection is analyzed in Investigation 5. In the Investigation 5, the aim is to find a solution to allow the crowbar connection also during the voltage recovery.

The grid codes require that wind turbines should generate reactive current to support the network voltage during the voltage dip. This is possible only after disconnection of the active crowbar. Whether or not DFIG is able to generate the maximum available reactive current during the voltage dip depends on the control strategy of RSC during the fault. [108] The idea of generating a demagnetizing current using RSC during the fault to oppose the stator transient flux, which is the root cause of the rotor overcurrent problem, was

originally presented in [109]. It is pointed out that the DFIG is able to ride through the symmetrical fault without the need of the crowbar activation. However, due to the fact that the rotor voltages and currents are very high, when the voltage dip occurs with worst case initial conditions, RSC needs to be considerably overrated. Therefore, this solution is not typically applicable. The idea of generating demagnetizing currents using RSC was further developed in [55], where the LVRT strategy contains two stages, which are the active crowbar protection and the demagnetizing current generation.

In this thesis, the impact of the transient flux during the symmetrical voltage dip on DFIG operation and the two stage LVRT strategy is analyzed in detail. New way to extract the transient stator flux component is proposed, which utilizes theory from the NSC synchronization section of this thesis. The LVRT method, which is capable to inject maximum available reactive current during the symmetrical fault, is presented in Investigation 4.

Real-time simulation environment for wind turbine LVRT studies

One objective of this thesis is the utilization of real-time simulators in the wind turbine LVRT research. A combined simulation environment, which contains RTDS for the power system simulation and dSPACE for the wind turbine model simulation, is constructed and extensively utilized in this thesis. The combined real-time simulation environment is beneficial from the wind turbine LVRT viewpoint, because both the grid and wind turbine operation can be studied with accurate and flexible models in reasonable time.

Similar environment was first time used in the study of the grid impacts of a FPC wind turbine in [66]. However, the simulation results were presented and analyzed only from the power system point of view. In addition, no verification of the real-time model was presented in [66]. The aim of this thesis is to extent the analysis to cover also the behavior of the wind turbine in addition to the power system operation. The verification of the environment is carried out in Investigation 3. The real-time environment is also implemented for DFIG at the first time to the best of author's knowledge in this thesis. The environment is utilized in the DFIG LVRT studies in Investigations 4 and 5.

RTDS-controlled PHIL environment for wind turbine FRT studies

In several PHIL applications [76, 96, 110-111], the simulation of the power system is carried out by using RTDS. The RTDS-simulated PCC voltages can be generated by using a motor-generator combination, whose drawback is a slow response for the wind turbine transient operation studies. [110] The PHIL system for testing the operation of a photovoltaic (PV) inverter is presented in [76]. However, the presented GE was not able to generate unbalanced voltages. The PHIL environment can be constructed also at

megawatt power level. [96, 111] In Ref. [111], the PCC voltages are not controlled, which means that the measured voltages do not follow the references as the operation point of the wind turbine changes. Thus, the test setup is effective only for the wind turbine control functions tests, but the impact of wind turbine to the grid operation cannot be reliably studied. The operation point of the tested system can be taken into account if the GE output voltages are closed-loop controlled [112]. However, the performance of the GE is investigated by using a purely resistive load in [112].

In this thesis, the RTDS/dSPACE –environment is extended to PHIL environment, where FPC-based GE gets its reference voltages from RTDS and the small scale wind turbine laboratory prototype is controlled by using dSPACE. An inexpensive commercial frequency converter is configured to operate as GE. The grid emulator controls the prototype wind turbine PCC voltages based on the RTDS simulation. Simultaneously, the PCC currents are measured and transferred to the RTDS simulation. The impact of different network topologies, parameters and disturbances on the operation of the prototype can be effectively studied. In addition, the impact of the wind turbine operation on the network operation can be similarly investigated. The research question is how well GE can generate the PCC voltages determined by the RTDS model. The performance of GE during the steady state is compared in open- and closed-loop voltage-control modes by using frequency response measurements. Measurement of the frequency response of the positive and negative sequence voltage components is analyzed in Investigation 6. Time domain measurements under network symmetrical and unsymmetrical voltage dips are carried out to assess the transient performance of GE in Investigation 7.

1.4 Scientific contributions

The main scientific contributions of this thesis can be summarized as follows:

1. A performance comparison of three synchronization methods during the grid disturbances. The synchronization methods under investigations are SRF-PLL, DDSRF-PLL and DSOGI-FLL. The impact of network voltage symmetrical and unsymmetrical dips as well as voltage harmonics to the synchronization performance is analyzed with respect to controller tuning. In addition, it is shown how the FPC wind turbine may generate DC-currents during the symmetrical voltage dip if the synchronization is improperly designed. Re-design of the synchronization system to avoid the DC current generation is presented.
2. Development of the real-time simulation environment for wind turbine and grid interactions studies. The environment consists of RTDS and dSPACE real-time

simulators. The performance of the real-time environment is verified against offline simulations carried out using Matlab Simulink. With the environment, the operation of the enhanced on-fault control of the DFIG wind turbine is tested with decreased simulation time. It is shown that the transient flux compensation control enables the maximum reactive power support by the wind turbine without a fear of repetitive crowbar activation. In addition, the quality of a generated power improves. Furthermore, it is revealed that the utilization of too small crowbar resistance may lead to delayed grid voltage recovery.

3. An extension of the real-time simulation environment and construction of PHIL laboratory test setup for the wind turbine prototype. The environment contains dSPACE and RTDS real-time simulators, the wind turbine prototype as well as converter-controlled GE. The performance of GE is analyzed in time and frequency domains and the main performance limitations are revealed. It is shown that the design of the wind turbine prototype has impact on the GE performance in addition to the design of the emulator itself. This may not be recognized in the studies, where the performance of GE is investigated by using only a purely resistive load as in [112].

1.5 Published papers

Following publications are related to the scope of this thesis. They were written and presented by the first author. In addition, the simulations and experiments are carried out by the first author.

[1] A. S. Mäkinen and H. Tuusa, “Impact of strength of fault current path on the operation of decoupled double synchronous reference frame – phase locked loop”, In *International Conference on Renewable Energies and Power Quality*, *ICREPQ*, Bilbao, 2013, p. 6.

[2] A. S. Mäkinen and H. Tuusa, "Analysis, comparison and performance evaluation of wind turbine synchronizing methods," in *IEEE International Conference on Computer as a Tool, EUROCON*, Zagreb, 2013, p. 8.

[3] A. Mäkinen and H. Tuusa, "Wind turbine and grid interaction studies using integrated real-time simulation environment," in *Nordic Workshop on Power and Industrial Electronics*, Espoo, 2008, p. 8.

[4] A. S. Mäkinen, O. Raipala, K. Mäki, S. Repo and H. Tuusa, "Fault-ride through capability of full-power converter wind turbine," *Journal of Energy and Power Engineering,* vol. 4, no. 1, pp. 29-45, 2010.

[5] A. S. Mäkinen, P. Lauttamus, O. Raipala, S. Repo and H. Tuusa, "Fault ride through study of doubly fed induction generator wind turbine in real time simulation environment," in *14th European Conference on Power Electronics and Applications, EPE*, Birmingham, 2011, p. 10.

[6] A. S. Mäkinen, T. Messo and H. Tuusa, "Power hardware-in-the-loop laboratory test environment for small scale wind turbine," in *16th European Conference on Power Electronics and Applications, EPE*, Lappeenranta, 2014, p. 10

1.6 Thesis outline

The rest of this thesis is organized as follows:

Chapter 2 presents the wind turbine and the control system models used in the thesis. In addition, the mathematical background of the synchronization methods is presented.

Chapter 3 deals with the synchronization of the control system of NSC. Special attention is paid to the operation of DDSRF-PLL during the symmetrical voltage dip. It is shown that DDSRF-PLL may operate harmfully from the power system point of view, if certain PLL tuning parameters are used. The problem description and a solution to avoid the problem is presented in Investigation 1.

A comparison and performance evaluation of SRF-PLL, DDSRF-PLL and DSOGI-FLL under the grid disturbances is carried out in Investigation 2. The aim is to show how a tuning parameter selection impacts the performance of the synchronizing methods. The results are compared against the theory expressed in Chapter 2.

Chapter 4 presents the combined real-time simulation environment implemented by using RTDS and dSPACE real-time simulators for a FPC wind turbine. The hardware arrangement of the simulation system is presented and the simulation results are verified against the offline simulations carried out by using Matlab Simulink in Investigation 3.

The real-time simulation environment is constructed also for a DFIG wind turbine model. The real-time model is used to study and analyze the impact of the transient flux

compensation control during the symmetrical voltage dip in Investigation 4. The operation of the DFIG wind turbine with the crowbar protection during the voltage recovery is analyzed in Investigation 5 with the real-time model.

Chapter 5 presents the extension of the real-time simulation environment to PHIL environment. The laboratory test setup for a wind turbine prototype is described and the detailed analysis of the GE performance is carried out. An analysis of positive and negative sequence frequency response measurements is carried out in Investigation 6 with performance evaluation of GE in a frequency domain. Investigation 7 contains the transient performance assessment of GE by using time domain measurements.

Chapter 6 concludes the thesis and proposes future research topics.

2. Wind turbine models

In this chapter, the mathematical background of the FPC and DFIG wind turbine models as well as the control systems of GSC, RSC and NSC are presented. In addition, NSC synchronization methods under research are presented.

2.1 FPC wind turbine

The full power wind turbine was illustrated in Fig. 1.4. The wind turbine rotor extracts kinetic energy from wind and converts it into rotational energy of a rotor shaft. A gearbox between the wind turbine rotor and the generator is used to increase rotational speed of the shaft to be suitable for the generator, which is PMSG in this thesis. The electrical power from the generator is rectified into the DC-link with help of IGBT-based GSC. Then, NSC feeds the power to AC grid. A step up transformer is used to increase the voltage suitable to the grid.

2.1.1 Wind turbine rotor

A rotor model is based on an equation, which describes the power extraction of the rotor from the wind [113]

$$P_t = \frac{1}{2} A \rho c_p(\lambda, \beta) v_w^3, \tag{2.1}$$

where P_t is the wind turbine rotor power, A is a rotor swept area, ρ is an air density, c_p is a performance coefficient, λ is a tip speed ratio, β is a blade angle and v_w is wind speed. The tip speed ratio is defined as a ratio between the blade tip speed v_{tip} and the wind speed and it can be given as [113]

$$\lambda = \frac{v_{tip}}{v_w} = \frac{\omega_t R}{v_w}, \tag{2.2}$$

where ω_t is the angular frequency of the rotor and R is a rotor radius.

The performance coefficient is defined as a ratio between the wind turbine rotor power and the power of the wind. The performance coefficient as a function of the tip speed ratio with

a zero blade angle is shown in Fig. 2.1. An algebraic equation of the performance coefficient as a function of the tip speed ratio and blade angle can be given as [2]

$$c_p(\lambda,\beta) = 0.73\left(\frac{151}{\lambda_i} - 0.58\beta - 0.002\beta^{2.14} - 13.2\right)\exp\left(\frac{-18.4}{\lambda_i}\right), \tag{2.3}$$

where

$$\lambda_i = \left[\left(\frac{1}{\lambda - 0.02\beta}\right) - \left(\frac{-0.003}{\beta^3 + 1}\right)\right]^{-1}. \tag{2.4}$$

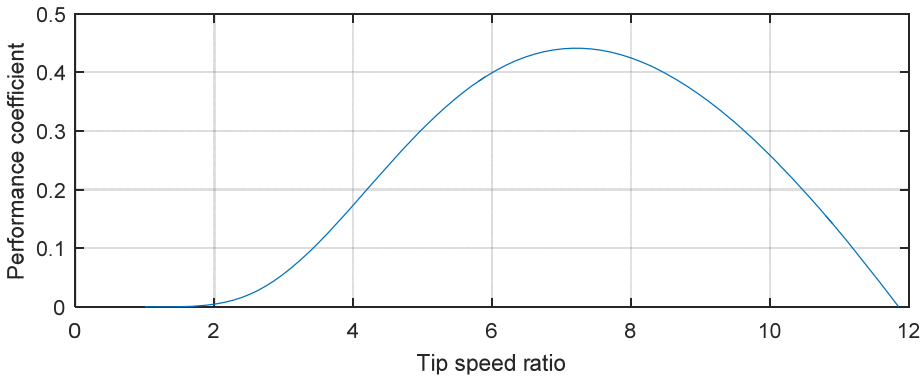

Fig. 2.1. Performance coefficient as function of tip speed ratio.

It can be noticed from Fig. 2.1 that there exists an optimal tip speed ratio which maximizes the power generation from the wind. In other words, the wind turbine must be able to modify its rotational frequency as the wind speed changes in order to maximize the electricity generation.

2.1.2 Drive train

The transmission ratio n of an ideal gearbox model is defined as a relation between the angular frequencies of the generator rotor ω_t and the wind turbine rotor

$$n = \frac{\omega_r}{\omega_t}. \tag{2.5}$$

An equation of motion determines whether the turbine rotor accelerates, decelerates or operates with constant speed. In mathematical terms, the equation of motion is defined as [114]

$$J' \frac{\mathrm{d}\omega_\mathrm{r}}{\mathrm{d}t} = t_\mathrm{g} + t_\mathrm{e} - B' \omega_\mathrm{r} , \tag{2.6}$$

where J' is total inertia of the wind turbine system reduced to the generator shaft, t_g is mechanical torque reduced to the generator shaft, t_e is electromagnetic torque, which is negative in generator operation, and B', which is reduced to the generator shaft, takes into account the losses proportional to the rotational speed (e.g. friction).

2.1.3 Permanent magnet synchronous generator

PMSG is modeled in a rotor reference frame, and its direct and quadrature axis equivalent circuits are presented in Fig. 2.2.

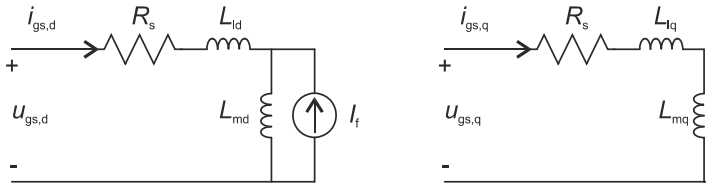

Fig. 2.2. Equivalent circuit for PMSG.

Stator voltage components of PMSG in the rotor reference frame can be given as follows [115]

$$u_{\mathrm{gs,d}} = R_\mathrm{s} i_{\mathrm{gs,d}} + \frac{\mathrm{d}\psi_\mathrm{d}}{\mathrm{d}t} - \omega_\mathrm{re} \psi_\mathrm{q} , \tag{2.7}$$

$$u_{\mathrm{gs,q}} = R_\mathrm{s} i_{\mathrm{gs,q}} + \frac{\mathrm{d}\psi_\mathrm{q}}{\mathrm{d}t} + \omega_\mathrm{re} \psi_\mathrm{d} , \tag{2.8}$$

where R_s is stator resistance, $u_{\mathrm{gs,d}}$ and $u_{\mathrm{gs,q}}$ are stator voltage components, $i_{\mathrm{gs,d}}$ and $i_{\mathrm{gs,q}}$ are stator current components, ψ_d and ψ_q are stator flux linkage components and ω_re is generator electrical angular frequency. The stator flux linkages can be given as [103]

$$\psi_\mathrm{d} = (L_\mathrm{ld} + L_\mathrm{md}) i_{\mathrm{gs,d}} + L_\mathrm{md} I_\mathrm{f} = L_\mathrm{d} i_{\mathrm{gs,d}} + \psi_\mathrm{pm} , \tag{2.9}$$

$$\psi_\mathrm{q} = (L_\mathrm{lq} + L_\mathrm{mq}) i_{\mathrm{gs,q}} = L_\mathrm{q} i_{\mathrm{gs,q}} , \tag{2.10}$$

where L_d and L_q are stator self-inductances, L_ld and L_lq are leakage inductances, L_md and L_mq are magnetizing inductances and ψ_pm is flux linkage of the permanent magnets.

Term ψ_{pm} is modeled using a constant current source I_f. In practice, the current I_f does not flow in the permanent magnets but it can be used to describe the flux linkage for modeling purposes. [116] If Eqs. (2.7) - (2.10) are combined, the stator voltage components can be expressed as follows

$$u_{gs,d} = R_s i_{gs,d} + \frac{d\psi_d}{dt} - \omega_{re} L_q i_{gs,q}, \tag{2.11}$$

$$u_{gs,q} = R_s i_{gs,q} + \frac{d\psi_q}{dt} + \omega_{re}\left(L_d i_{gs,d} + \psi_{pm}\right). \tag{2.12}$$

The electromagnetic torque of the generator can be given as [115]

$$\begin{aligned} t_e &= \frac{3}{2}\mathrm{p}\underline{\psi}^{g} \times \underline{i}^{g}_{gs} = \frac{3}{2}\mathrm{p}\underline{\psi}^{s} \times \underline{i}^{s}_{gs} = \frac{3}{2}\mathrm{p}\underline{\psi}^{r} \times \underline{i}^{r}_{gs} = \frac{3}{2}\mathrm{p}\left(\psi_d i_{gs,q} - \psi_q i_{gs,d}\right) \\ &= \frac{3}{2}\mathrm{p}\left(\psi_{pm} i_{gs,q} + i_{gs,q} i_{gs,d}\left(L_d - L_q\right)\right) \end{aligned}, \tag{2.13}$$

where p is a number of pole pairs and superscripts g, s and r correspond to general, stator and rotor reference frame, respectively.

2.1.4 Frequency converter

A frequency converter decouples the frequency of generator stator windings from the grid frequency. Thus, the generator rotor can rotate depending on the wind conditions and independent of the grid voltage frequency. Therefore, the tip speed ratio can be optimized and energy extraction from the wind can be maximized. A braking chopper is modeled at the DC-link in order to protect the DC-link capacitor during the grid disturbances. The chopper is activated, when the DC-link voltage increases over a pre-defined limit. In this thesis, both GSC and NSC are modeled to execute their voltage references ideally. In other words, the modulator is not modeled in order to save the computational power of the real-time simulators. The drawback of this approach is the lack of capability to investigate events around the switching frequency. In addition, the high frequency ripple in the converter voltages and currents do not appear in the simulation results. However, the selected modeling approach is sufficient for control system operation investigations, because the control system frequency bandwidth is significantly lower than the switching frequency.

An ideal frequency converter model is based on assumption of equal powers in both AC and DC sides of the converters. In other words,

$$p_{ac} = p_{dc}\,. \tag{2.14}$$

Thus, GSC and NSC can be modeled by using the following equations

$$\begin{aligned} \frac{3}{2}\left(u_{gs,d} i_{gs,d} + u_{gs,q} i_{gs,q}\right) &= u_{dc} i_{dc,g}, \\ \frac{3}{2}\left(u_{conv,d} i_{L1,d} + u_{conv,q} i_{L1,q}\right) &= u_{dc} i_{dc,n}, \end{aligned} \tag{2.15}$$

where u_{dc} is the DC-link voltage, $i_{dc,g}$ and $i_{dc,n}$ are generator and network-side DC currents, and u_{conv} as well as i_{L1} are network-side voltage and current, respectively.

2.1.5 Control system of generator-side converter

Vector control system of GSC oriented to the rotor reference frame is shown in Fig. 2.3a. The fundamental-frequency references of the current controllers can be expressed as DC values in the reference frame, which implies that the steady state error can be eliminated by using a proportional – integral (PI) controller. The inner loop controls the stator current and the outer loop controls the angular frequency of PMSG. In order to maximize the generated power from the fluctuating wind, the reference value ω_r^* is selected to optimize the tip speed ratio. The speed control is based on the equation of motion expressed in (2.6). The output of the speed controller is the limited reference for the quadrature axis stator current component $i_{gs,q}^*$.

The outer control loop can also be realized using torque controller as shown in Fig. 2.3b. This control method can be considered as a standard method in wind turbine industry. [117] The measured rotor speed ω_r is fed as input to generate the desired torque reference t_e^*. The mathematical analysis on the torque control is presented in details in Appendix A.

It should be noted that independent on whether the outer control loop controls the generator speed or torque, the reference is selected to optimize the power extracted from the wind only during wind conditions under rated wind speed. As the wind speed exceeds the rated value, the control target is to maintain constant output power in order to prevent the turbine to experience damage caused by exceeding mechanical and electrical limits. The limitation of power extraction from the wind is typically carried out using pitch control. [117]

The reference of the stator current direct component $i_{gs,d}^{*}$ is set to zero. By this way, the electromagnetic torque is dependent solely on the current $i_{gs,q}^{*}$ as can be seen from (2.13). In addition, the stator currents are minimized, which results in minimized losses. It would be possible to use a generator stator voltage controller to provide the $i_{gs,d}^{*}$ in order to prevent a stator overvoltage under high rotational speeds [118]. However, large $i_{gs,d}^{*}$ current component would be needed to produce notable reduction in a magnetic flux. This would increase remarkably the stator losses, and therefore, the control of $i_{gs,d}^{*}$ is not typically used in PMSG drives. [116]

Terms $\left(-\omega_{re}L_{q}i_{gs,q}\right)$ and $\omega_{re}\left(\psi_{m}+L_{d}i_{gs,d}\right)$ cancel the cross-coupling effect, which appear as a result of coordination transformation. The stator voltage dq-components are transformed back to stationary abc components and the control system output is the stator voltage vector reference $\underline{u}_{gs,abc}^{*}$. Pulse width modulation (PWM) is typically used to generate the firing pulses to GSC. In this thesis, the simple generator control system with speed control is used.

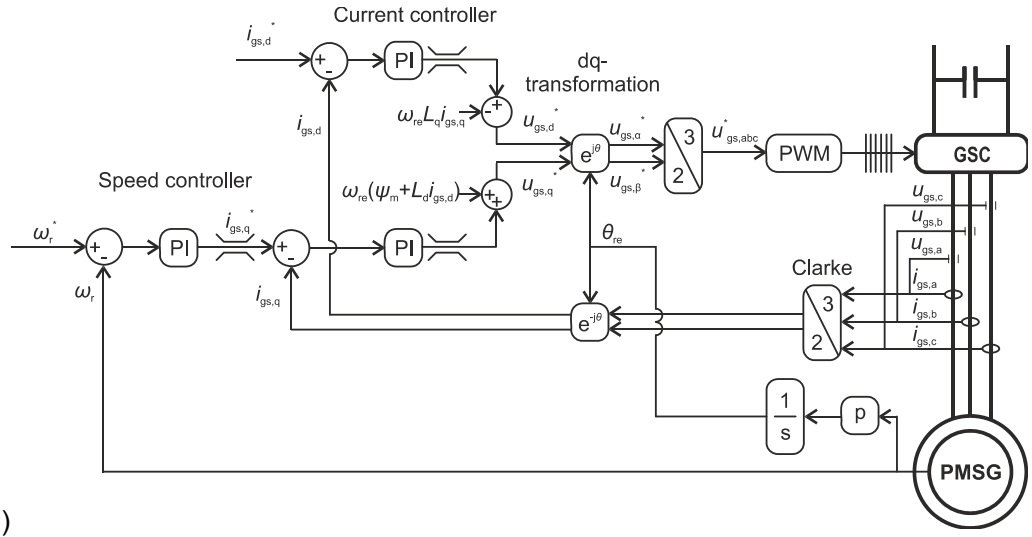

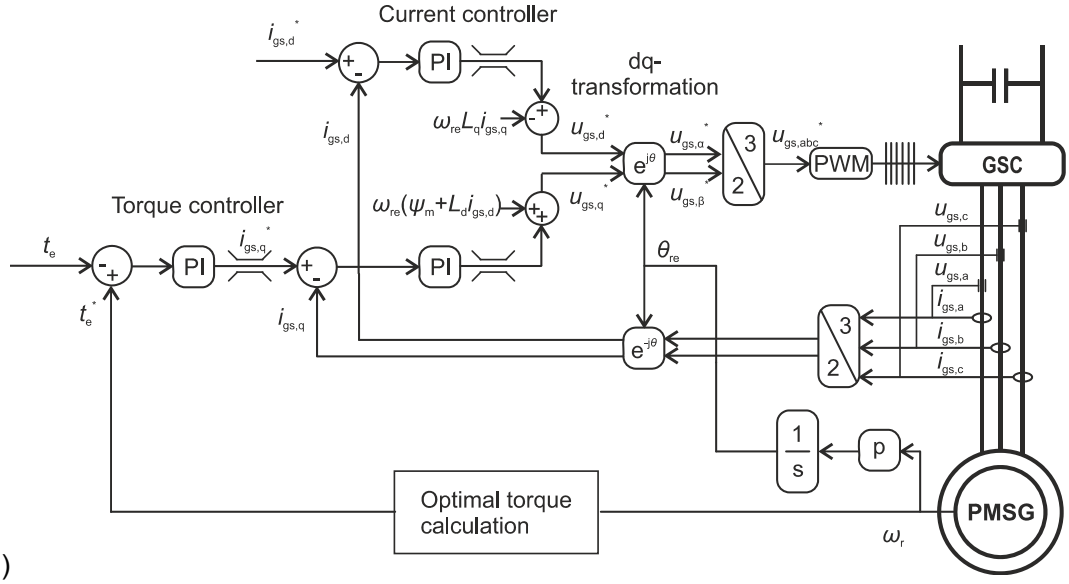

Fig. 2.3. Control system of GSC: a) with speed controller, b) non-linear torque controller.

2.1.6 Control system of network-side converter

The vector control system of NSC is implemented in a synchronous reference frame oriented to the wind turbine transformer secondary side voltage. The control system consists of an inner current control loop and outer DC-link voltage as well as reactive power control loops. Due to the reference frame selection, the DC-link voltage and reactive power can be controlled with current d- and q-components, respectively.

Current control

The space vector based NSC model is shown in Fig. 2.4. The filter capacitor branch is typically neglected in the current control design, when its capacitance value is small and, therefore, the reactance is high for low-order current harmonics. [119] The converter voltage vector in the stationary reference frame can be given as

$$\underline{u}_{\text{conv}} = \underline{u}_{\text{sync}} - \underline{u}_{\text{Lf}} = \underline{u}_{\text{sync}} - R_{\text{Lf}}\,\underline{i}_{\text{L1}} - L_{\text{Lf}}\,\frac{d\,\underline{i}_{\text{L1}}}{dt}, \tag{2.16}$$

where $\underline{u}_{\text{Lf}}$ is the voltage over inductors L_1 and L_2. Inductance L_{Lf} corresponds to the sum of inductances L_1 and L_2 while resistance R_{Lf} corresponds to the sum of resistances R_1 and R_2. The converter voltages in the synchronous reference frame can be given as

$$\underline{u}_{\text{conv}} = \underline{u}_{\text{sync}} - R_{\text{Lf}}\,\underline{i}_{\text{L1}} - L_{\text{Lf}}\,\frac{d\,\underline{i}_{\text{L1}}}{dt} - \text{j}\,\omega_{\text{sync}} L_{\text{Lf}}\,\underline{i}_{\text{L1}}, \tag{2.17}$$

where ω_{sync} is the angular frequency of the synchronous reference frame.

Eq. (2.17) can be given in component form as

$$u_{\text{conv,d}} = u_{\text{sync,d}} - R_{\text{Lf}} i_{\text{L1,d}} - L_{\text{Lf}}\,\frac{di_{\text{L1,d}}}{dt} + \omega_{\text{sync}} L_{\text{Lf}} i_{\text{L1,q}}, \tag{2.18}$$

$$u_{\text{conv,q}} = u_{\text{sync,q}} - R_{\text{Lf}} i_{\text{L1,q}} - L_{\text{Lf}}\,\frac{di_{\text{L1,q}}}{dt} - \omega_{\text{sync}} L_{\text{Lf}} i_{\text{L1,d}}. \tag{2.19}$$

The voltage components contain cross-coupling terms, which are canceled in the control system like in the case of GSC.

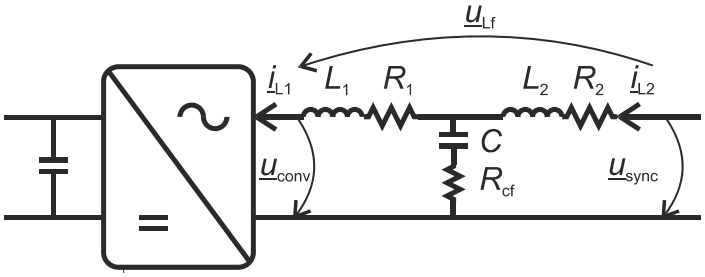

Fig. 2.4. Space vector based NSC model.

Control system oriented to network voltage

The block diagram of the vector control system of NSC oriented to the transformer secondary or synchronizing point voltage $\underline{u}_{\text{sync}}$ is shown in Fig. 2.5a. The phase angle θ_{sync} of the reference frame is received from block *Sync*, which represents the synchronizing unit. Purpose of the DC-link voltage controller is to maintain constant DC-link voltage, thereby ensuring that the generated active power is fed into the grid. Output of the DC-link-voltage controller is the reference for d-component of the converter current i_{L1d}^{*}. Reactive power controller output is the reference of q-axis component of the converter current i_{L1q}^{*}. Calculation of an instantaneous reactive power *q* is performed in the *pq-calculation* block. The reference currents i_{L1d}^{*} and i_{L1q}^{*} are compared to the measured currents and the errors are fed to the current controllers. The outputs of the current controllers are the voltage components over LCL-filter inductors u_{Ld}^{*} and u_{Lq}^{*}. After removal of the cross-coupling terms and with the help of the measured synchronizing point voltage components $u_{\text{sync,d}}$ and $u_{\text{sync,q}}$, the NSC voltage reference components $u_{\text{conv, d}}^{*}$ and $u_{\text{conv,q}}^{*}$ are obtained. It should be noticed that the voltage component $u_{\text{sync,q}}$ should be zero in the selected reference frame. The control system outputs are the NSC stationary phase voltage references $u_{\text{conv,abc}}^{*}$.

The NSC filter can also be implemented without inductor L_2 as shown in Fig. 2.5b. This is typical way in modern industrial wind turbines because of the advantage of reducing the number of installed reactive components. It should be noted that the transformer leakage inductance serves as a other L in the LCL structure.

Direct consequence of having this kind of hardware arrangement is that the synchronizing point voltage measurement is taken from the voltage over the filter capacitor. In this case, the voltage for synchronization should be carefully filtered in order to maintain proper dq-orientation and, thereby, low THD in currents and voltages. [120] If the voltage is measured like in Fig. 2.5a, the grid side inductor effectively blocks the current towards the grid and therefore the voltage at measurement point contain lower amount of harmonics. Because the switching of the IGBTs are not modelled in this thesis, the impact of selection of voltage measurement point is minor. The voltage measurement over the filter capacitor can also be used for active damping purposes. [121] The voltage measurement like in Fig. 2.5a is used in the thesis.

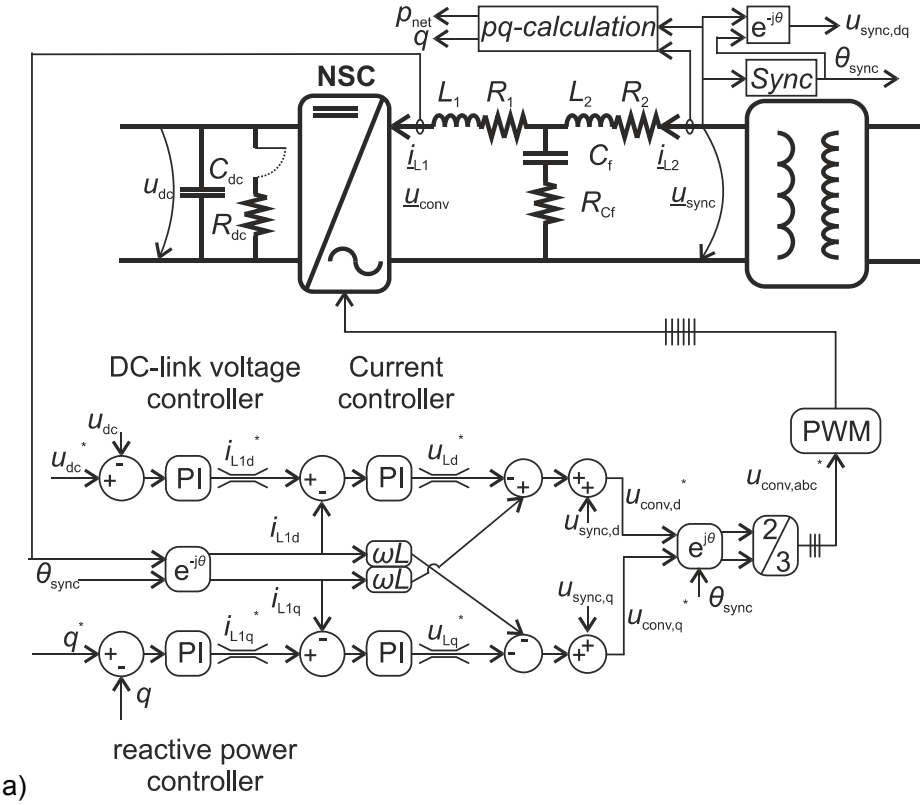

a)

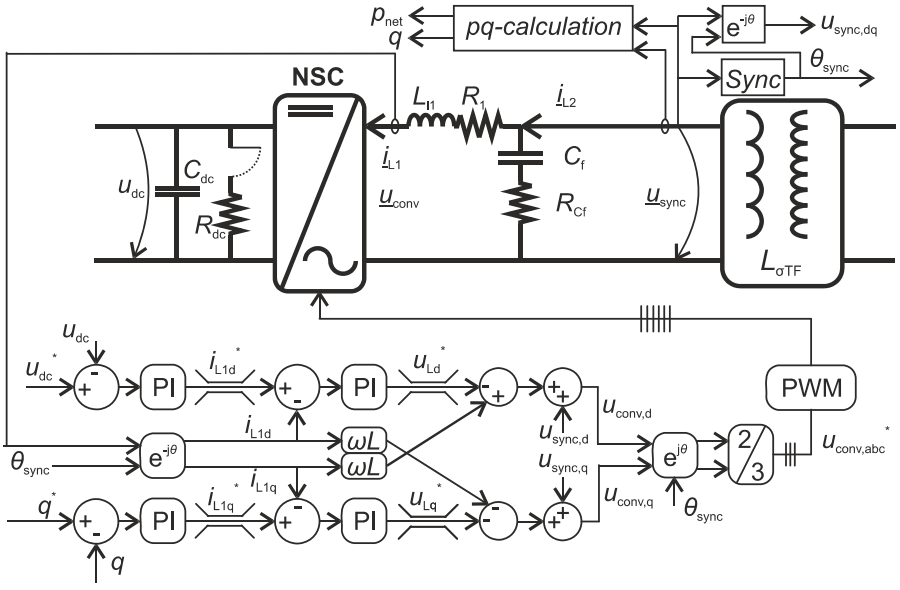

b)

Fig. 2.5a. Control system of NSC oriented to network voltage reference frame, b) orientation to voltage over filter capacitor.

2.2 DFIG wind turbine

The DFIG wind turbine concept was shown in Fig. 1.3. Wind turbine rotor, drive train and frequency converter models are identical compared to the FPC wind turbine model. In addition, the control system of NSC is similar as presented in Section 2.1.6. However, the reactive current injection by using NSC is typically applied only during the voltage dips, and the reactive power control is done by using RSC.

2.2.1 Wound rotor induction generator

A stationary reference frame space-vector based equivalent circuit of WRIG is presented in Fig. 2.6. Stator voltage vector and rotor voltage vector reduced to the stator can be given as [122]

$$\underline{u}_\mathrm{s} = R_\mathrm{s}\underline{i}_\mathrm{s} + \frac{d\underline{\psi}_\mathrm{s}}{dt}, \tag{2.20}$$

$$\underline{u}_\mathrm{r}' = R_\mathrm{r}'\underline{i}_\mathrm{r}' + \frac{d\underline{\psi}_\mathrm{r}'}{dt} - j\omega_r\underline{\psi}_\mathrm{r}', \tag{2.21}$$

where R_s and R_r are stator and rotor resistances, respectively, $\underline{\psi}_\mathrm{s}$ and $\underline{\psi}_\mathrm{r}$ are stator and rotor flux linkage vectors, respectively, $\underline{i}_\mathrm{s}$ and $\underline{i}_\mathrm{r}$ are stator and rotor current vectors, respectively and ω_r is the angular speed of the rotor. The transformer describes the generator rotor to stator turns ratio *N*. Superscript ' means reduction to the stator. The reduction can be given as:

$$\underline{u}_\mathrm{r} = N\underline{u}_\mathrm{r}', \tag{2.22}$$

$$\underline{i}_\mathrm{r} = \frac{1}{N}\underline{i}_\mathrm{r}', \tag{2.23}$$

$$R_\mathrm{r} = N^2 R_\mathrm{r}'. \tag{2.24}$$

The flux linkage vectors can be expressed as follows

$$\underline{\psi}_\mathrm{s} = (L_\mathrm{m} + L_\mathrm{sl})\underline{i}_\mathrm{s} + L_\mathrm{m}\underline{i}_\mathrm{r}' = L_\mathrm{s}\underline{i}_\mathrm{s} + L_\mathrm{m}\underline{i}_\mathrm{r}', \tag{2.25}$$

$$\underline{\psi}_\mathrm{r}' = (L_\mathrm{m} + L_\mathrm{rl}')\underline{i}_\mathrm{r}' + L_\mathrm{m}\underline{i}_\mathrm{s} = L_\mathrm{r}'\underline{i}_\mathrm{r}' + L_\mathrm{m}\underline{i}_\mathrm{s}, \tag{2.26}$$

where L_s and L_r are stator and rotor self-inductances and L_m is magnetizing inductance. The self-inductances are defined as $L_s = L_{sl} + L_m$ and $L_r' = L_{rl}' + L_m$, where L_{sl} and L_{rl} correspond to stator and rotor leakage inductances, respectively. The reduction of L_{rl} can be given as

$$L_{rl} = N^2 L_{rl}'. \tag{2.27}$$

The electromagnetic torque in the stationary reference frame is expressed as follows

$$t_e = \frac{3}{2} p \underline{\psi}_s \times \underline{i}_s = -\frac{3}{2} p\{(\psi_{s\alpha} + j\psi_{s\beta})(i_{s\alpha} - ji_{s\beta})\} = \frac{3}{2} p(\psi_{s\alpha} i_{s\beta} - \psi_{s\beta} i_{s\alpha}), \tag{2.28}$$

where subscripts α and β correspond to the two-axis components of the space vector in the stationary reference frame.

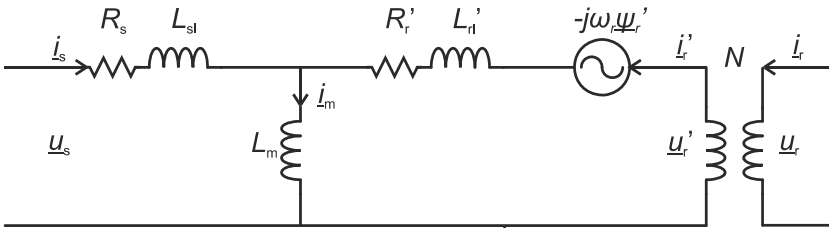

Fig. 2.6. Equivalent circuit of WRIG.

2.2.2 Control system of RSC

The vector control of RSC is carried out in the synchronous reference frame oriented to the stator flux linkage. The orientation enables independent control of the electrical torque and machine excitation via rotor current components. Therefore, the generator active and reactive powers can be controlled independently from each other.

Current control

The mathematical background of the RSC current control in the stator flux linkage reference frame is presented in this section. The stator magnetizing current $\underline{i}_{ms}$ in the reference frame can be given as

$$\underline{i}_{ms}^{s\psi} = \frac{\underline{\psi}_s^{s\psi}}{L_m} = \frac{L_s}{L_m} \underline{i}_s^{s\psi} + \underline{i}_r'^{s\psi}, \tag{2.29}$$

where superscript sψ corresponds to the stator flux linkage reference frame. Due to the reference frame selection, the flux contains only x-axis component. Thus, the above equation can be rewritten as

$$\underline{i}_{\mathrm{ms}}^{\mathrm{s}\psi} = \left|\underline{i}_{\mathrm{ms}}^{\mathrm{s}\psi}\right| = \frac{\psi_{\mathrm{x}}}{L_{\mathrm{m}}}. \tag{2.30}$$

The rotor voltage equation (2.21) in the stator flux linkage reference frame rotating with angular frequency of ω_{ms} can be given as

$$\underline{u}_{\mathrm{r}}{}'^{\mathrm{s}\psi} = R_{\mathrm{r}}'\,\underline{i}_{\mathrm{r}}{}'^{\mathrm{s}\psi} + \frac{d\underline{\psi}_{\mathrm{r}}{}'^{\mathrm{s}\psi}}{dt} - \mathrm{j}(\omega_{\mathrm{ms}} - \omega_r)\underline{\psi}_{\mathrm{r}}{}'^{\mathrm{s}\psi}. \tag{2.31}$$

From now on, the superscript sψ indicating the reference frame is omitted in order to simplify the equations. The rotor voltages can be given by taking into account (2.26) and (2.29)

$$\begin{aligned}\underline{u}_{\mathrm{r}}' &= R_{\mathrm{r}}'\,\underline{i}_{\mathrm{r}}' + L_{\mathrm{r}}'\frac{d\underline{i}_{\mathrm{r}}'}{dt} + L_{\mathrm{m}}\frac{d\underline{i}_{\mathrm{s}}}{dt} + \mathrm{j}(\omega_{\mathrm{ms}} - \omega_r)(L_{\mathrm{r}}'\,\underline{i}_{\mathrm{r}}' + L_{\mathrm{m}}\underline{i}_{\mathrm{s}}) \\ &= R'\underline{i}_{\mathrm{r}}' + \sigma L_{\mathrm{r}}'\frac{d\underline{i}_{\mathrm{r}}'}{dt} + \frac{L_{\mathrm{m}}^2}{L_{\mathrm{s}}}\frac{d\left|\underline{i}_{\mathrm{ms}}\right|}{\mathrm{dt}} + \mathrm{j}\omega_{\mathrm{sl}}\left(\sigma L_{\mathrm{r}}'\,\underline{i}_{\mathrm{r}}' + \frac{L_{\mathrm{m}}^2}{L_{\mathrm{s}}}\left|\underline{i}_{\mathrm{ms}}\right|\right)\end{aligned}, \tag{2.32}$$

where σ is a leakage factor defined as $\sigma = 1 - L_{\mathrm{m}}^2 / L_{\mathrm{s}}L_{\mathrm{r}}'$, $\sigma L_{\mathrm{r}}'$ is rotor transient inductance and ω_{sl} is a slip angular frequency. Because the stator is connected to the grid and the impact of the stator resistance is small, $\left|\underline{i}_{\mathrm{ms}}\right|$ can be assumed to be constant. Hence, the term $d\left|\underline{i}_{\mathrm{ms}}\right| / dt$ is set to zero. Therefore, the rotor voltage vector can be given as

$$\underline{u}_{\mathrm{r}}' = R'\underline{i}_{\mathrm{r}}' + \sigma L_{\mathrm{r}}'\frac{d\underline{i}_{\mathrm{r}}'}{dt} + \mathrm{j}\omega_{\mathrm{sl}}\left(\sigma L_{\mathrm{r}}'\,\underline{i}_{\mathrm{r}}' + \frac{L_{\mathrm{m}}^2}{L_{\mathrm{s}}}\left|\underline{i}_{\mathrm{ms}}\right|\right). \tag{2.33}$$

This can be expressed in the component form as follows

$$u_{\mathrm{rx}}' = R_{\mathrm{r}}'\,i_{\mathrm{rx}}' + \sigma L_{\mathrm{r}}'\frac{di_{\mathrm{rx}}'}{dt} - \omega_{\mathrm{sl}}\sigma L_{\mathrm{r}}'\,i_{\mathrm{ry}}', \tag{2.34}$$

$$u_{\mathrm{ry}}' = R_{\mathrm{r}}'\,i_{\mathrm{ry}}' + \sigma L_{\mathrm{r}}'\frac{di_{\mathrm{ry}}'}{dt} + \omega_{\mathrm{sl}}\left(\sigma L_{\mathrm{r}}'\,i_{\mathrm{rx}}' + \frac{L_{\mathrm{m}}^2}{L_{\mathrm{s}}}\left|\underline{i}_{\mathrm{ms}}\right|\right). \tag{2.35}$$

It can be noticed from (2.34) and (2.35) that the current components cannot be directly controlled by using the corresponding voltage components. Thus, the cross-coupling compensation terms are added to the output of the current controllers. The cross-coupling terms $u'_{cc,x}$ and $u'_{cc,y}$ are

$$u_{cc,x}' = -\omega_{sl}\sigma L_r' i_{ry}', \tag{2.36}$$

$$u_{cc,y}' = \omega_{sl}\left(\sigma L_r' i_{rx}' + \frac{L_m^2}{L_s}|\underline{i}_{ms}|\right). \tag{2.37}$$

Torque, speed and instantaneous reactive power control

The angle of the stator flux linkage θ_{sf} is needed due to the reference frame selection. The angle is obtained from the stator voltage equation (2.20) by using stator voltage and current measurements

$$\psi_{s\alpha} = \int (u_{s\alpha} - R_s i_{s\alpha})dt, \tag{2.38}$$

$$\psi_{s\beta} = \int (u_{s\beta} - R_s i_{s\beta})dt, \tag{2.39}$$

$$\theta_{sf} = \tan^{-1}\frac{\psi_{s\beta}}{\psi_{s\alpha}}. \tag{2.40}$$

The integrals in Eqs. 2.38 and 2.39 need to be filtered for example by using band-pass filter low cut-off frequency in order to eliminate drifting of integrals and avoid DC offset.

The operation of the speed controller is based on the equation of motion (2.6), and the controller reference is selected to optimize the tip speed ratio. The output of the speed controller is the reference for the electrical torque t_e^*.

The electrical torque in the stator flux reference frame can be given as

$$t_e = \frac{3}{2}\mathrm{p}\underline{\psi}_s \times \underline{i}_s = \frac{3}{2}\mathrm{p}(\psi_{sx} i_{sy} - \psi_{sy} i_{sx}). \tag{2.41}$$

Due to the fact that the ψ_{sy} is zero in the given reference frame and taking into account (2.30), the electrical torque can be reduced to the form

$$t_e = \frac{3}{2}\mathrm{p}\psi_{sx} i_{sy} = \frac{3}{2}\mathrm{p}L_m|\underline{i}_{ms}|i_{sy}. \tag{2.42}$$

It can be seen that the torque is directly proportional to the y-component of the stator current.

The stator current can be expressed with help of (2.29) as

$$\underline{i}_{\mathrm{s}} = \frac{L_{\mathrm{m}}}{L_{\mathrm{s}}}\left(|\underline{i}_{\mathrm{ms}}| - \underline{i}_{\mathrm{r}}'\right), \tag{2.43}$$

which can be given in component form as follows

$$i_{\mathrm{sx}} = \frac{L_{\mathrm{m}}}{L_{\mathrm{s}}}\left(|\underline{i}_{\mathrm{ms}}| - i_{\mathrm{rx}}'\right), \tag{2.44}$$

$$i_{\mathrm{sy}} = -\frac{L_{\mathrm{m}}}{L_{\mathrm{s}}} i_{\mathrm{ry}}' \,. \tag{2.45}$$

It can be noticed that the rotor current y-component is proportional to the stator current y-component. Therefore, the output of the torque controller is the reference of the rotor current y-component i_{ry}^{*}.

Instantaneous active and reactive powers can be presented in the stationary reference frame by utilizing grid current and stator voltage measurements as follows

$$p = \frac{3}{2}\left(u_{\mathrm{s}\alpha} i_{\mathrm{grid}\alpha} + u_{\mathrm{s}\beta} i_{\mathrm{grid}\beta}\right), \tag{2.46}$$

$$q = \frac{3}{2}\left(u_{\mathrm{s}\beta} i_{\mathrm{grid}\alpha} - u_{\mathrm{s}\alpha} i_{\mathrm{grid}\beta}\right). \tag{2.47}$$

The instantaneous reactive power can be expressed in the stator flux linkage reference frame by

$$q = \frac{3}{2}\left(u_{\mathrm{sy}} i_{\mathrm{gridx}} - u_{\mathrm{sx}} i_{\mathrm{gridy}}\right). \tag{2.48}$$

In the given reference frame, $u_{\mathrm{sx}} = 0$ and the stator voltage is aligned to y-axis ($u_{\mathrm{sy}} = |\underline{u}_{\mathrm{s}}|$). Therefore, the instantaneous reactive power expression is reduced to the following form

$$q = \frac{3}{2} u_{\mathrm{sy}} i_{\mathrm{gridx}} \,. \tag{2.49}$$

Hence, the reactive power can be controlled by means of grid current x-component. The grid current is the sum of the stator current and the current flowing through NSC of DFIG. Thus, the rotor current x-component can be used to control the reactive power output as can be seen from (2.44). Therefore, the output of the reactive power controller is the reference for rotor current x-component i_{rx}^{*} . The control system of RSC in the stator flux reference frame is shown in Fig. 2.7.

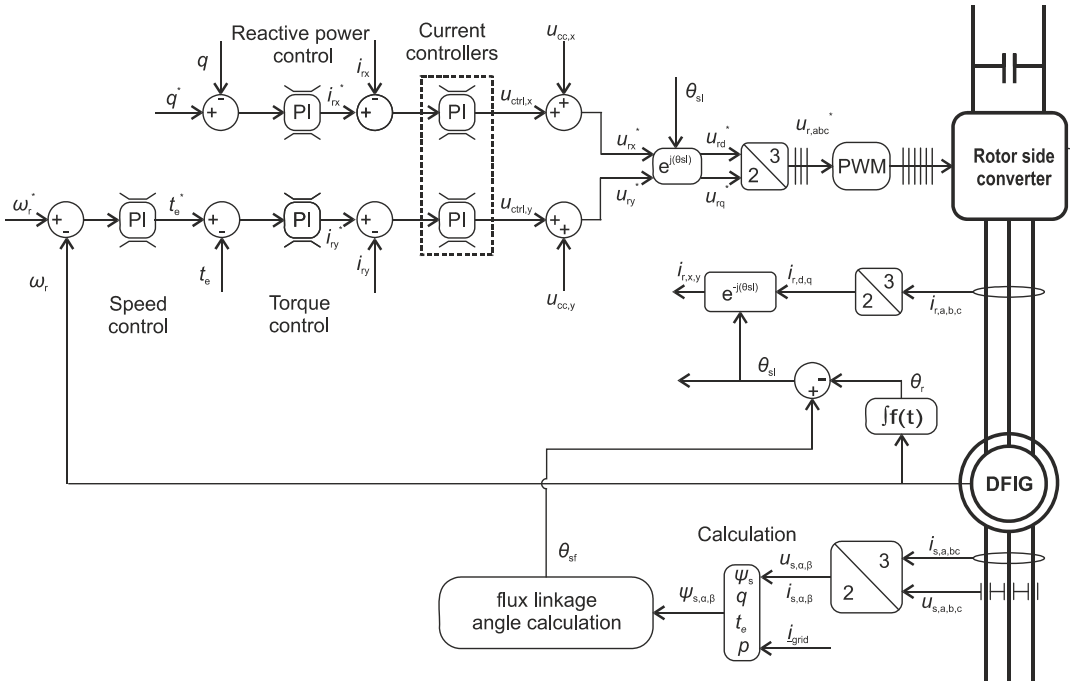

Fig. 2.7. Control system of DFIG RSC.

2.3 NSC synchronization

This section focuses on NSC synchronization block *Sync* shown in Fig. 2.5. The main target of the NSC synchronization is to provide the angle of the fundamental frequency positive sequence component from the grid voltage as fast as possible. If the angle contains other frequencies than the fundamental, the wind turbine output currents become distorted although the current references are constants.

2.3.1 Phase locked loop based on detection of zero crossings

A straightforward method to synchronize to the grid voltage is based on the detection of grid voltage zero crossings. The block diagram of the synchronization method based on

the zero crossings is shown in Fig. 2.8. [123] The measured a-phase of the grid voltage is low pass filtered in order to remove harmonics from the voltage u_a. The time difference between the zero crossing times of low pass filtered voltage u_{a1} and estimated phase angle $\theta_{ua,1}$ is controlled to zero by using PI-controller. The controller output is angle increment $\Delta\theta_{ua,1}$, which is added to previous sample time value $\theta_{ua,1}$ at every computation period. The updated value for the angle increment $\Delta\theta_{ua,1}$ is obtained only after the zero crossings. The filter delay compensation takes the phase shift caused by the low pass filter into account. The synchronizing angle θ_{sync} is achieved after subtraction of π/2, which takes into account the angle difference between a-phase voltage and voltage space vector.

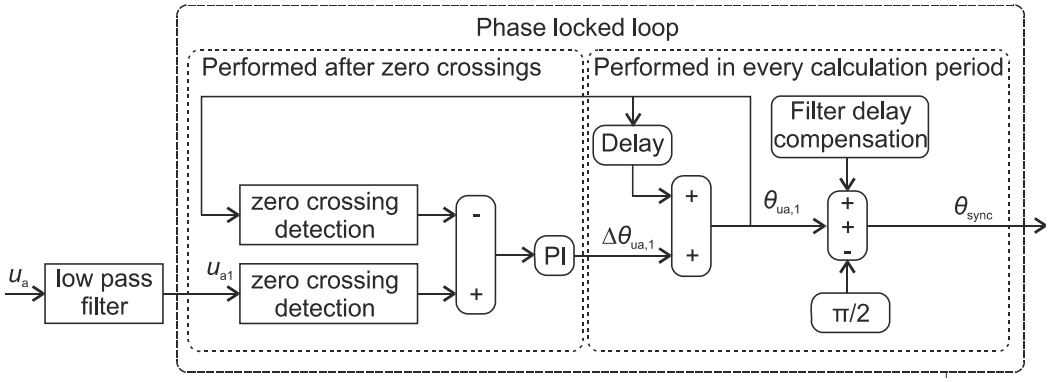

Fig. 2.8. Block diagram of PLL implementation based on zero crossing detection.

A major drawback of this synchronizing method is that the operation relies only on the measurement of the grid voltage a-phase. Thus, the behavior of two other phases are not taken into account. In addition, the method is slow, because the phase tracking can be executed only two times during one cycle. As a result, the dynamic performance may not fulfil the operation requirements. Furthermore, multiple zero crossings may be detected if the grid voltage is distorted.

2.3.2 Synchronous reference frame – phase locked loop

The block diagram of SRF-PLL is shown in Fig. 2.9. Three-phase synchronizing point voltages are Park-transformed and q-component of the grid voltage is controlled to zero by using a PI-controller. As a result, the d-axis voltage component represents the magnitude of the grid voltage. The feed forward term ω_{ff} is used to accelerate the start-up. The estimated angular position of the rotating reference frame θ_{sync} is attained after integration of the reference frame angular frequency ω_{sync}.

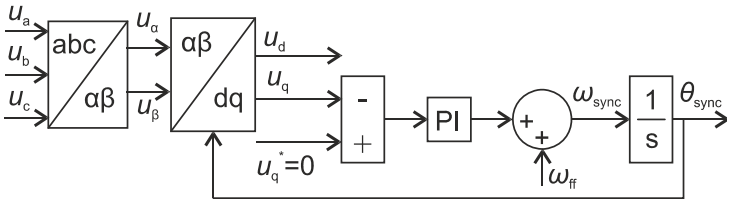

Fig. 2.9. Block diagram of SRF-PLL.

The measured three-phase grid voltages u_a, u_b and u_c after Clarke transformation are

$$\underline{u}_{\alpha\beta} = \begin{bmatrix} u_\alpha \\ u_\beta \end{bmatrix} = \lfloor T_{\alpha\beta} \rfloor \begin{bmatrix} u_a \\ u_b \\ u_c \end{bmatrix} = \frac{2}{3} \begin{bmatrix} 1 & -\frac{1}{2} & -\frac{1}{2} \\ 0 & \frac{\sqrt{3}}{2} & -\frac{\sqrt{3}}{2} \end{bmatrix} \begin{bmatrix} \hat{u}\cos\theta \\ \hat{u}\cos\left(\theta - \frac{2\pi}{3}\right) \\ \hat{u}\cos\left(\theta - \frac{4\pi}{3}\right) \end{bmatrix} = \hat{u} \begin{bmatrix} \cos\theta \\ \sin\theta \end{bmatrix}, \tag{2.50}$$

where θ is the angular position of the grid voltage vector, $\hat{u}$ is a peak value of the phase voltage and $\lfloor T_{\alpha\beta} \rfloor$ is a Clarke transformation matrix. Eq. (2.50) can be given in a rotating reference frame as

$$\underline{u}_{dq} = \begin{bmatrix} u_d \\ u_q \end{bmatrix} = \begin{bmatrix} \cos\theta_{sync} & \sin\theta_{sync} \\ -\sin\theta_{sync} & \cos\theta_{sync} \end{bmatrix} \begin{bmatrix} u_\alpha \\ u_\beta \end{bmatrix} = \hat{u} \begin{bmatrix} \cos(\theta - \theta_{sync}) \\ \sin(\theta - \theta_{sync}) \end{bmatrix}, \tag{2.51}$$

where the angle θ_{sync} is the angular position of the rotating reference frame estimated by SRF-PLL. The voltage component of interest is u_q, because the purpose is to regulate it to zero. The system is nonlinear due to the sinusoidal function in (2.51). However, the difference $\theta - \theta_{sync}$ is small after PLL is locked, which means that $\sin(\theta - \theta_{sync}) \approx \theta - \theta_{sync}$. Therefore, the system can be assumed to behave linearly and the linearized block diagram of SRF-PLL can be presented like in Fig. 2.10, where k_{LF} and T_i are loop filter, i.e. the PI-controller, gain and integration time, respectively.

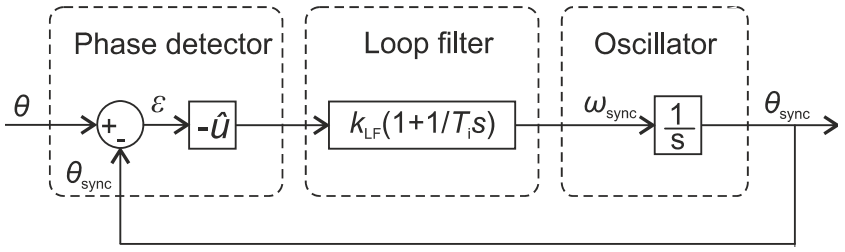

Fig. 2.10. Block diagram of linearized SRF-PLL.

Closed-loop transfer function $H_{\mathrm{cl}}(s)$ can be determined from Fig. 2.10 and it can be given as

$$H_{\mathrm{cl}}(s)=\frac{\theta_{\mathrm{sync}}}{\theta}=\frac{k_{\mathrm{PLL}}s+\dfrac{k_{\mathrm{PLL}}}{T_{\mathrm{i}}}}{s^2+k_{\mathrm{PLL}}s+\dfrac{k_{\mathrm{PLL}}}{T_{\mathrm{i}}}}, \tag{2.52}$$

where k_{PLL} is the gain of PLL, which can be expressed as

$$k_{\mathrm{PLL}}=-\hat{u}k_{\mathrm{LF}}. \tag{2.53}$$

It can be seen from (2.53) that the PLL gain is proportional to the peak value of the grid voltage in addition to the PI-controller gain. Eq. (2.52) can also be expressed in a normalized form by using damping factor ς and undamped natural frequency ω_{n} as

$$\begin{aligned}H_{\mathrm{cl}}(s)&=\frac{2\varsigma\omega_{\mathrm{n}}s+\omega_{\mathrm{n}}^2}{s^2+2\varsigma\omega_{\mathrm{n}}s+\omega_{\mathrm{n}}^2}=\frac{\dfrac{\omega_{\mathrm{n}}^2}{\omega_{\mathrm{z}}}(s+\omega_{\mathrm{z}})}{s^2+2\varsigma\omega_{\mathrm{n}}s+\omega_{\mathrm{n}}^2}=\frac{\omega_{\mathrm{n}}^2}{s^2+2\varsigma\omega_{\mathrm{n}}s+\omega_{\mathrm{n}}^2}+\frac{\dfrac{\omega_{\mathrm{n}}^2}{\omega_{\mathrm{z}}}s}{s^2+2\varsigma\omega_{\mathrm{n}}s+\omega_{\mathrm{n}}^2},\\&=H_2(s)+\frac{s}{\omega_{\mathrm{z}}}H_2(s)\end{aligned} \tag{2.54}$$

where $H_2(s)$ is normalized 2nd-order transfer function and ω_{z} is a zero frequency, which is defined as the root of the numerator [124], as

$$2\varsigma\omega_{\mathrm{n}}s+\omega_{\mathrm{n}}^2=0\Rightarrow s=-\frac{\omega_{\mathrm{n}}^2}{2\varsigma\omega_{\mathrm{n}}}=-\frac{\omega_{\mathrm{n}}}{2\varsigma}=-\omega_{\mathrm{z}}. \tag{2.55}$$

The normalized form of the closed-loop transfer function is utilized in the controller tuning. The parameters k_{PLL} and T_{i} can be calculated in terms of ς and ω_{n} by combining Eqs. (2.52) and (2.54)

$$k_{\mathrm{PLL}} = 2\varsigma\omega_{\mathrm{n}} \;\; ; \;\; T_{\mathrm{i}} = \frac{2\varsigma}{\omega_{\mathrm{n}}}. \tag{2.56}$$

2.3.2.1 Analysis of closed-loop transfer function of SRF-PLL

The closed loop transfer function of SRF-PLL, shown in (2.54), can be divided into two parts: the left-hand-side part of $H_{\mathrm{cl}}(s)$ is the normalized 2nd-order transfer function and the right-hand-side part contains the impact of zero. The significance of the zero increases as ω_{z} decreases. Thus, the impact of zero to the system response increases as ω_{n} decreases or ς increases as indicated by (2.55).

The impact of different values of ω_{n} and ς to the step responses of $H_2(s)$ and $H_{\mathrm{cl}}(s)$ is illustrated in Fig. 2.11, respectively. The increase in the damping factor decreases the rise time of the step response of $H_2(s)$ as shown in Fig. 2.11a. The increment in ω_{n} increases the speed of the response but has no effect on the overshoot of the response of $H_2(s)$, which is solely determined by ς. The differences between the responses of Figs. 2.11a and c as well as of Figs. 2.11b and d are due to the impact of zero. It can be noticed from Figs. 2.11c and d that the zero decreases the rise time and increases the overshoot of the response. In addition, as ς increases or ω_{n} decreases, the impact of the zero to the system response becomes more important as expected based on (2.55).

The above discussion gives the theoretical background for the analysis of SRF-PLL during the different network voltage disturbances with different tuning parameters. The analysis is carried out in Investigation 2 in Section 3.3.

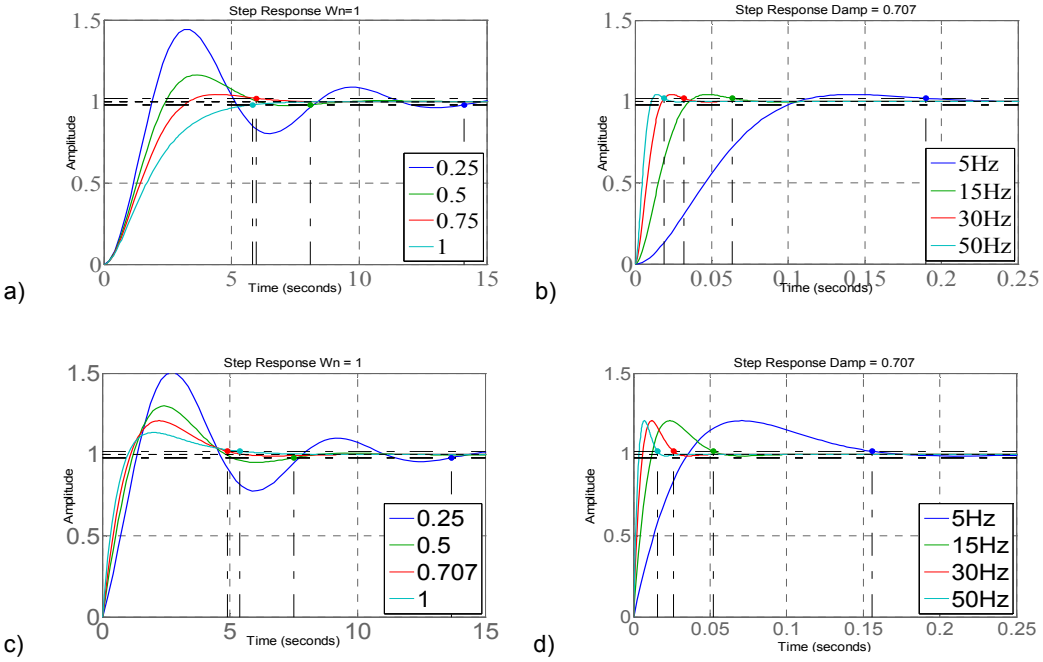

Fig. 2.11. Step response: a) $H_2(s)$ with constant ω_h, b) $H_2(s)$ with constant ς, c) $H_{cl}(s)$ with constant ω_h, d) $H_{cl}(s)$ with constant ς.

2.3.3 Decoupled double synchronous reference frame – phase locked loop

The DDSRF-PLL synchronizing method consists of a decoupling network and SRF-PLL. The decoupling network provides positive and negative sequence components from the network voltage vector. The synchronization to the positive sequence component of the grid voltage vector is done by using SRF-PLL. In this section, the mathematical background of DDSRF-PLL is given.

The unbalanced distortion free grid voltage vector $\underline{u}_{\alpha\beta}$ in the stationary reference frame can be given as [33]

$$\underline{u}_{\alpha\beta} = \begin{bmatrix} u_\alpha \\ u_\beta \end{bmatrix} = \hat{u}^+ \begin{bmatrix} \cos(\omega t + \varphi^+) \\ \sin(\omega t + \varphi^+) \end{bmatrix} + \hat{u}^- \begin{bmatrix} \cos(-\omega t + \varphi^-) \\ \sin(-\omega t + \varphi^-) \end{bmatrix}, \tag{2.57}$$

where superscripts + and – correspond to positive and negative sequence references, respectively, and φ is an initial angle. It is assumed that the reference frame estimated by the synchronization system rotates synchronously with the fundamental frequency positive

sequence component of the grid voltage. Thus, $\theta_{\text{sync}} = \omega t$. The positive and negative sequence components can be given in the synchronous dq-reference frame as

$$\begin{aligned}\underline{u}_{\text{dq}}^{+} &= \begin{bmatrix} u_{\text{d}}^{+} \\ u_{\text{q}}^{+} \end{bmatrix} = \left[T_{\text{dq}}^{+}\right]\begin{bmatrix} u_{\alpha} \\ u_{\beta} \end{bmatrix} = \begin{bmatrix} \cos(\theta_{\text{sync}}) & \sin(\theta_{\text{sync}}) \\ -\sin(\theta_{\text{sync}}) & \cos(\theta_{\text{sync}}) \end{bmatrix}\begin{bmatrix} u_{\alpha} \\ u_{\beta} \end{bmatrix} \\ &= \hat{u}^{+}\begin{bmatrix} \cos(\varphi^{+}) \\ \sin(\varphi^{+}) \end{bmatrix} + \hat{u}^{-}\cos(\varphi^{-})\begin{bmatrix} \cos(2\omega t) \\ -\sin(2\omega t) \end{bmatrix} + \hat{u}^{-}\sin(\varphi^{-})\begin{bmatrix} \sin(2\omega t) \\ \cos(2\omega t) \end{bmatrix}\end{aligned}, \tag{2.58}$$

$$\begin{aligned}\underline{u}_{\text{dq}}^{-} &= \begin{bmatrix} u_{\text{d}}^{-} \\ u_{\text{q}}^{-} \end{bmatrix} = \left[T_{\text{dq}}^{-}\right]\begin{bmatrix} u_{\alpha} \\ u_{\beta} \end{bmatrix} = \begin{bmatrix} \cos(\theta_{\text{sync}}) & -\sin(\theta_{\text{sync}}) \\ \sin(\theta_{\text{sync}}) & \cos(\theta_{\text{sync}}) \end{bmatrix}\begin{bmatrix} u_{\alpha} \\ u_{\beta} \end{bmatrix} \\ &= \hat{u}^{-}\begin{bmatrix} \cos(\varphi^{-}) \\ \sin(\varphi^{-}) \end{bmatrix} + \hat{u}^{+}\cos(\varphi^{+})\begin{bmatrix} \cos(2\omega t) \\ \sin(2\omega t) \end{bmatrix} + \hat{u}^{+}\sin(\varphi^{+})\begin{bmatrix} -\sin(2\omega t) \\ \cos(2\omega t) \end{bmatrix}\end{aligned}. \tag{2.59}$$

Eqs. (2.58) and (2.59) contain DC and AC components. The DC components are solved in order to obtain the positive and negative sequence components from the grid voltage as follows

$$\hat{u}^{+}\begin{bmatrix} \cos(\varphi^{+}) \\ \sin(\varphi^{+}) \end{bmatrix} = \begin{bmatrix} U_{\text{d}}^{+} \\ U_{\text{q}}^{+} \end{bmatrix} = \begin{bmatrix} u_{\text{d}}^{+} \\ u_{\text{q}}^{+} \end{bmatrix} - \hat{u}^{-}\cos(\varphi^{-})\begin{bmatrix} \cos(2\omega t) \\ -\sin(2\omega t) \end{bmatrix} - \hat{u}^{-}\sin(\varphi^{-})\begin{bmatrix} \sin(2\omega t) \\ \cos(2\omega t) \end{bmatrix}, \tag{2.60}$$

$$\hat{u}^{-}\begin{bmatrix} \cos(\varphi^{-}) \\ \sin(\varphi^{-}) \end{bmatrix} = \begin{bmatrix} U_{\text{d}}^{-} \\ U_{\text{q}}^{-} \end{bmatrix} = \begin{bmatrix} u_{\text{d}}^{-} \\ u_{\text{q}}^{-} \end{bmatrix} - \hat{u}^{+}\cos(\varphi^{+})\begin{bmatrix} \cos(2\omega t) \\ \sin(2\omega t) \end{bmatrix} - \hat{u}^{+}\sin(\varphi^{+})\begin{bmatrix} -\sin(2\omega t) \\ \cos(2\omega t) \end{bmatrix}. \tag{2.61}$$

where U_{d}^{+} , U_{q}^{+} , U_{d}^{-} and U_{d}^{-} are d- and q-components of the positive and negative sequence components after decoupling network, respectively.

The decoupling network, shown in Fig. 2.12, is created based on (2.60) and (2.61). It cancels the AC component from the positive sequence voltages, which is caused by the negative sequence grid voltage. In addition, the AC component in the negative sequence voltages appearing due to the positive sequence grid voltage is canceled. The outputs of the decoupling network are the positive and negative sequence grid voltage components represented as DC values. The block LPF, shown in Fig. 2.12, represents a simple low pass filter with a cut-off frequency of ω_{f} as follows

$$\text{LPF}(s) = \frac{\omega_{\text{f}}}{s + \omega_{\text{f}}}. \tag{2.62}$$

where $\overline{U}_{\mathrm{d}}^{+}$, $\overline{U}_{\mathrm{q}}^{+}$, $\overline{U}_{\mathrm{d}}^{-}$ and $\overline{U}_{\mathrm{q}}^{-}$ correspond to the filtered d- and q-components of the positive and negative sequence voltages, respectively.

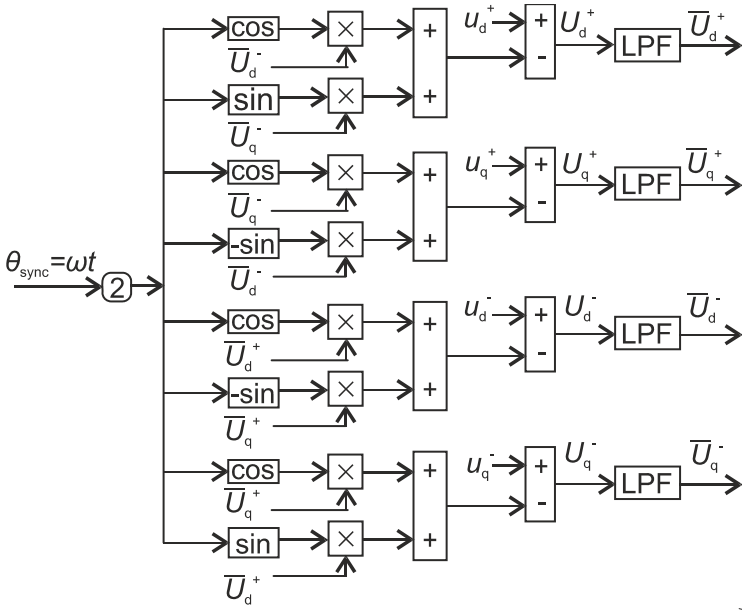

Fig. 2.12. Block diagram of decoupling network.

The block diagram of DDSRF-PLL is shown in Fig. 2.13. The synchronization to the positive sequence network voltage component is perfect, when the positive sequence q-axis voltage component after decoupling network U_{q}^{+} is zero. In that case, the initial angle φ^{+} is zero and the positive sequence voltage is aligned to d^{+}-axis. In other words, it can be expressed as

$$U_{\mathrm{d}}^{+} = \left|\hat{u}^{+}\right|. \tag{2.63}$$

The positive sequence network voltage angle θ_{sync} is attained by using SRF-PLL.

Due to the fact that the gain of SRF-PLL depends on the magnitude of the input voltage, the input U_{q}^{+} is actively normalized to the magnitude of the positive sequence component of the input voltage. The purpose is to prevent the loss of gain phenomenon [36], which means the decrement of the gain during the decreased grid voltage. In addition, the increase of the gain during the grid overvoltage is prevented.

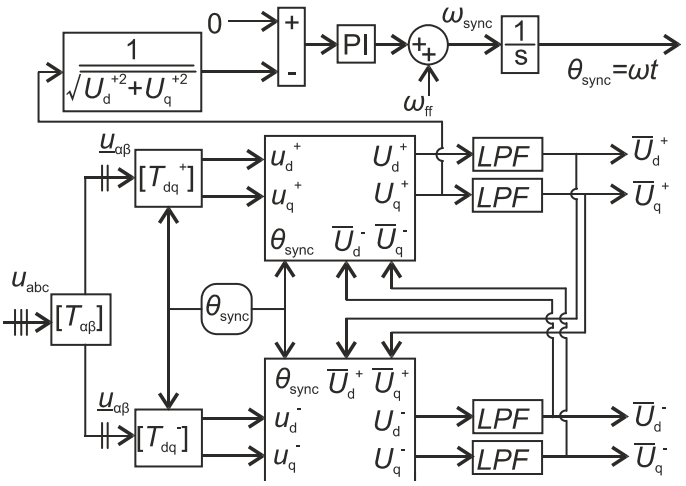

Fig. 2.13. Block diagram of DDSRF-PLL.

2.3.4 Dual second order generalized integrator – frequency locked loop

The DSOGI-FLL synchronization method extracts the positive and negative sequence components from the grid voltage in the stationary reference frame. The purpose of DSOGI is to produce in-quadrature axis components from the grid voltage vector, which are needed in the computation of the positive and negative sequence components. DSOGI is a bandpass filter, whose resonant frequency is actively tuned to the grid frequency by using FLL.

2.3.4.1 Instantaneous symmetrical grid voltage components

The instantaneous positive and negative sequence components of the grid voltages can be computed using Fortescue operator $\alpha=e^{j2\pi/3}=e^{j120^\circ}=-1/2+j*\sqrt{3}/2$ [125]

$$\begin{bmatrix} u_a^+ \\ u_b^+ \\ u_c^+ \end{bmatrix} = \frac{1}{3}\begin{bmatrix} 1 & \alpha & \alpha^2 \\ \alpha^2 & 1 & \alpha \\ \alpha & \alpha^2 & 1 \end{bmatrix}\begin{bmatrix} u_a \\ u_b \\ u_c \end{bmatrix} = [T_+]\begin{bmatrix} u_a \\ u_b \\ u_c \end{bmatrix}, \tag{2.64}$$

$$\begin{bmatrix} u_a^- \\ u_b^- \\ u_c^- \end{bmatrix} = \frac{1}{3}\begin{bmatrix} 1 & \alpha^2 & \alpha \\ \alpha & 1 & \alpha^2 \\ \alpha^2 & \alpha & 1 \end{bmatrix}\begin{bmatrix} u_a \\ u_b \\ u_c \end{bmatrix} = [T_-]\begin{bmatrix} u_a \\ u_b \\ u_c \end{bmatrix}. \tag{2.65}$$

Eq. (2.64) is transformed into stationary reference frame 2-axis components by using Clarke transformation as follows

$$\begin{bmatrix} u_\alpha^+ \\ u_\beta^+ \end{bmatrix} = [T_{\alpha\beta}]\begin{bmatrix} u_a^+ \\ u_b^+ \\ u_c^+ \end{bmatrix} = [T_{\alpha\beta}][T_+]\begin{bmatrix} u_a \\ u_b \\ u_c \end{bmatrix} = [T_{\alpha\beta}][T_+][T_{\alpha\beta}]^{-1}\begin{bmatrix} u_\alpha \\ u_\beta \end{bmatrix}, \tag{2.66}$$
$$= \frac{1}{2}\begin{bmatrix} 1 & \mathrm{j} \\ -\mathrm{j} & 1 \end{bmatrix}\begin{bmatrix} u_\alpha \\ u_\beta \end{bmatrix} = \frac{1}{2}\begin{bmatrix} 1 & -q \\ q & 1 \end{bmatrix}\begin{bmatrix} u_\alpha \\ u_\beta \end{bmatrix} = [T_{\alpha\beta}^+]\begin{bmatrix} u_\alpha \\ u_\beta \end{bmatrix}$$

where the operator q is the 90°-lagging phase-shift operator i.e.,

$$q = \mathrm{e}^{-\frac{\mathrm{j}\pi}{2}}. \tag{2.67}$$

The negative sequence components from the αβ-grid voltages can be computed by utilizing (2.65) as follows

$$\begin{bmatrix} u_\alpha^- \\ u_\beta^- \end{bmatrix} = [T_{\alpha\beta}][T_-][T_{\alpha\beta}]^{-1}\begin{bmatrix} u_\alpha \\ u_\beta \end{bmatrix} = \frac{1}{2}\begin{bmatrix} 1 & q \\ -q & 1 \end{bmatrix}\begin{bmatrix} u_\alpha \\ u_\beta \end{bmatrix} = [T_{\alpha\beta}^-]\begin{bmatrix} u_\alpha \\ u_\beta \end{bmatrix}. \tag{2.68}$$

The positive and negative sequence components can be identified from the grid voltage vector using matrixes $[T_{\alpha\beta}^+]$ and $[T_{\alpha\beta}^-]$ according to (2.66) and (2.68). However, in order to use the equations, the operator q needs to be implemented in practice. The implementation is done by using DSOGI.

2.3.4.2 Dual second order generalized integrator

DSOGI consists of two SOGIs, which are second order adaptive bandpass filters. SOGIs generate in-phase and 90°-phase-shifted components from the input voltages u_α and u_β in a resonant frequency ω'. The structure of SOGI is shown in Fig. 2.14, where u is the input voltage, u' is the output voltage in-phase with the u, qu' is the output voltage in quadrature-phase with the u, k_{SOGI} is the system gain and $\varepsilon_{\mathrm{SOGI}}$ is the error measure. The transfer functions of SOGI can be defined by utilizing Fig. 2.14 yielding as [33]

$$D(s) = \frac{u'}{u}(s) = \frac{k_{\mathrm{SOGI}}\omega' s}{s^2 + k_{\mathrm{SOGI}}\omega' s + \omega'^2}, \tag{2.69}$$

$$Q(s) = \frac{qu'}{u}(s) = \frac{k_{\mathrm{SOGI}}\omega'^2}{s^2 + k_{\mathrm{SOGI}}\omega' s + \omega'^2}, \tag{2.70}$$

$$E(s)=\frac{\varepsilon_{SOGI}}{u}(s)=\frac{s^2+\omega'^2}{s^2+k_{SOGI}\omega' s+\omega'^2}. \tag{2.71}$$

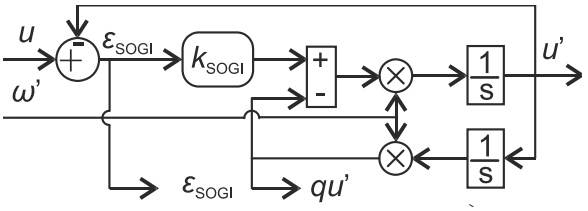

Fig. 2.14. Structure of SOGI.

The Bode plots of the transfer functions $D(s)$ and $Q(s)$ with different k_{SOGI} values are shown in Figs. 2.15a and b, respectively. The resonant frequency of SOGI is set to 2π*50Hz.

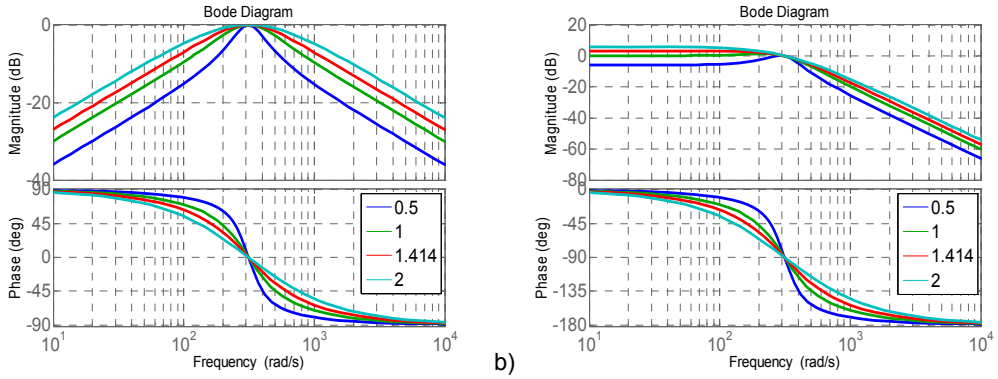

a) b)

Fig. 2.15. Bode plot: a) $D(s)$, b) $Q(s)$.

The bandwidth of the transfer functions is determined by the gain k_{SOGI}. The bandwidth increases as the gain value increases leading to faster response. However, as k_{SOGI} decreases the selectivity of the filter increases indicating an improved harmonic rejection.

The in-phase and 90°-phase-shifted components in the resonant frequency ω' generated by DSOGI are utilized as building blocks of the matrixes $[T_{\alpha\beta}^{+}]$ and $[T_{\alpha\beta}^{-}]$ as follows

$$\begin{bmatrix} u_\alpha^+ \\ u_\beta^+ \end{bmatrix} = \left[T_{\alpha\beta}^+\right]\begin{bmatrix} u_\alpha \\ u_\beta \end{bmatrix} = \frac{1}{2}\begin{bmatrix} 1 & -q \\ q & 1 \end{bmatrix}\begin{bmatrix} u_\alpha \\ u_\beta \end{bmatrix} = \frac{1}{2}\begin{bmatrix} D(s) & -Q(s) \\ Q(s) & D(s) \end{bmatrix}\begin{bmatrix} u_\alpha \\ u_\beta \end{bmatrix},$$
$$= \frac{1}{2}\frac{k_{SOGI}\omega' }{s^2+k_{SOGI}\omega' s+\omega'^2}\begin{bmatrix} s & -\omega' \\ \omega' & s \end{bmatrix}\begin{bmatrix} u_\alpha \\ u_\beta \end{bmatrix} \tag{2.72}$$

$$\begin{bmatrix} u_\alpha^- \\ u_\beta^- \end{bmatrix} = \frac{1}{2}\frac{k_{SOGI}\omega' }{s^2 + k_{SOGI}\omega' s + \omega'^2}\begin{bmatrix} s & \omega' \\ -\omega' & s \end{bmatrix}\begin{bmatrix} u_\alpha \\ u_\beta \end{bmatrix}. \tag{2.73}$$

Eqs. (2.72) and (2.73) show that the grid-voltage positive and negative sequence components can be computed by using DSOGI. However, the above equations are valid only if the grid frequency equals ω'. The resonant frequency is adapted to the grid frequency by using FLL.

2.3.4.3 Frequency locked loop

An operation principle of FLL can be understood by investigating the transfer functions $Q(s)$ (2.70) and $E(s)$ (2.71). The phases of the transfer functions are shown in Fig. 2.16, when the ω' is set to 2π*50Hz. The phases are in-phase to each other, when the grid frequency is lower than ω'. However, when the grid frequency is higher than ω', the phase difference of 180° appear. This means that the phases have different sign. The product of ε_{SOGI} and qu' is used as an error measure ε_{FLL}, which has positive or negative value, when the grid frequency is lower or higher than ω', respectively. ε_{FLL} is fed to an integral controller with a negative gain $-\gamma$. Thus, the positive ε_{FLL} makes the controller to decrease ω' and vice versa. The resonant frequency equals the grid frequency when ε_{FLL} is zero. The average error measure ε_{FLL} can be obtained as follows

$$\varepsilon_{FLL} = \frac{1}{2}\left(\varepsilon_{FLL\alpha} + \varepsilon_{FLL\beta}\right) = \frac{1}{2}\left(\varepsilon_{SOGI\alpha} qu'_\alpha + \varepsilon_{SOGI\beta} qu'_\beta\right). \tag{2.74}$$

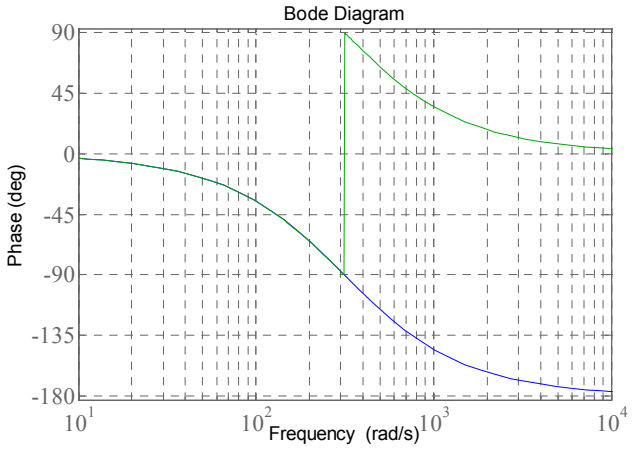

Fig. 2.16. Phases of Q(s) and E(s) when ω' is 2π*50Hz.

Finally, the structure of FLL can be expressed as shown in Fig. 2.17.

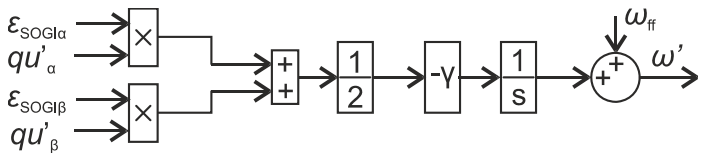

Fig. 2.17. Structure of FLL.

2.3.4.4 Dual second order generalized integrator – frequency locked loop

DSOGI-FLL contains the computation of positive and negative sequence voltage components by using (2.66) and (2.68), two SOGIs to generate the 90°-shifted components from the grid voltage and FLL to lock ω' to the grid frequency. The angle of positive sequence fundamental frequency θ_{sync} used to synchronize the control system is computed from the positive sequence αβ-components as follows

$$\theta_{sync} = \tan^{-1}\left(\frac{u_{\beta}^{+}}{u_{\alpha}^{+}}\right). \tag{2.75}$$

The block diagram of DSOGI-FLL is shown in Fig. 2.18. It is presented in detail in [33] that FLL dynamic response is affected by the square of the grid voltage, the SOGI gain and the SOGI resonant frequency. Thus, the normalized FLL gain Γ is used in this thesis, which can be given as [33]

$$\Gamma = \frac{U^2\gamma}{k_{SOGI}\omega'}. \tag{2.76}$$

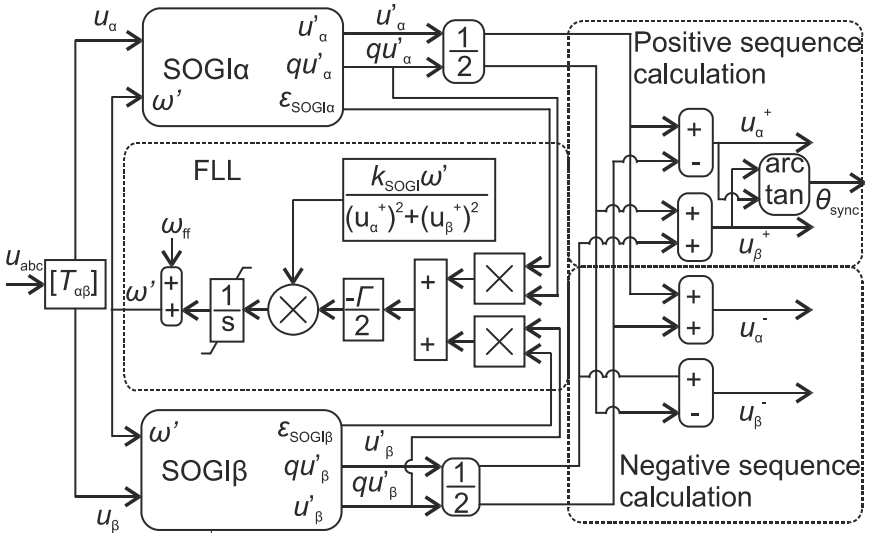

Fig. 2.18. Block diagram of DSOGI-FLL.

3. Comparison and performance evaluation of NSC synchronization methods

This chapter presents the comparison and performance evaluation of SRF-PLL, DDSRF-PLL and DSOGI-FLL synchronization methods used in the FPC wind turbine. SRF-PLL can be considered as a traditional synchronizing method, whereas DDSRF-PLL is an improved method originating from SRF-PLL. Unlike SRF-PLL and DDSRF-PLL, which operates in a synchronous reference frame, DSOGI-FLL operates in a stationary reference frame. However, DDSRF-PLL and DSOGI-FLL are comparable methods to each other, because the transfer function of the decoupling network transformed in the stationary reference frame is similar to the DSOGI transfer function. However, appropriate parameter selection needs to be made to make the methods comparable as discussed in Appendix B. Thus, the main difference of the methods is the different operations of PLL and FLL.

This chapter consists of two investigations related to the operation of the synchronizing methods during the grid disturbances. The control strategy of the FPC wind turbine during the grid fault in both Investigations is described in Section 3.1. The operation of the synchronization methods is investigated during the symmetrical grid voltage dip in Section 3.2. In Section 3.3, the operation of the methods during symmetrical and unsymmetrical voltage dips, voltage recovery as well as under the presence of grid voltage harmonics is compared from the viewpoint of parameter selection sensitivity.

3.1 Control of wind turbine during grid fault

The time constants of the phenomena related to mechanical parts operation are much larger than the time constants related to the synchronization. Because the main target of the investigations in this chapter is to analyze the operation of the synchronization methods, the drive train, the generator and GSC are modeled simply as a current source i_{WT} located in the DC-link of the frequency converter. The value i_{WT} is given as follows

$$i_{\mathrm{WT}} = \frac{p_{\mathrm{gen}}}{u_{dc}}, \tag{3.1}$$

where p_{gen} is the generated active power by the generator and u_{dc} is the DC-link voltage. The braking chopper for DC-link overvoltage protection is activated, if the DC-link voltage

increases above 1250V. After the activation, the surplus energy is dissipated in a chopper resistance R_{dc} .

The wind turbine and control system models used in both investigations of this chapter are shown in Fig. 3.1. NSC is controlled to inject reactive current during the fault in order to support the decreased grid voltage. The reference of the NSC current q-component is increased during the fault to 591A and the current $i_{WT}$is set to zero. This represents the case, where the generator active current reference $i^*_{gs,q}$ is set to zero during the fault and the energy from the wind is stored to the rotating mass of the wind turbine mechanical parts. The parameters of wind turbine and the network models are given in Appendix C.

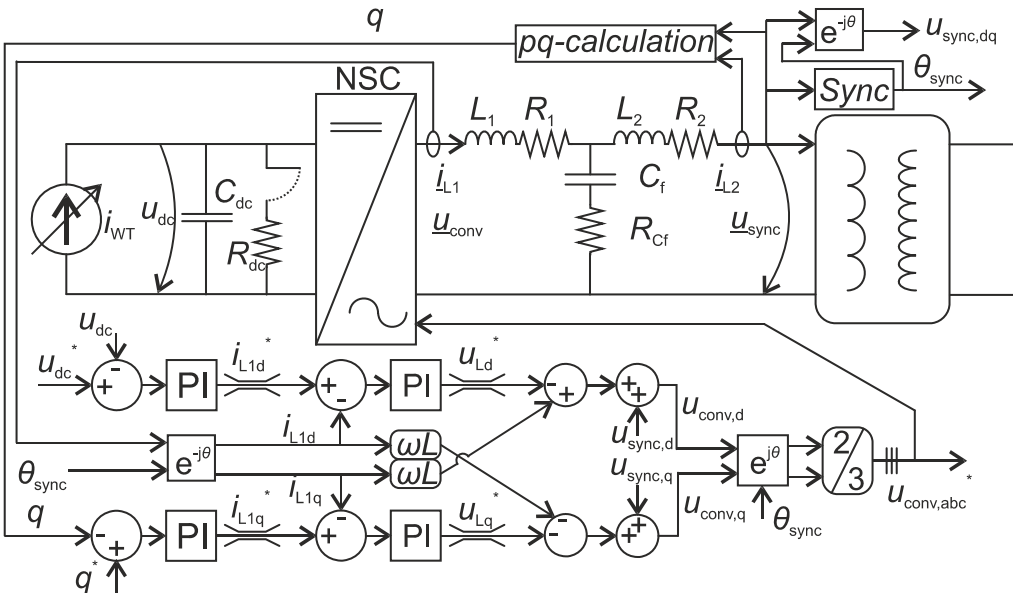

Fig. 3.1. Wind turbine and control system model used in investigations.

3.2 Investigation 1: Operation of SRF-PLL, DDSRF-PLL and DSOGI-FLL during symmetrical voltage dip

In this section, the operation of SRF-PLL, DDSRF-PLL and DSOGI-FLL during the symmetrical voltage dip is analyzed. The parameters of the synchronization methods are given in Table 3.1 by using the (ω_n, ς) parametrization.

Table 3.1. Parameters of SRF-PLL, DDSRF-PLL and DSOGI-FLL.

SRF-PLL	ω_h = 2*π*20	ς = 1/√2	-
DDSRF-PLL	ω_h = 2*π*20	ς = 1/√2	ω_f = 2*π*50/√2
DSOGI-FLL	Γ = 387	-	k_{SOGI} = √2

The wind turbine synchronizing point voltages $u_{sync,a,b,c}$ during the symmetrical voltage dip are shown in Fig. 3.2a, when SRF-PLL is used. The transients appearing on the angular frequency of SRF-PLL, shown in Fig. 3.3a, are caused by the rapid changes of the grid voltage phase, which are not filtered by the SRF-PLL loop filter. The angular frequency has not settled to the grid frequency during the 200 ms-lasting voltage dip, because the PLL gain is decreased due to the reduction of the grid voltage magnitude. After the first transients, the angular frequency of SRF-PLL follows the output of the PI-controller integrator, which is shown in Fig. 3.4a. The grid and SRF-PLL angles are shown in Fig. 3.5a. The angle of SRF-PLL is not significantly influenced by the sudden chances in the grid angle. However, the tracking of correct grid angle is slow due to the loss of gain phenomenon. The converter currents, shown in Fig. 3.6a, stay sinusoidal due to the linear behavior of the SRF-PLL angle.

The synchronizing-point voltages during the same fault with DDSRF-PLL are shown in Fig. 3.2b. The main difference between SRF-PLL and DDSRF-PLL during the voltage dip is the gain normalization of PLL in the latter method. Therefore, the gain of the PLL part of DDSRF-PLL is not affected by the magnitude of the grid voltage. The normalization could also be done to SRF-PLL. However, the drawback of the normalization is a constantly varying gain under asymmetrical network voltage conditions. Thus, the SRF-PLL gain is not normalized in the comparison.

The decoupling network and the gain normalization have a remarkable impact on the behavior of the error measure of the PLL part of DDSRF-PLL. This is due to the fact that the decoupling network cannot instantaneously detect the correct value of u_q^+ after the voltage dip and the gain of synchronization system does not decrease with the network voltage magnitude. If the PLL output frequency is not limited, the integrator of the PI-controller, shown in Fig. 3.4b, can reach a very high negative value. As a result, the angular frequency of DDSRF-PLL, shown in Fig. 3.3b, drops near to zero. The angle used by the control system of NSC, pointed out in Fig. 3.5b, remains nearly constant during the time, when the angular frequency is near to zero. Hence, the converter currents, shown in Fig. 3.6b, contain a significant DC-component. This is not tolerable, because the DC-

component overstress the transformer of the wind turbine. It should be noted that this is not a natural response of the FPC wind turbine to the symmetrical voltage dip. The reason for the DC-current generation is the poorly designed synchronization. The simulation results, expressed in Figs. 3.2b – 3.6b, emphasize the importance of an appropriate synchronization design.

The synchronizing-point voltages with DSOGI-FLL are expressed in Fig. 3.2c and the resonant frequency of the DSOGI bandpass filter is shown in Fig. 3.3c. The frequency does not suffer from the similar initial transients like the PLL-based methods. In addition, the deviation of the frequency from the nominal value is much smaller. The behavior of the frequency is mainly determined by the operation of FLL. The smaller deviation of the frequency is the consequence from the fact that the power system frequency is steadier variable than the phase angle. The network voltage angle and the angle of DSOGI-FLL are pointed out in Fig. 3.5c. It takes about one cycle from DSOGI-FLL to track the network voltage angle with decent accuracy. As expected based on the linear behavior of DSOGI-FLL angle, the converter currents, shown in Fig. 3.6c, contain mainly fundamental-frequency positive-sequence component during the fault. Thus, it can be concluded that the wind turbine is able to ride-through the fault and inject reactive current to the grid without additional stress to the grid components.

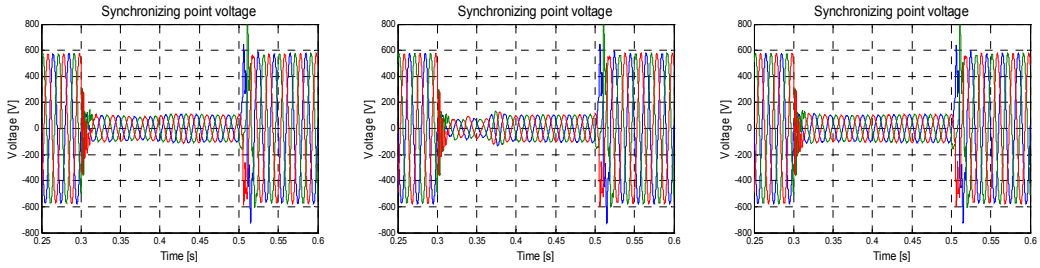

a) b) c)

Fig. 3.2. Synchronizing point voltage $u_{\text{sync,a,b,c}}$: a) SRF-PLL, b) DDSRF-PLL, c) DSOGI-FLL.

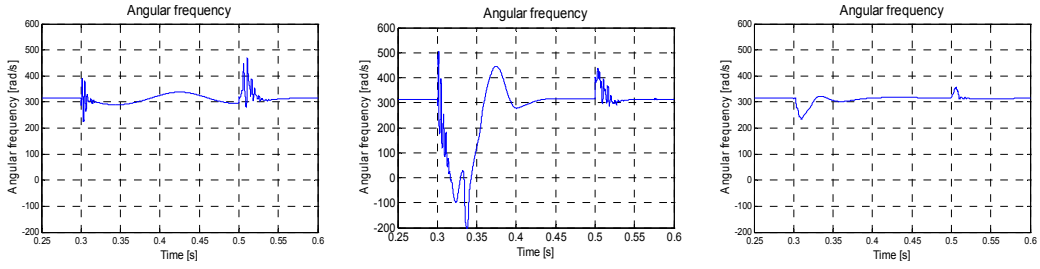

a) b) c)

Fig. 3.3. Angular frequency: a) SRF-PLL, b) DDSRF-PLL, c) DSOGI-FLL.

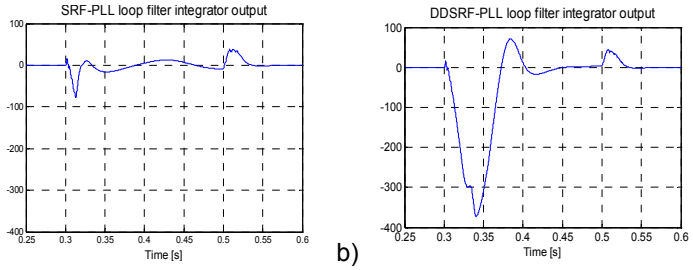

Fig. 3.4. Output of the loop filter integrator: a) SRF-PLL, b) DDSRF-PLL.

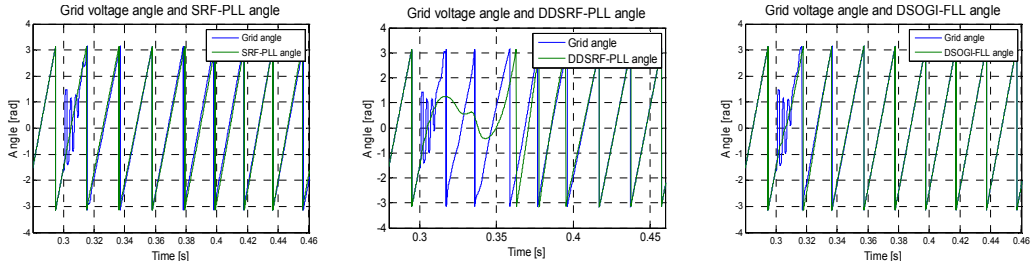

Fig. 3.5. Angle of $\underline{u}_{\text{sync}}$ compared to synchronizing method angle: a) SRF-PLL, b) DDSRF-PLL, c) DSOGI-FLL.

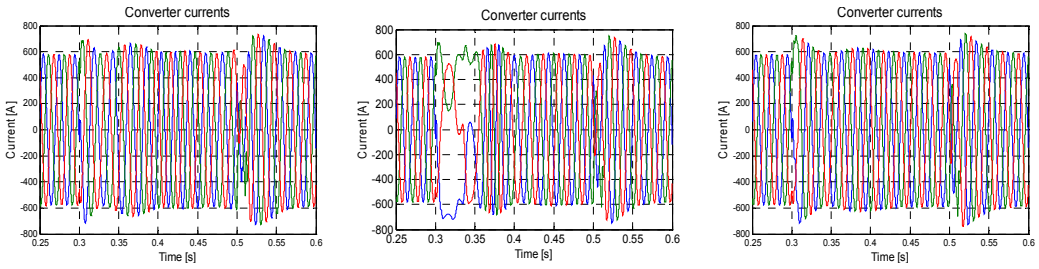

Fig. 3.6. Converter currents: a) SRF-PLL, b) DDSRF-PLL, c) DSOGI-FLL.

3.2.1 Frequency limitation and integrator anti-windup

The grid angle may change rapidly after the voltage dip causing the significant error measure ε, shown in Fig. 2.10, to be fed to the PI-controller of DDSRF-PLL. If the PI-controller is tuned to have a high gain, the controller output ω_{sync} may deviate significantly from the fundamental frequency as shown in Fig. 3.3b. The consequence is an increased amount of harmonics or even a DC-component in the generated currents. Due to the fact that the grid frequency is steadier variable, it is vice to limit the ω_{sync}. The limitation does not remove the temporary harmonic current generation after voltage dips. However, the

generation of DC-currents can be prevented. The block diagram of the SRF-PLL part of DDSRF-PLL with the controller output limitation is shown in Fig. 3.7.

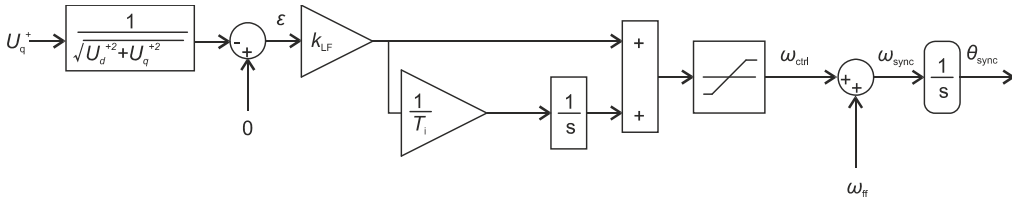

Fig. 3.7. SRF-PLL part of DDSRF-PLL with controller output limitation.

If the controller output frequency is very strictly limited, the windup of the controller integrator may become a problem. [126] If the sign of significant ε remains unchanged for a long time, the output value of the integrator increases as long as the error measure sign does not change. As was shown in Fig. 3.4b the output value may become very large. If the limited controller output value ω_{ctrl} deviates from the output value of the integrator, the angular frequency of the reference frame ω_{sync} saturates to value $\omega_{ctrl}+\omega_{ff}$. In order to prevent windup, the integration of error measure must be stopped, when the controller output reaches its limit. The structure of SRF-PLL with an anti-windup scheme is shown in Fig. 3.8. The anti-windup tracking time constant T_t should be small enough to prevent the increase of the integrator output value. It is suggested that T_t should be smaller than the integration time of the controller T_i. [126]

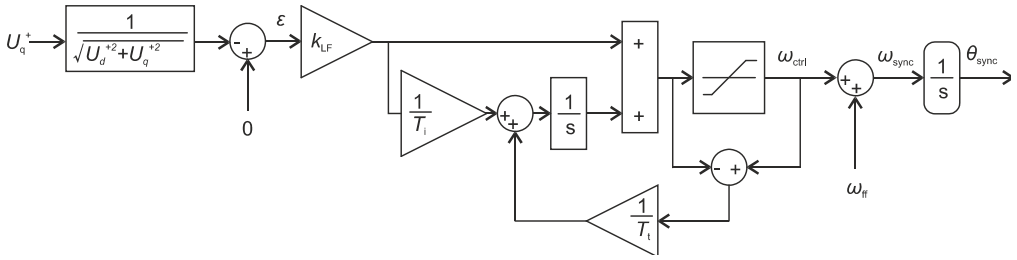

Fig. 3.8. SRF-PLL with integrator anti-windup.

The same fault is now simulated using DDSRF-PLL with SRF-PLL containing the frequency limitation to ±10 Hz with integrator-anti-windup scheme. The synchronizing-point voltages are shown in Fig. 3.9a. The controller output limitation and the integrator anti-windup prevents the integrator output to have large deviations as shown in Fig. 3.9b. Thus, the DDSRF-PLL angle follows the angle of synchronizing-point voltage with the exception that the rapid phase angle changes are filtered to a large extent as depicted in Fig. 3.9c. The converter currents contain mainly fundamental component as shown in Fig.

3.9d. It can be concluded that the wind turbine is able to ride-through the fault and inject reactive current to the grid also with DDSRF-PLL including the gain normalization.

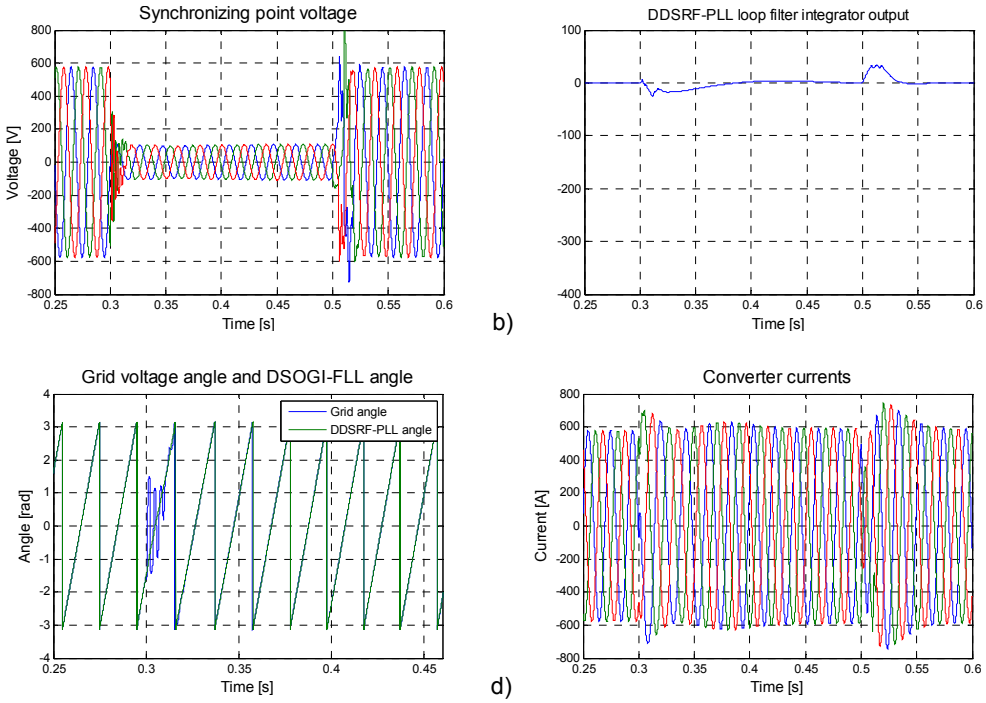

Fig. 3.9. a) Synchronizing point voltages, b) output of loop filter integrator, c) network synchronizing point and DDSRF-PLL angle, d) converter currents.

The comparison of angular frequencies, when all synchronization methods uses ±10Hz limitation, is shown in Fig. 3.10. The angular frequency of SRF-PLL does not settle down due to the loss of gain under the decreased grid voltage. Due to the gain normalization, DDSRF-PLL shows an improved angular frequency response compared to SRF-PLL. The correct frequency estimation is important, because the calculated frequency may be used to trigger other control functions of the wind turbine such as an anti-islanding detection or frequency control. The angular frequency of DSOGI-FLL is in agreement with the angular frequency of DDSRF-PLL. However, the main difference is the lack of high frequency transients after a fault initiation. The reason is the difference in the fundamental operation principle between PLL and FLL.

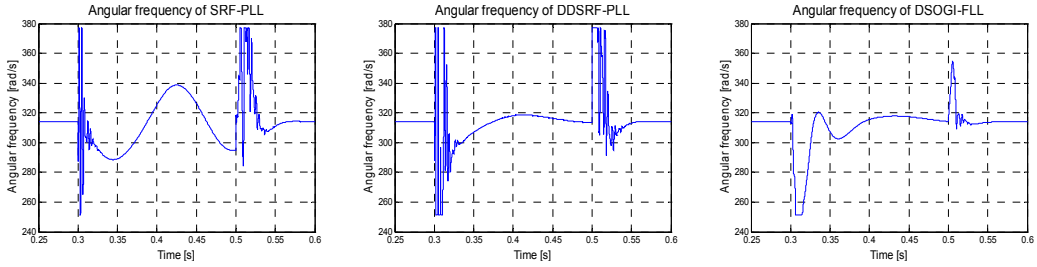

a) b) c)

Fig. 3.10. Angular frequency: a) SRF-PLL, b) DDSRF-PLL, c) DSOGI-FLL.

3.2.2 Conclusion of Investigation 1

The performance of the synchronization system has significant influence on the operation of the FPC wind turbine during the symmetrical grid fault. It is shown in Investigation 1 that the wind turbine may generate significant DC-currents during the symmetrical voltage dip if the DDSRF-PLL synchronization, demonstrated for example in [33], is used. The problem is not easy to detect, because it appears only if the loop-filter gain is high enough and the gain normalization is used. However, the DC-currents are not generated due to the high gain, but due to the unlimited output of the loop filter. It is shown that in practical applications, it is mandatory to add the frequency limitation and the integrator anti-windup arrangement to the loop filter of DDSRF-PLL in order to avoid the problem of DC-current generation. It is concluded that the wind turbine is able to ride through the symmetrical grid fault and inject reactive current to the network with all analyzed synchronizing methods. However, DSOGI-FLL provides the smoothest reference frame frequency behavior during the voltage dip.

3.3 Investigation 2: Comparison and tuning parameter selection of synchronization methods

The main task of the wind turbine is to generate electrical power into grid by feeding fundamental frequency positive sequence currents. This task is fulfilled from a control system viewpoint if the following conditions are met:

- the synchronous reference frame of vector-controlled NSC is rotating with the angular frequency of the fundamental-frequency positive-sequence component of the grid voltage,
- the references for the d- and q-axis current components are constants,
- the error measures of the current controllers are controlled to zero.

If the above conditions are not met, the output currents of the wind turbine contain also additional harmonics.

The aim of this investigation is to study, how the selection of different synchronization parameters (ς, ω_h, ω_f, k_{SOGI}, Γ) impacts on the ability of the wind turbine to generate fundamental-frequency currents during the grid voltage disturbances. Performance of the DC-link voltage controller, current controllers and synchronization system determines whether or not the aforementioned conditions are met after the disturbances. This study considers only the operation of the synchronization systems. Thus, the control system operation of NSC is identical during all the following grid disturbances, while the synchronization method and its tuning is changed. Hence, the differences in the simulation results are caused only by the performance differences of the synchronization systems.

The performance of the synchronizing systems is compared during the three-phase and two-phase fault as well as during the voltage recovery. In addition, the performance under the presence of grid voltage 5th-harmonic is evaluated. The purpose is to find the factors, which should be taken into account, when the parameters related to the synchronization systems are selected.

In order to avoid the DC current-generation problem described in Investigation 1, the output of the PLL PI-controller and the DSOGI resonant frequency ω' are limited to 2π*(±10 Hz) rad/s. In addition, the controllers are provided with the anti-windup scheme. The fundamental-frequency negative-sequence component and harmonic components from 2nd to 20th of the converter currents are measured using Matlab Simulink sequence analyzer library block, which outputs the amount of corresponding harmonic components as DC values. These DC values are integrated (summed). The converter currents are close to a pure sine wave throughout the fault, when the resulting integral of harmonics is small. Therefore, the integral of harmonics can be used to assess the quality of the generated currents and performance of the synchronization method. The integral of harmonics is normalized by using a Normal (Gaussian) distribution. From now on, the term harmonic integral corresponds to the normalized integral of harmonics. The simulation results are analyzed against to the theory introduced in Section 2.3.

Three different parameter values for damping factors ς (0.5, 0.707 and 1) are used for SRF-PLL and DDSRF-PLL in the comparison. Four values for undamped natural frequencies ω_h are located on x-axis (2π*5 Hz, 2π*15 Hz, 2π*30 Hz, 2π*50 Hz). The DDSRF-PLL performance depends also on the cut-off frequency ω_f used in the decoupling network. The values in the comparison are ω_f = 2π*50/4 and ω_f = 2π*50/√2.

The performance of DSOGI-FLL depends on k_{SOGI} and Γ. The x-axis consists of Γ values, which are chosen in a way that -3 dB bandwidths are comparable for the FLL and PLL loops if the PLL parameter selection is ς = 0.707. This is discussed in detail in Appendix B. For example, the bandwidth of SRF-PLL is 64.5 rad/s, when the settings are ω_h = 2π*5 Hz and ς = 0.707 as shown in Appendix B. Hence, the bandwidths of the PLL and FLL loops are comparable, when the respective value for the Γ is set to 64.5 rad/s. The values for k_{SOGI} are chosen to have similar transfer functions for DSOGI and the decoupling network as discussed in Appendix B. In other words, k_{SOGI}= 0.5 is comparable with ω_f = 2π*50/4 and k_{SOGI}= √2 is comparable with ω_f = 2π*50/√2.

3.3.1 Symmetrical fault and voltage recovery

The symmetrical fault occurs at 0.3 s at the point Fault 2 of the network model shown in Appendix C, and the fault is cleared at 0.5 s. The integration of the harmonic components of the currents starts in the fault beginning and ends after 100 ms from the fault clearing at 0.6 s. Thus, the operation of synchronization methods is investigated also during the voltage recovery.

The harmonic integrals of SRF-PLL during the symmetrical voltage dip with different ς and ω_h are shown in Fig. 3.11a. The performance of SRF-PLL during the voltage dip improves as the parameters ς and ω_h increase due to the increased control bandwidth. Therefore, PLL tracks the grid angle faster, which decreases the harmonic integral value.

Harmonic integrals of DDSRF-PLL are shown in Figs. 3.11b and c, when ω_f is set to 2π*50/4 and 2π*50/√2, respectively. The harmonic integrals are significantly lower than in case of SRF-PLL. The main reason is the normalization of the PLL gain. The impact of ς on the harmonic integrals is more significant, when ω_h is small due to the increased impact of zero as shown in (2.54). As ω_h increases, the controller becomes faster, which has tendency of decreasing the harmonic integrals. However, the impact of the network voltage transients (fault and voltage recovery) on the synchronizing angle increases resulting increase of the harmonic integrals due to the decreased filtering of transients. As a result, the harmonic integral values remain approximately constant. When the cut-off frequency of the low-pass filter is increased from ω_f =2π*50/4 to ω_f =2π*50/√2, the harmonic integrals generally increase due to the decreased filtering of the synchronizing angle during the transients.

The DSOGI-FLL harmonic integrals are shown in Fig. 3.11d. It can be seen that if small k_{SOGI} is selected, which means that the bandwidth of the bandpass filter is narrow as shown in Fig. 2.15, the normalized FLL gain Γ plays important role on the speed of the response. However, the increment of the bandpass filter bandwidth clearly decreases the impact of Γ. Generally, the selection of high k_{SOGI} yields to faster response. However, the increase in Γ causes decreased filtering of the synchronization angle during the transients.

The worst performance appears, when SRF-PLL is used with values ω_h =2π*(5 Hz) and ς =0.5, and the best performance is achieved using DDSRF-PLL with ω_h =2π*(15 Hz), ς =1/√2 and ω_f =2π*(50Hz)/4. The tracking of the grid angle in the worst case as well as in the best case are shown in Figs. 3.12a and b, respectively. It can be noticed that if SRF-PLL is used with low bandwidth, the tracking of the grid angle takes more than 6 cycles. The perfect tracking time is about 30 ms, when DDSRF-PLL is used.

a)

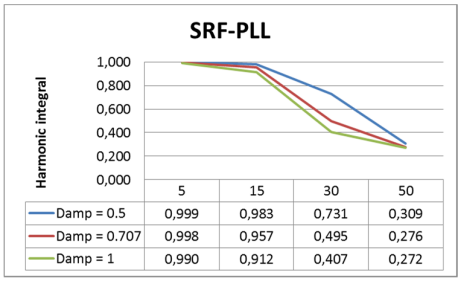

	5	15	30	50
Damp = 0.5	0,999	0,983	0,731	0,309
Damp = 0.707	0,998	0,957	0,495	0,276
Damp = 1	0,990	0,912	0,407	0,272

b)

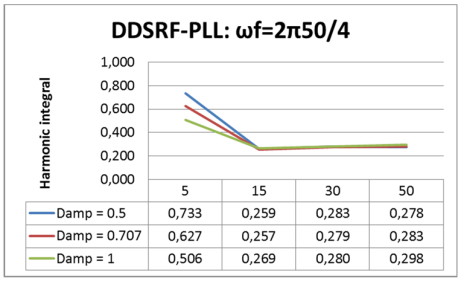

	5	15	30	50
Damp = 0.5	0,733	0,259	0,283	0,278
Damp = 0.707	0,627	0,257	0,279	0,283
Damp = 1	0,506	0,269	0,280	0,298

c)

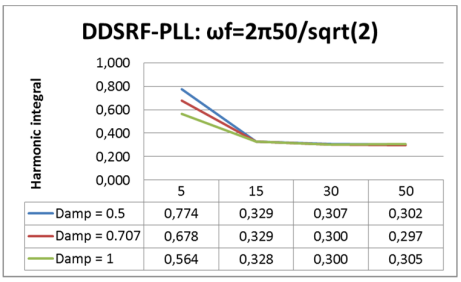

	5	15	30	50
Damp = 0.5	0,774	0,329	0,307	0,302
Damp = 0.707	0,678	0,329	0,300	0,297
Damp = 1	0,564	0,328	0,300	0,305

d)

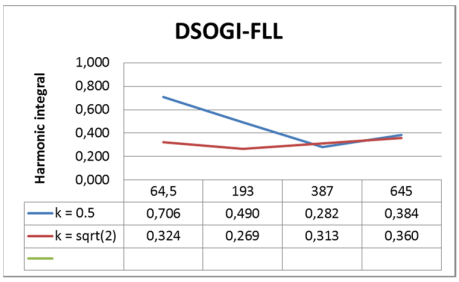

	64,5	193	387	645
k = 0.5	0,706	0,490	0,282	0,384
k = sqrt(2)	0,324	0,269	0,313	0,360

Fig. 3.11. Harmonic integrals under three-phase fault: a) SRF-PLL, b) DDSRF-PLL ω_f =2π50/4 c) DDSRF-PLL ω_f =2π50/√2, d) DSOGI-FLL.

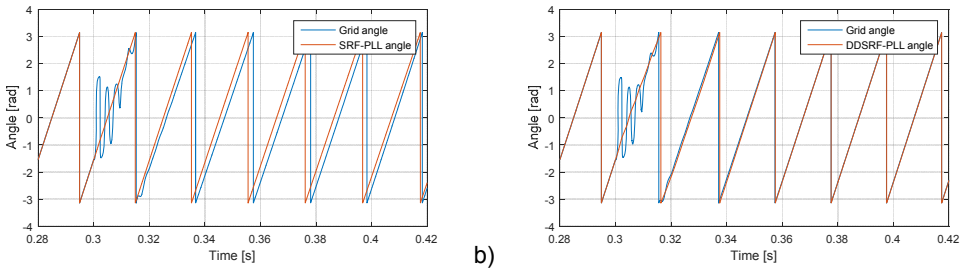

a) b)

Fig. 3.12. Behavior of grid angle and θ_{sync} : a) worst result, b) best result.

3.3.2 Unsymmetrical fault

The performances of the synchronizing methods are compared during the two-phase-to-ground fault occurring at the same Fault point. The harmonic integrals are calculated from the time span of the fault. The integrals are shown in Fig. 3.13a, when SRF-PLL is used. The integrals increase as ω_h and the ς increase, because SRF-PLL becomes more prone reacting on the negative sequence component of the grid voltage. In practice, this may be the limiting factor of the control bandwidth.

Due to the fact that the decoupling network in DDSRF-PLL cancels the effect of the negative sequence component of the grid voltage, the increase in ω_h and ς do not have noteworthy impact on the harmonic integrals as shown in Figs. 3.13b and c. The integrals of DDSRF-PLL are significantly lower compared to SRF-PLL. Thus, the performance during the unsymmetrical grid faults is clearly improved.

The DSOGI-FLL harmonic integrals are shown in Fig. 3.13d. When $\Gamma$is small, the integrals are lower with higher k_{SOGI} due to the faster tracking of the grid-voltage positive-sequence-component angle. As Γ increases, the grid angle is tracked even earlier decreasing the integrals. However, if k_{SOGI} is high, the decreased filtering of transients increases the integrals. The results between DDSRF-PLL and DSOGI-FLL are in agreement with each other, because the impact of the negative sequence voltage component is canceled from the synchronization angle.

The converter currents in the worst case (SRF-PLL: ω_h = 2π*(50 Hz) and ς = 1) and in the best case (DDSRF-PLL: ω_f = 2π*(50 Hz)/4, ω_h = 2π*(15 Hz) and ς = 0.5) are shown in Figs. 3.14a and b, respectively. After approximately 30 ms from the fault beginning, the best case currents can be considered to contain only fundamental-frequency positive-sequence component, while in the worst case, the currents are distorted during the whole monitored interval.

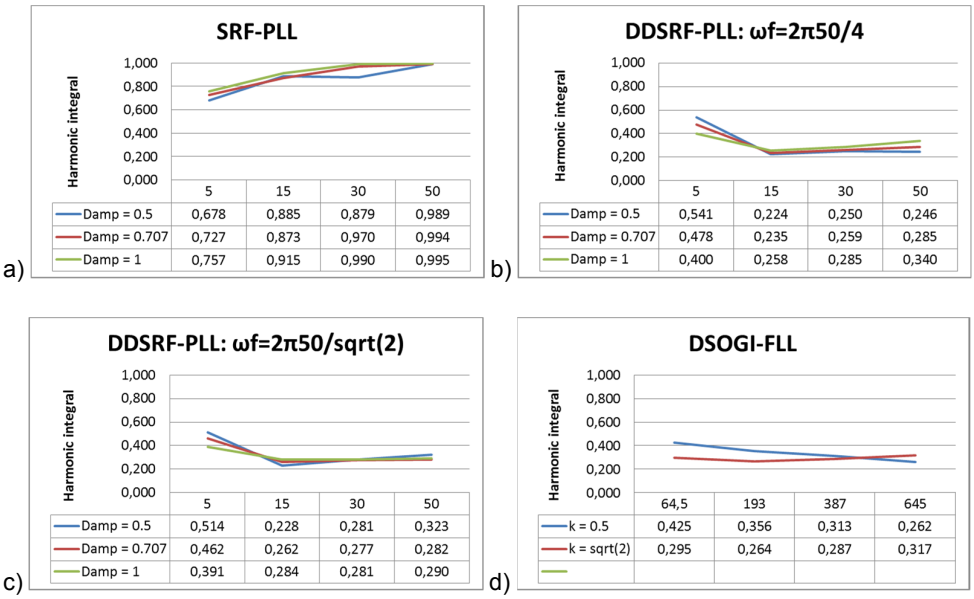

Fig. 3.13. Harmonic integrals under two-phase fault: a) SRF-PLL, b) DDSRF-PLL ω_f =2π50/4, c) DDSRF-PLL ω_f =2π50/√2, d) DSOGI-FLL.

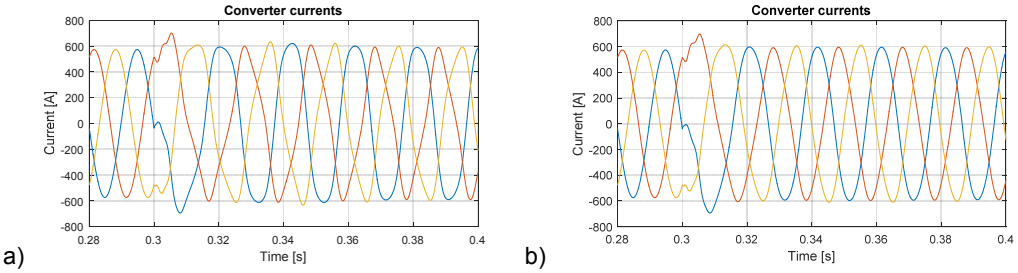

Fig. 3.14. Converter currents under asymmetrical fault: a) worst result, b) best result.

3.3.3 Presence of network voltage harmonics

The grid voltage is affected by 5th-harmonic in the following simulations. The level of the 5th-voltage harmonic measured from the primary side of the wind turbine transformer was 5.93% without the wind turbine connection. The limit for 5th-voltage harmonic in a medium voltage network defined in EN 50160 is 6%. [127] Only weak feeder 1 in the network model is in operation. Total harmonic distortion (THD) is used to measure the quality of the converter currents. THD is measured using Matlab Simulink library block and it is defined as

$$\mathrm{THD} = \frac{I_\mathrm{h}}{I_\mathrm{f}} = \frac{\sqrt{I_2^2 + I_3^2 + \ldots + I_\mathrm{n}^2}}{I_\mathrm{f}}, \tag{3.2}$$

where I_h is harmonic RMS current, I_f is RMS value of fundamental frequency current and n is number of harmonic component.

The normalized THDs under the presence of 5$^{\mathrm{th}}$-voltage-harmonic are shown in Fig. 3.15a when SRF-PLL is used. THDs using DDSRF-PLL are shown in Figs. 3.15b and c. THD of the converter current increases significantly with both methods as ω_h and ς increases, because of the decreased harmonic rejection. The decoupling network used in DDSRF-PLL cancels only the negative sequence component so the rejection of other harmonics is directly determined by the tuning of PLL. In addition, the positive sequence component of the grid voltage is close to nominal in this case, so the gain normalization does not have impact. Therefore, the simulation results between both methods are almost identical.

The simulation results with DSOGI-FLL are shown in Fig. 3.15d. The harmonic rejection capability depends on k_SOGI, while Γ has no influence. This is expected because the bandwidth of the bandpass filter is determined by k_SOGI as illustrated in Fig. 2.15.

According to the simulation results of Figs. 3.15a-d, the presence of the network voltage harmonics may be the limiting factor for ω_h and ς, when SRF-PLL or DDSRF-PLL is used. If DSOGI-FLL is used, k_SOGI may need to be limited. The lowest THD in the simulations is achieved, when SRF-PLL is used with parameters ω_h=2π*(5 Hz), ς=0.5, resulting THD of 1.19%. The highest THD value is 3.56%, when SRF-PLL is used with ω_h=2π*(50 Hz) and ς=1. The THD values are significantly influenced by the bandwidth of the reactive power controller, which is in operation during these simulations. For example, the THD values are 5.4% and 7.28%, if the controller gain is increased from 0.45 to 3 and the integration time is reduced from 40 ms to 20 ms. However, this study analyzes only synchronizing methods and the controller tuning is excluded from the scope of this work.

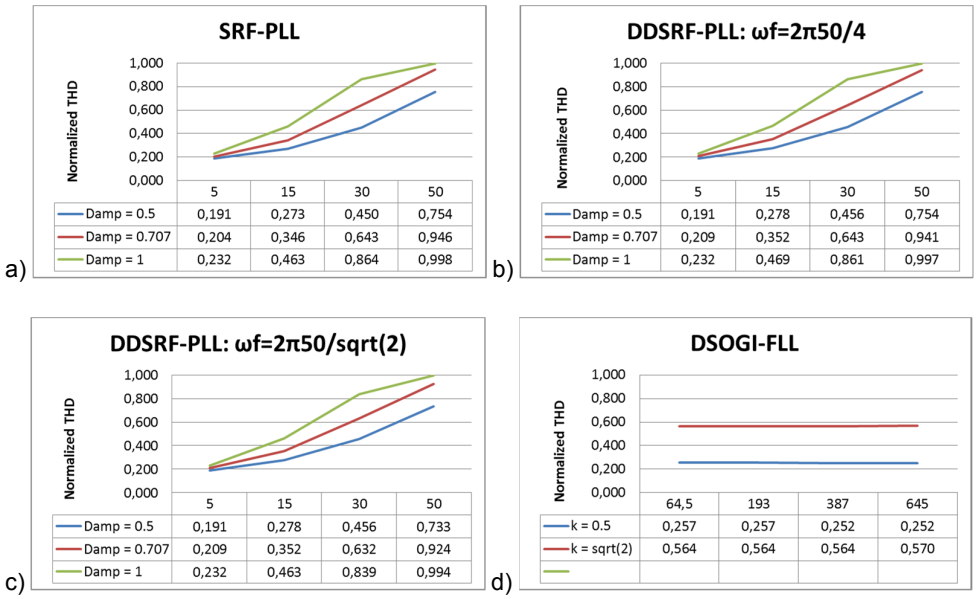

Fig. 3.15. Current THD under presence of voltage 5th-harmonics: a) SRF-PLL, b) DDSRF-PLL ω_f =2π50/4 c) DDSRF-PLL ω_f =2π50/√2, d) DSOGI-FLL.

3.3.4 Overall performance and parameter sensitivity

The simulation results show that the parameter selection is a trade-off between the speed of the operation and the harmonic content of the generated currents. The normalized harmonic integrals of first two cases and the normalized THD values of the third case are added together in order to find parameters, which would minimize the converter-current harmonics, when all cases are taken into account.

The overall current harmonics increase as the SRF-PLL bandwidth increase as can be seen from Fig. 3.16a. Although the performance with high bandwidth is better during the symmetrical voltage dips and during the voltage recovery, the poor performance under the unsymmetrical voltage dips and under the presence of network-voltage harmonics may force to select low values for ω_h and ς. This is important to notice because the unsymmetrical voltage dips are more common than symmetrical voltage dips. In this study, the lowest aggregated harmonic integral value for SRF-PLL is achieved using parameters ω_h = 2π*5 and ς = 0.5.

In the case of DDSRF-PLL, there is no reason to limit ω_h due to the performance during the unsymmetrical voltage dips. However, the performance under the presence of the voltage harmonics is identical to SRF-PLL. Thus, the performance decreases significantly,

if too high bandwidth is used. The lowest aggregate value for DDSRF-PLL is found with parameters $\omega_n = 2\pi*15$, $\varsigma = 0.5$, $\omega_f = 2\pi*15/4$.

The lowest aggregate value for DSOGI-FLL is achieved by using parameters: $k_{SOGI} = 0.5$, Γ=387. It can be concluded that the best results obtained using DDSRF-PLL and DSOGI-FLL are in great agreement with each other.

a)

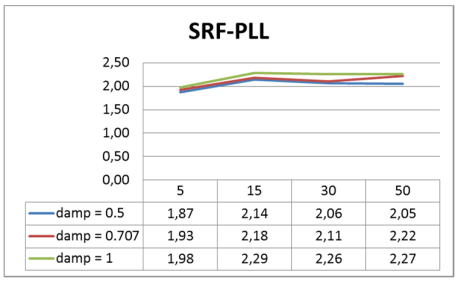

	5	15	30	50
damp = 0.5	1,87	2,14	2,06	2,05
damp = 0.707	1,93	2,18	2,11	2,22
damp = 1	1,98	2,29	2,26	2,27

b)

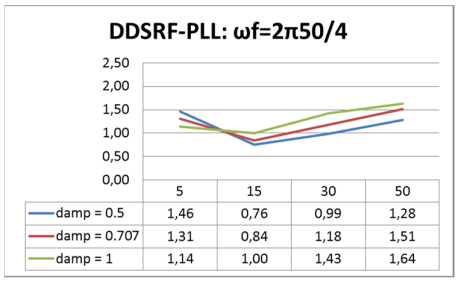

	5	15	30	50
damp = 0.5	1,46	0,76	0,99	1,28
damp = 0.707	1,31	0,84	1,18	1,51
damp = 1	1,14	1,00	1,43	1,64

c)

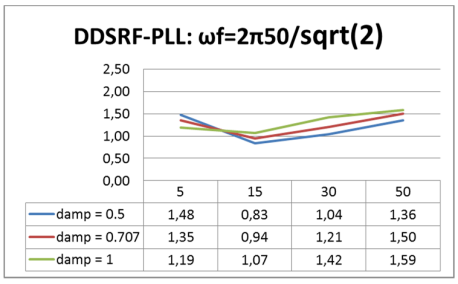

	5	15	30	50
damp = 0.5	1,48	0,83	1,04	1,36
damp = 0.707	1,35	0,94	1,21	1,50
damp = 1	1,19	1,07	1,42	1,59

d)

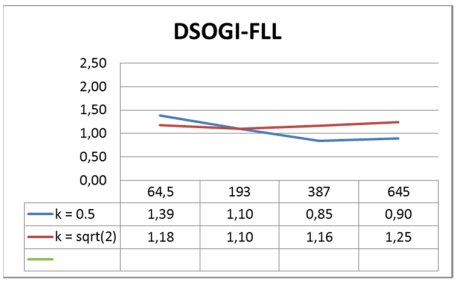

	64,5	193	387	645
k = 0.5	1,39	1,10	0,85	0,90
k = sqrt(2)	1,18	1,10	1,16	1,25

Fig. 3.16. Sum of normalized results: a) SRF-PLL, b) DDSRF-PLL $\omega_f = 2\pi50/4$ c) DDSRF-PLL $\omega_f = 2\pi50/\sqrt{2}$, d) DSOGI-FLL.

3.3.5 Conclusion of investigation 2

It is shown in Investigation 2 that the bandwidth of SRF-PLL needs to be limited due to the poor performance during the unbalanced grid faults and under the presence of grid-voltage harmonics. When DDSRF-PLL is used, the limiting factor of the PLL bandwidth is the harmonics. The performance of DSOGI-FLL is determined by the bandpass filter gain and bandwidth of the normalized FLL gain. The increase of the bandpass filter gain leads to deterioration of harmonic performance. However, the operation becomes faster especially if the normalized FLL gain is small. It is shown that the performance of DDSRF-PLL and DSOGI-FLL are in agreement with each other although DDSRF-PLL gives slightly faster responses.

The simulation results of this investigation show that the synchronization carried out by using DDSRF-PLL or DSOGI-FLL shows superior performance compared to the traditional SRF-PLL method during the grid voltage disturbances. The main reasons are the gain normalization and the canceling of the negative sequence component from the synchronization angle.

The simulation results of this investigation give an indication on how the tuning parameter selection (ς, ω_h, ω_f, k_{SOGI}, Γ) of the synchronizing methods impacts on the wind turbine operation during the grid disturbances. However, the parameter selection should always be done by taking into account the customer specifications in practical cases, network parameters and the general level of the voltage harmonics on the point of connection. For example, if the network is strong or the harmonic level is small, it is possible to increase the bandwidth without significant influence on the power system operation due to the decreased current quality. Although this investigation considers only the impact of the tuning of the different synchronization methods, it should be kept in mind that the overall performance of the wind turbine during the grid faults are also affected by the tuning of the control system controllers. However, the tuning of the control system controllers is out of the scope of this thesis. This is reasonable, because tuning of controller in synchronization system and tuning of control system controllers are different tasks. The simulation results in this chapter can be considered as general results considering the synchronization part.

4. RTDS/dSPACE real-time simulation environment

This chapter focuses on the real-time simulation environment constructed at TUT laboratory, which uses RTDS and dSPACE simulators. This chapter is organized as follows. The main features of the real-time environment are described in Section 4.1. The practical implementation of the real-time simulation environment for the FPC wind turbine concept, which uses PMSG, is presented in Section 4.2. In Section 4.3, the real-time simulation results during the three-phase short-circuit and automatic reclosing are compared to the simulation results obtained by using the identical model implemented in Matlab Simulink in order to verify the real-time model.

The practical implementation of the real-time environment for the DFIG wind turbine model presented in Chapter 2 is described in Appendix E. The real-time model is used in analysis of the impact of the transient flux compensation control on the operation of DFIG during the symmetrical grid fault in Section 4.4. The DFIG operation during a voltage recovery is analyzed in Section 4.5.

4.1 Features of real-time simulation environment

The real-time simulation environment consists of a dSPACE controller board and RTDS. dSPACE is used to simulate the operation of the FPC wind turbine, which is modeled in Matlab Simulink. The dSPACE simulation is controlled by using ControlDesk software, which allows the management of the simulation by providing a virtual control panel with online parameter changing and signal supervision. RTDS is used to simulate the power system, which is modeled in Draft mode of RSCAD software. The Draft mode contains a library for power and control system component models. The online control and monitoring are performed in Runtime mode of RSCAD. Typical control actions of the RTDS simulation are the generation of symmetrical or unsymmetrical faults, the connection of heavy loads or the status changes of circuit breakers installed in the modeled network.

The main benefits of the real-time simulation environment are the sharing of the computation power between two simulators and the decreased simulation time compared to the offline simulations carried out, for example, by using the Matlab Simulink or PSCAD simulators. In addition, the tuning of the control parameters and the testing of the control algorithms during the different grid conditions become easier and faster in the real-time environment. Furthermore, the use of real devices such as electric machines, electric loads or protection relays as a part of the tests is possible. The drawbacks of the

environment are the limited simulation model and time step of the individual simulators and costs of the real-time simulators.

4.2 Practical implementation of real-time environment for FPC wind turbine

The real-time model the FPC wind turbine is shown in Fig. 4.1. The mathematical background of the model is presented in Chapter 2, and the network model as well as the model parameters are presented in Appendix D, respectively.

The LC part of the wind turbine filter is simulated in dSPACE and the network-side inductor is simulated by RTDS. dSPACE receives synchronizing-point voltages $u_{\mathrm{sync(a,b,c)}}$ and currents $i_{\mathrm{L2(a,b,c)}}$ from RTDS and sends the voltage over filter capacitor $u_{\mathrm{fC(a,b,c)}}$ into RTDS. As can be seen from Fig. 4.2, the data transmission between the simulators is performed by using analog signals. The output-voltage range of AD and DA cards in RTDS and dSPACE is ±10 V making the scaling of the transferred signals to be straightforward. Due to the interface selection between the two simulators, the wind turbine is modeled as a voltage source in RTDS. The simulation time steps used in RTDS and dSPACE are 50 µs and 100 µs, respectively.

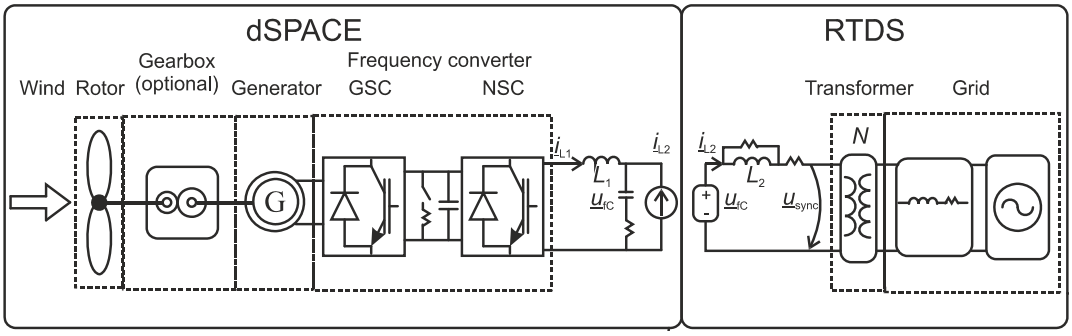

Fig. 4.1. FPC wind turbine real-time model.

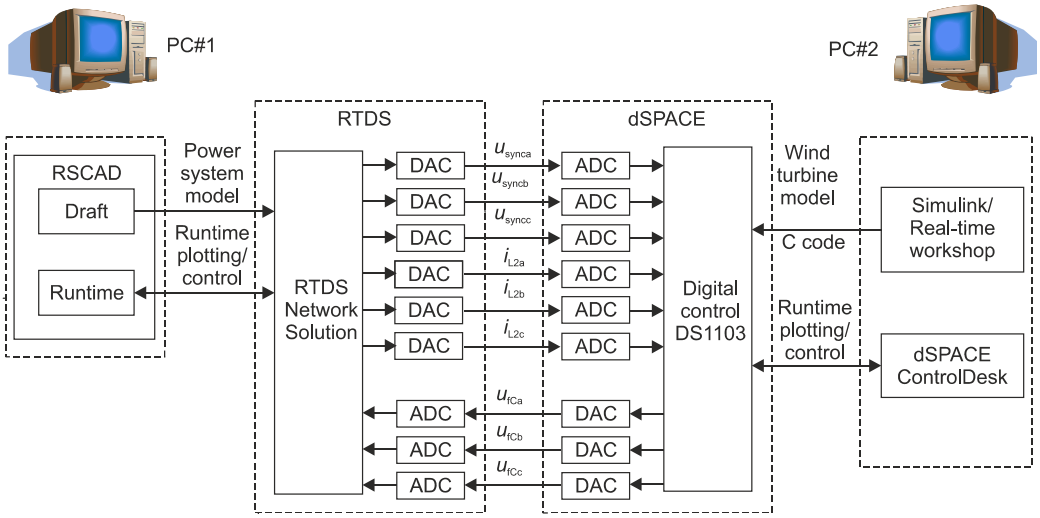

Fig. 4.2. Practical implementation of real-time simulation environment for FPC wind turbine.

4.3 Investigation 3: Verification of real-time environment

In this investigation, the real-time model of the FPC wind turbine is verified against the corresponding Matlab Simulink model. In order to achieve accurate reference results, the simulation time step of Simulink model is set to 10 µs. Because of the longer step-sizes of the real-time simulators and the transfer of the measured signals between the simulators, there are delays in the real-time simulation. This delay is compensated by shifting the angle of the voltage vector $\underline{u}_{fC}$, which is fed from dSPACE to RTDS. The selected angle shift corresponds to the delay of 400 µs.

The simulated wind speed is 12 m/s. The verification is done by simulating a three-phase fault occurring at the transformer primary at 419.954 s. The fault is cleared by the automatic reclosing after 300 ms from the beginning of the fault. The GSC current references are set to zero after 50 ms from the fault beginning. Hence, the wind turbine does not disturb the automatic reclosing sequence and the active power transfer into the DC-link is avoided. During the voltage recovery, the converter references are increased in a controlled manner.

The verification simulation results are shown in Fig. 4.3, where the left-hand side and right-hand side results are obtained from Simulink and RTDS/dSPACE, respectively. The synchronizing-point voltage A-phase drops to zero as a result of the voltage dip as shown in Figs. 4.3a-b. The converter currents, shown in Figs. 4.3c-d, increase to limit value after the voltage dip, because the DC-link voltage controller attempts to maintain the power

balance between the generated power and the power transferred into the grid. The instantaneous active power p transferred into the grid during the fault is zero due to the zero voltage in the transformer primary as can be seen from Figs. 4.3e-f. Therefore, all generated power during the first 50 ms after the fault is stored into the DC-link capacitors of the frequency converter. As a result, the DC-link voltage u_{dc}, shown in Figs. 4.3g-h, increases and exceeds the braking chopper activation level (1300 V). As the GSC current references are set to zero, all the energy from the wind is stored into the rotating mass of the wind turbine rotor. Hence, the rotational speed ω_t, shown in Figs. 4.3i-j, increases and the acceleration continues as long as the mechanical torque of the rotor is greater than the electrical torque controlled by GSC. After the voltage recovery, the converter currents are increased in controlled manner back to original operation point. However, it can be seen that the converter current and instantaneous active power transients are greater in RTDS/dSPACE-environment. The transients in the converter current and in the instantaneous active power during the voltage recovery are presented in Figs. 4.3k-l and in Figs. 4.3m-n, respectively, with different time scale compared to other figures. It can be seen that the transient in converter current is approximately two times larger in RTDS/dSPACE than in Simulink. In addition, the transients in instantaneous active power in Simulink lasts less than 10 ms, while the transients in RTDS/dSPACE decays after approximately 20 ms.

The simulation results obtained using the Simulink and RTDS/dSPACE environments are in agreement with each other during the steady state operation. The used delay compensation method is effective during steady state or during slowly varying operation. However, the voltage vector length changes rapidly during the transients and the time and magnitude of change are impossible to predict. Therefore, the transients in the converter currents and instantaneous active power are greater in the RTDS/dSPACE-environment. The delay between the real-time simulators decreases if the simulation step sizes decreases. However, due to the large size of the wind turbine and its control-system model, it was not possible to decrease the simulation step size of dSPACE.

Another issue related to RTDS/dSPACE-environment is the asynchronous operation of the simulators. As the simulation time increases, the simulation steps of the simulators drifts with respect to each other. As a result, the delay is not constant. The impact of varying delay is not of significant importance to the simulation results. However, the varying delay is avoided by feeding an external interrupt signal from RTDS into dSPACE to synchronize the simulation steps of the simulators. This interrupt signal is used in the following real-time simulations of this thesis.

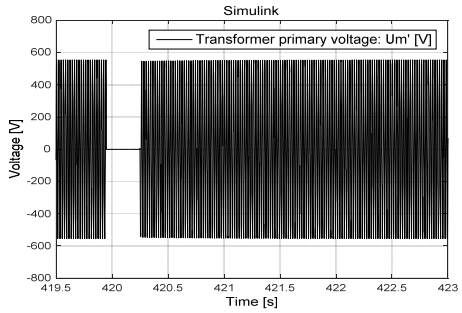
Simulink
Transformer primary voltage: Um' [V]
Voltage [V]
Time [s]

a)

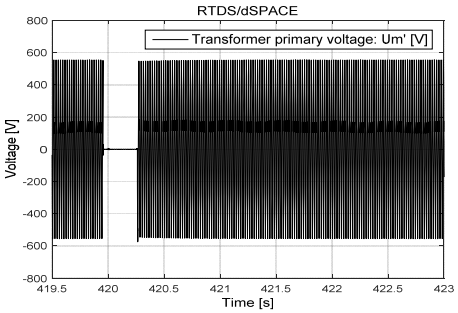
RTDS/dSPACE
Transformer primary voltage: Um' [V]
Voltage [V]
Time [s]

b)

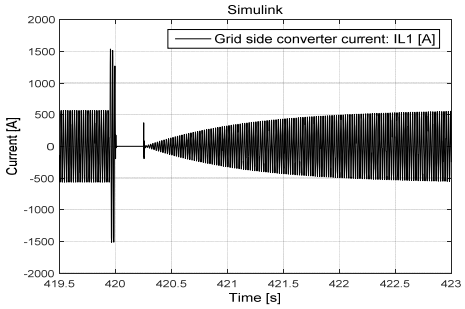
Simulink
Grid side converter current: IL1 [A]
Current [A]
Time [s]

c)

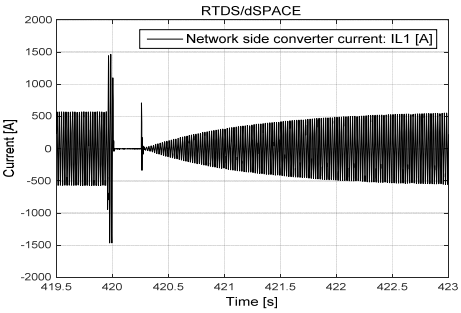
RTDS/dSPACE
Network side converter current: IL1 [A]
Current [A]
Time [s]

d)

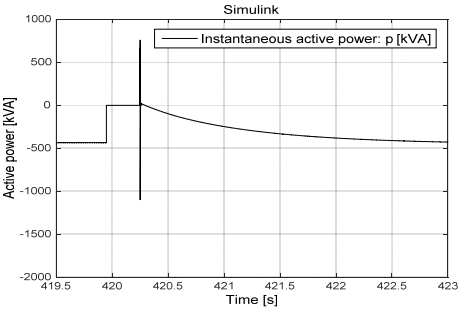
Simulink
Instantaneous active power: p [kVA]
Active power [kVA]
Time [s]

e)

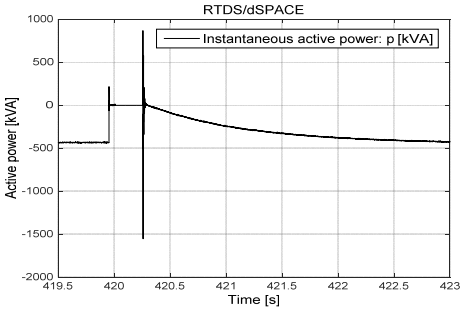
RTDS/dSPACE
Instantaneous active power: p [kVA]
Active power [kVA]
Time [s]

f)

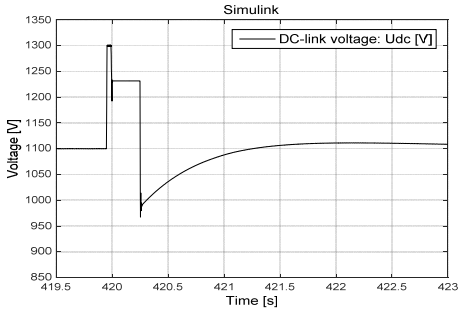
Simulink
DC-link voltage: Udc [V]
Voltage [V]
Time [s]

g)

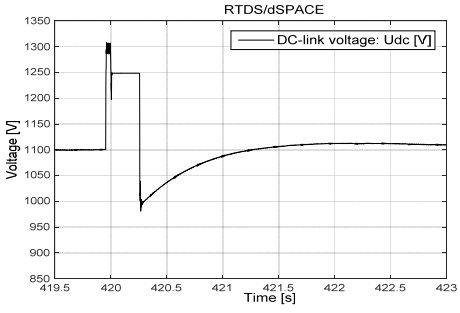
RTDS/dSPACE
DC-link voltage: Udc [V]
Voltage [V]
Time [s]

h)

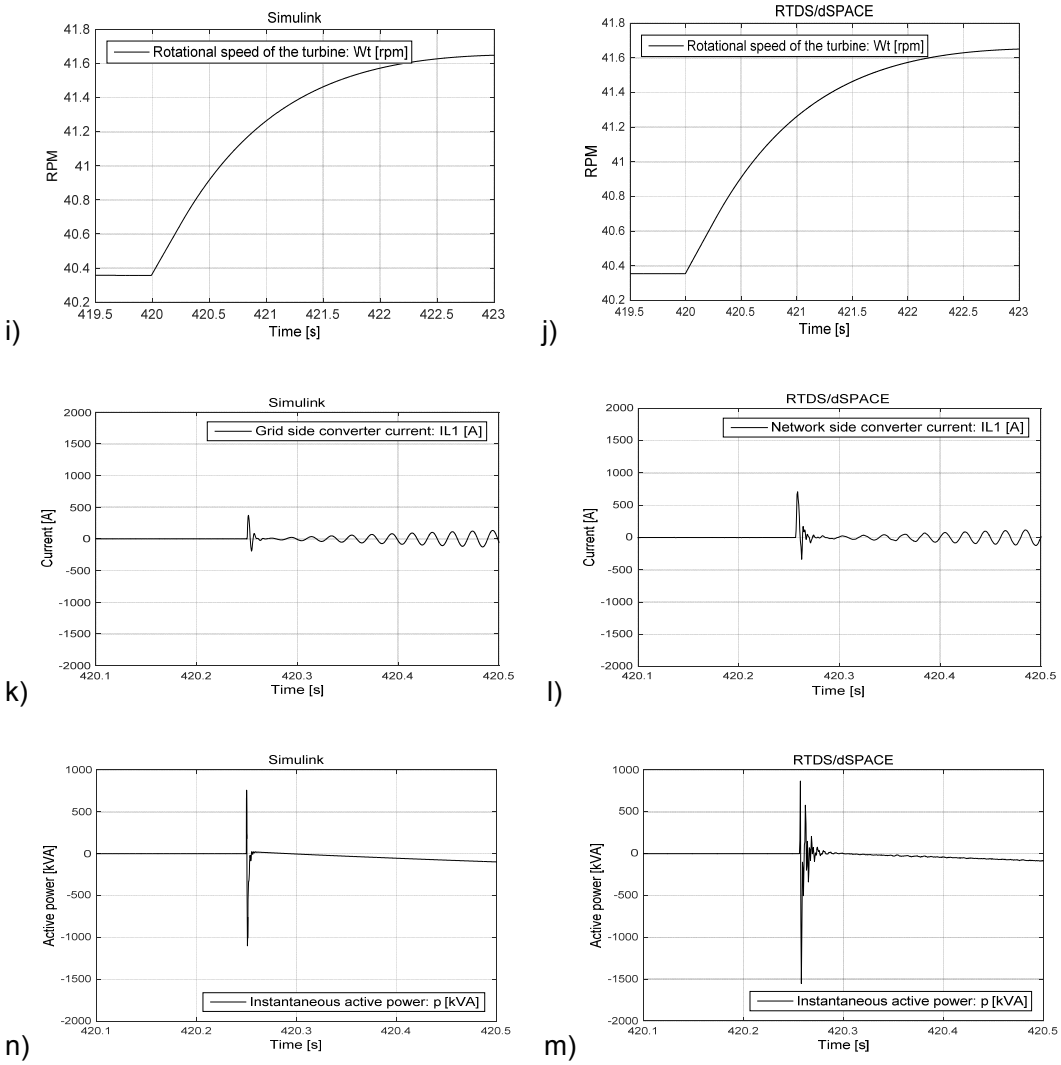

Fig. 4.3. Transformer primary A-phase voltage: a) Simulink, b) RTDS/dSPACE; converter A-phase current: c) Simulink, d) RTDS/dSPACE; instantaneous active power p: e) Simulink, f) RTDS/dSPACE; DC-link voltage u_{dc}: g) Simulink, h) RTDS/dSPACE; Angular frequency of turbine ω_t: i) Simulink, j) RTDS/dSPACE; transient of i_a: k) Simulink, l) RTDS/dSPACE; transient of p: n) Simulink, m) RTDS/dSPACE.

In spite of the delay, which misinterprets the simulation results during the transients, the advantages of the real-time environment became clear. It took 4 hours and 28 minutes in Simulink to simulate 430 seconds by using real-time environment. In addition, the significant benefit is the possibility to tune the control parameters of the PI-controllers online.

4.3.1 Conclusion of Investigation 3

It is shown that the RTDS/dSPACE simulation results are in sufficient agreement with Simulink results in a steady state mode of operation. The transients in the RTDS/dSPACE-environment are greater and last longer because of the longer simulation step-sizes (100 µs in dSPACE, 50 µs in RTDS and 10 µs in Simulink) and the delay (≈400 µs) between the simulators. In general, the simulation results show that the differences between the simulation environments are of no significant importance from the power system analysis point of view, because the transients in the RTDS/dSPACE environment lasts approximately one grid frequency cycle. However, when operation of power electronic devices during transients are investigated, the real time simulation environment cannot be considered truly reliable. With this environment, the capability of control system to limit currents through IGBTs, for example during voltage recovery, cannot be reliably studied. As a conclusion, it can be stated that the real-time simulation environment is almost as reliable environment for studies of the interactions between wind turbines and network as Simulink, which requires much more simulation time. With the real-time environment it is possible to test and improve control and protection functions of the wind turbine during different network disturbances with reasonable simulation time.

4.4 Investigation 4: Operation of DFIG during symmetrical voltage dip and transient flux compensation control

In this investigation, the operation of the DFIG wind turbine during the symmetrical voltage dip is analyzed. The purpose of this investigation is to show the impact of transient flux on the operation of the wind turbine. The DFIG and grid model in the real-time simulation environment are described in Appendix E.

The stator flux oriented control system of DFIG is depicted in Fig. 2.7. The stator flux can be directly computed from the measured stator currents and voltages. [63, 128] However, the stator flux angle suffers from sudden changes during the grid voltage transients due to the steps in the grid voltage angle or continuous oscillations during the grid voltage unbalance due to the presence of negative sequence component. As a result, the frequency of RSC reference frame is not constant, which causes nonlinear behavior of the angle θ_{sf}. In order to avoid this, the control system, in this thesis, is oriented to the positive sequence component of the stator flux by using frequency adaptive DSOGI-FLL. The use of DSOGI-FLL is beneficial also, because its outputs can be used to compute the transient flux for the transient flux compensation control. Thus, there is no need for external transient flux extraction schemes as presented in [55, 109]. Another benefit in using DSOGI-FLL is

the elimination of the need of bandpass filter in order to eliminate the DC offset of the integrals shown in Eqs. 2.38-2.39. For example in [128], the bandpass filter with cut-off frequencies 0.5Hz and 1 Hz needed to be used for this purpose.

4.4.1 DFIG operation during symmetrical voltage dip

In steady state operation, the three-phase stator voltages generate flux linkage to the generator stator, which rotates at stator voltage fundamental frequency. In addition, the magnitude of the stator flux linkage is proportional to the stator voltages. A symmetrical voltage dip in the stator terminals decreases instantaneously the magnitude of the rotating flux. However, according to the theorem of a constant flux linkage, the flux linkage of any closed circuit of finite resistance and electromotive force cannot change instantly. [129] Thus, the total stator flux linkage does not change due to the voltage dip even though the rotating part changes. The difference between the total stator flux linkage and the remaining rotating flux linkage is called natural or transient flux linkage, because it appears only during the voltage transients. The angular frequency of the transient flux is zero and it gets its maximum value in the beginning of the voltage dip. After the voltage dip, the transient flux decays depending on the WRIG inductance and resistance.

Induced voltages to the WRIG rotor are proportional to the stator voltage, stator and rotor turns ratio as well as angular slip frequency. The slip frequency is defined as the difference between the angular frequency of the rotating air gap flux and the angular frequency of the generator rotor. Due to the zero frequency of the transient flux, the slip frequency increases to rotor frequency when transient flux appears. Therefore, the transient flux may induce higher voltages to the rotor circuit than RSC can generate from the available DC-link voltage. Hence, RSC cannot control the rotor currents anymore and the currents cannot be limited.

4.4.2 Control and protection of DFIG during symmetrical voltage dip

The wind turbine LVRT strategy used in this chapter contains the active crowbar protection and reactive power injection utilizing both NSC and RSC. The modified crowbar structure, which principle is illustrated in Fig. 4.4, is used, where the crowbar resistance is set to 0.4 pu and 0.8 pu after the fault and after the voltage recovery, respectively. The crowbar is activated after the fault by closing the switch S1 if the rotor currents exceeds the crowbar trigger limit. After the rotor currents are decreased enough, S1 is opened again and RSC starts to overexcite the rotor windings, which causes capacitive reactive current flow to the grid for voltage support purposes. After the crowbar is deactivated during the fault, the crowbar resistance is increased by opening the switch S2. This leads to crowbar

resistance of (R1+R2) during the voltage recovery. The reason for this arrangement is discussed in Investigation 5.

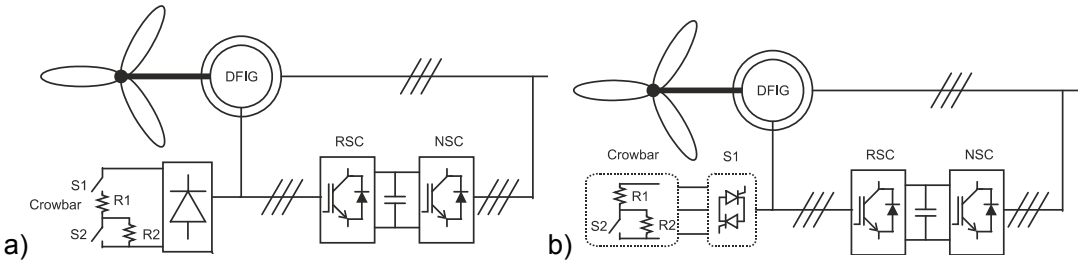

Fig. 4.4. Modified crowbar structure.

The crowbar is activated if the measured rotor currents exceed the current capability of RSC, which is in this case 900 A_{rms} (1270 A_{peak}). The control target of RSC is to fully prioritize the reactive power injection during the fault. Thus, the active current reference is set to zero during the fault. The reactive power injection of NSC is implemented so that the active current component i_{L1d}^{*} is prioritized in order to maintain the DC-link voltage at the reference value. In other words, the reactive current reference of NSC is the difference between current capacity of NSC (600 A_{rms}) and the measured active current and it can be computed as follows

$$i_{L1q}^{*} = \sqrt{\left({i_{max}}^{2} - {i_{L1d}^{*}}^{2} \right)} = \sqrt{\left(\left(\sqrt{2} * 600\,\mathrm{A} \right)^{2} - {i_{L1d}^{*}}^{2} \right)} \ . \qquad (4.1)$$

4.4.3 Impact of transient flux during symmetrical voltage dip

The three-phase voltage dip occurs in the high voltage network shown in Appendix E. The residual voltage during the fault is 20% of the nominal value. The fault begins at 5.151 s and lasts for 300 ms. The simulation results are shown in Fig. 4.5. The rotor voltages, shown in Fig. 4.5b, become distorted after the voltage dip. The frequency of the rotor voltages in rotor coordinate is proportional to the slip of the generator. The rotor voltage frequency prior to fault is negative sequence 10.5 Hz. However, 60.5 Hz component appears in the rotor voltages during the fault, which corresponds to the electrical frequency of the generator. Because the frequency of the rotor voltages is proportional to the slip, the 60.5 Hz rotor-voltage component can appear only if there is a non-rotating stator flux component. The non-rotating flux component is the transient flux, which is illustrated in Fig. 4.5c in stator flux reference frame. Because the reference frame rotates with 50 Hz

frequency, the transient flux appears as negative sequence 50 Hz component in the stator flux reference frame, i.e. beta leads alpha.

The increased rotor currents activate the crowbar protection after the fault. When the currents have decreased enough, the crowbar is deactivated and RSC is connected back in operation. As can be seen from Figs. 4.5d and e, the on-fault rotor and grid currents contain harmonics caused by the transient flux. The transient flux generates also the 50 Hz component to the measured rotor current components i_{sx} and i_{sy} as well as on the instantaneous reactive power, which is shown in Fig. 4.5f. In order to avoid repetitive crowbar activation during the fault due to the 50 Hz component in currents the reactive current reference need to be set to a lower value than the current capacity of RSC. In this case, the reference was set to 1070 A_{peak} while the current capacity value is 1270 A_{peak}. This means that the reactive current injection during the fault is not maximized.

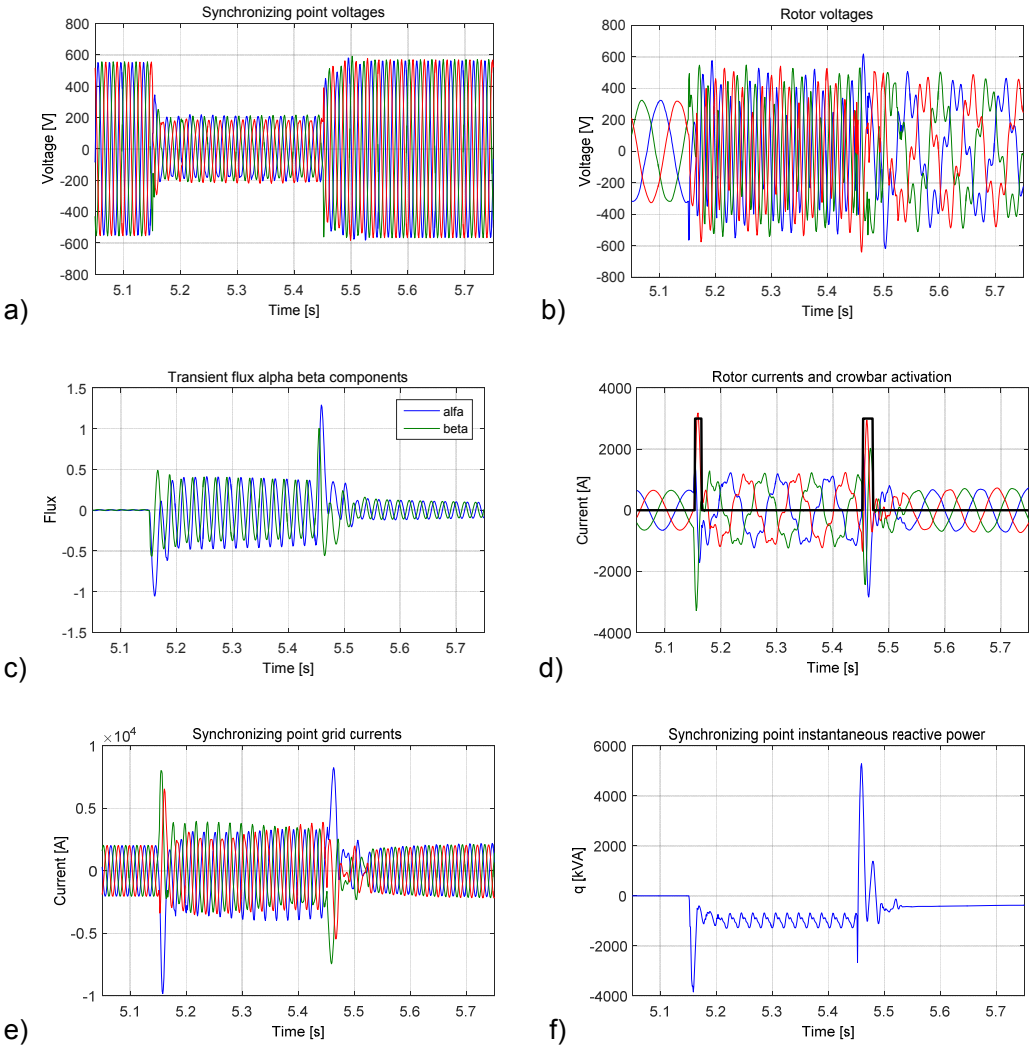

Fig. 4.5. DFIG during symmetrical voltage dip: a) synchronizing point voltages, b) rotor voltages, c) transient flux, d) rotor currents and crowbar activation, e) synchronizing point currents, f) synchronizing point instantaneous reactive power.

4.4.4 Transient flux compensation control

The transient flux causes poor harmonic performance in addition to the limitation of the reactive power injection as shown in Section 4.4.3. In this section, the control system is modified in order to compensate the impact of the transient flux on the operation of DFIG during the symmetrical dip.

The modified control system of RSC including the transient flux compensation control is shown in Fig. 4.6. DSOGI-FLL is used to separate the positive and negative sequence components from the flux. In case of the symmetrical voltage dip in a non-polluted network,

the negative sequence flux linkage ψ_s^- is zero and the transient flux linkage ψ_{stf} can be given as follows

$$\underline{\psi}_{stf} = \underline{\psi}_s - \underline{\psi}_s^+ - \underline{\psi}_s^- = \underline{\psi}_s - \underline{\psi}_s^+ . \tag{4.2}$$

A rotor flux linkage vector can be given as

$$\underline{\psi}_r' = L_r' \underline{i}_r' + L_m \underline{i}_s = \frac{L_m}{L_s}\underline{\psi}_s + L_r' \underline{i}_r' - \frac{L_m^2}{L_s}\underline{i}_r' = \frac{L_m}{L_s}\underline{\psi}_s + \sigma L_r' \underline{i}_r' . \tag{4.3}$$

The rotor flux linkage can be divided into sequence components as follows

$$\underline{\psi}_r' = \underline{\psi}_r^+' + \underline{\psi}_r^-' + \underline{\psi}_{rtf}' = \underline{\psi}_r^+' + \underline{\psi}_{rtf}' = \frac{L_m}{L_s}\left(\underline{\psi}_s^+ + \underline{\psi}_{stf}\right) + \sigma L_r' \left(\underline{i}_r^+' + \underline{i}_{rtf}'\right), \tag{4.4}$$

where ψ_r^+' and i_r^+' correspond to positive sequence rotor flux and current, respectively. The ψ_{rtf}' and i_{rtf}' are the transient flux and current terms, respectively, and ψ_r^-' is the negative sequence flux, which is zero during the symmetrical voltage dip. The superscript ‘ means that the measures are reduced to the stator. The purpose of the transient flux compensation control is to minimize the impact of the transient flux on the generator rotor. In other words, the aim is to control the transient flux on the rotor to zero

$$\underline{\psi}_{rtf}' = \frac{L_m}{L_s}\underline{\psi}_{stf} + \sigma L_r' \underline{i}_{rtf}' = 0 . \tag{4.5}$$

The rotor current vector, which can be used to compensate the transient flux, can now be given as

$$\underline{i}_{rtf} = \frac{\underline{i}_{rtf}'}{N} = -\frac{L_m}{N L_s \sigma L_r'}\underline{\psi}_{stf} = -\frac{L_m}{N L_s \sigma L_r'}\left(\underline{\psi}_s - \underline{\psi}_s^+\right). \tag{4.6}$$

In the proposed LVRT control strategy, the transient flux compensation control is prioritized during the fault. After deactivation of the crowbar and activation of RSC, the computed transient flux compensation current components $i_{rtf,x,y}$ are set as the references for the current controllers. As the transient flux declines, the current needed to cancel the transient flux decreases. When the magnitude of the compensating current vector $|\underline{i}_{rtf}|$ is smaller than the current capacity of RSC, the surplus capacity can be utilized for the reactive current injection. In other words, the reactive current reference is the difference between the RSC current capacity and the transient flux compensating current reference.

The active current reference $i_{ry}{}^{*}$ is set to zero during the fault because the reactive power injection is prioritized. Hence, the current references during the voltage dip are

$$i_{rtf,x}{}^{*} = -\frac{L_m}{NL_s\sigma L_r'}\psi_{stf,x}\,, \tag{4.7}$$

$$i_{rtf,y}{}^{*} = -\frac{L_m}{NL_s\sigma L_r'}\psi_{stf,y}\,, \tag{4.8}$$

$$i_{rx}{}^{*} = \sqrt{(i_{rmax})^2 - \left(\left|\underline{i}_{rtf}{}^{*}\right|\right)^2}\,, \tag{4.9}$$

$$i_{ry}{}^{*} = 0\,, \tag{4.10}$$

where i_{rmax} is the current capacity of RSC and $\left|\underline{i}_{rtf}{}^{*}\right|$ is the magnitude of the transient current vector. After the transient flux is canceled, the transient current is zero and the whole current capacity can be utilized for reactive current injection.

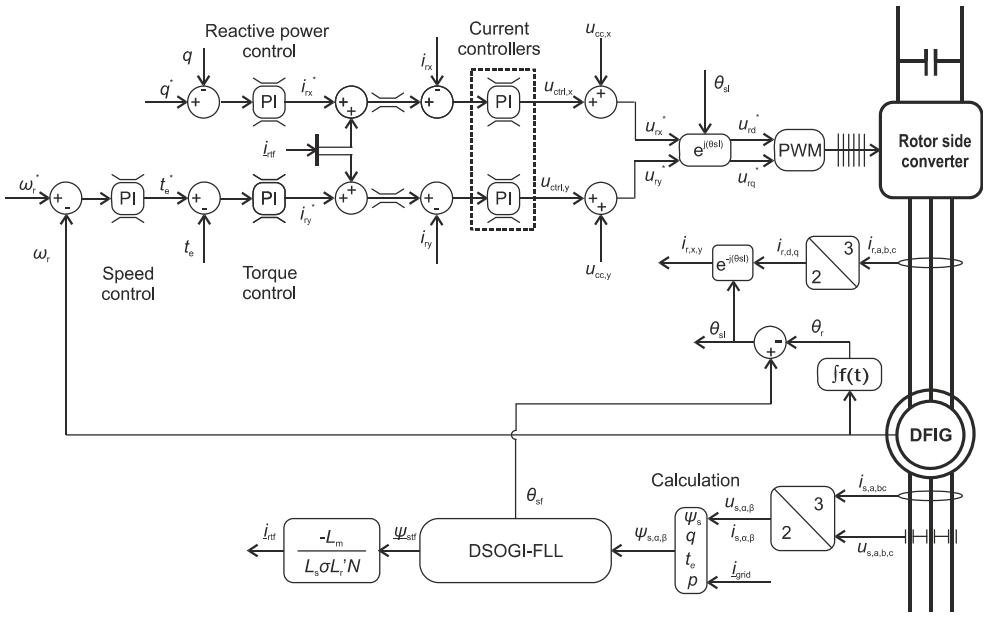

Fig. 4.6. Control system of RSC with transient flux compensation control.

Next, the same fault as in Section 4.4.3 is simulated with the active crowbar protection and the transient flux compensation control. The simulation results are shown in Fig. 4.7. The transient flux is effectively cleared after crowbar deactivation as shown in Fig. 4.7b. As a result, the 60.5 Hz component from the rotor voltages is removed and the rotor voltages, shown in Fig. 4.7c, as well as the rotor currents, presented in Fig. 4.7d, consist of only

positive sequence component. The RSC reactive current reference is now set to 1270 A instead of previous 1070 A without repetitive crowbar activation. Thus, the reactive power injection is maximized during the dip as can be seen from Fig. 4.7e, which is desirable from the grid codes point of view. Furthermore, the 50 Hz oscillating part in the instantaneous reactive power is removed. The grid currents, shown in Fig. 4.7f, contain only positive sequence component indicating improved power quality. Therefore, the synchronizing-point voltages, shown in Fig. 4.7a, consists of only fundamental frequency positive sequence component. It can be concluded that the transient flux compensation control enhances significantly the performance of DFIG during the symmetrical voltage dip.

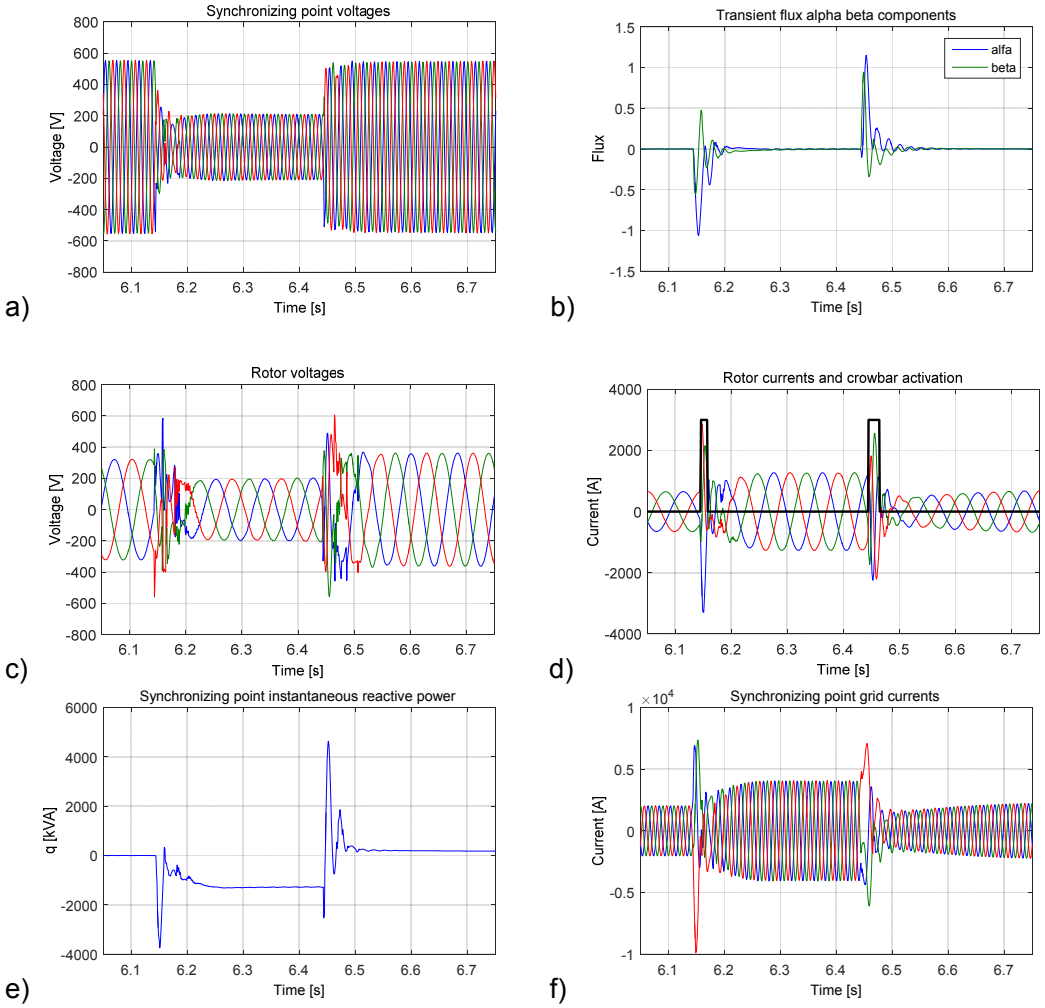

Fig. 4.7. DFIG during symmetrical voltage dip with transient flux compensation control: a) synchronizing point voltages, b) transient flux, c) rotor voltages, d) rotor currents and crowbar activation, e) synchronizing point instantaneous reactive power, f) synchronizing point currents.

4.4.5 Conclusion of Investigation 4

In Investigation 4, the impact of the transient flux compensation control on the operation of the DFIG wind turbine during the symmetrical voltage dip is analyzed. The investigation is carried out by using the RTDS/dSPACE real-time simulation environment.

The synchronization of RSC is oriented to the positive sequence component of the stator flux linkage utilizing the frequency adaptive DSOGI-FLL analyzed in Section 2.3.4. The outputs of DSOGI-FLL, which are positive and negative sequence components of the stator flux linkage, enable the calculation of the transient flux. Based on the estimated transient flux, the compensation current references are generated.

It is shown that the whole RSC current capacity can be utilized for the reactive power injection without a fear of repetitive crowbar activation during the symmetrical voltage dip, if the LVRT method including the transient flux compensation control is used. Thus, the reactive power injection is maximized. It can also be noticed that the transient flux compensation control enhances the quality of the generated currents during the dip.

4.5 Investigation 5: DFIG crowbar protection during voltage recovery

The DFIG grid-voltage recovery is rapid in simulations presented in Investigation 4. In this investigation, the operation of DFIG is analyzed when the traditional active crowbar structure, shown in Fig. 1.6b, is used instead of the modified structure shown in Fig. 4.4.

When the crowbar is activated, DFIG operates like an induction generator with an increased rotor resistance and, possibly, with high value of slip. The impact of the crowbar resistance on the DFIG active and reactive powers is depicted in Fig. 4.8a. The lower the crowbar resistance is, the steeper are the slip versus active and reactive power curves. As a consequence, the absorbed reactive power during the voltage recovery is significant, if small resistance is used and the generator operates with high slip. This leads to high stator currents, which causes a voltage drop over the network impedances. Therefore, the stator terminal voltages may not recover to the level prior the fault. The voltage drop is proportional to the network impedance. Thus, the problems associated to the operation during the voltage recovery are more severe, when DFIG is connected to weak network. In addition, if there are number of DFIG wind turbines operating as a wind farm, the voltage drop becomes more significant due to the aggregated reactive current absorption of DFIGs.

The active and reactive powers of the induction generator are determined by the slip and the stator voltages as can be seen from Fig. 4.8b. The decreased terminal voltage during the voltage recovery decreases the generator peak active power and peak torque. The operation becomes unstable, if the pull-out slip is exceeded. In that case, the turbine needs to be tripped in order to prevent an excessive reactive power consumption of the generator, which may lead to a voltage collapse in the worst case. The tripping of the wind turbine means unsuccessful FRT, which is against the grid codes. The curves in Fig. 4.8 are attained using induction generator, which parameters are collected in Table 4.1.

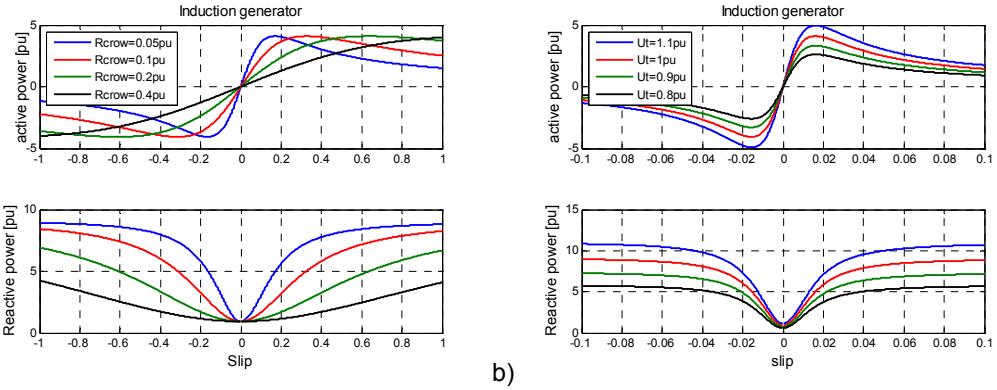

a) b)

Fig. 4.8. a) Active and reactive power of the induction generator with respect to slip and stator terminal voltages, b) active and reactive power of the induction generator with respect to slip and crowbar resistance.

Table 4.1. Induction generator parameters. [49]

S_n = 1717 [MVA]	U_n = 575 V	R_s = 0.0073 [pu]	R_r = 0.0052 [pu]
L_{sl} = 0.1766 [pu]	L_{rl} = 0.1610 [pu]	L_m = 3 [pu]	

4.5.1 Voltage recovery with varying crowbar resistance

The operation of DFIG during the identical fault compared to Investigation 4 is analyzed, when the crowbar resistance is selected to be 0.5 pu. Rotor currents, crowbar activation as well as synchronizing-point voltages and currents are shown in Fig. 4.9. Due to the low crowbar resistance, the appearing rotor currents, shown in Fig. 4.9a, are so high that the crowbar connection is prolonged. After more than 600 ms from the voltage recovery, the crowbar is deactivated. During the time of the crowbar activation, the reactive power to magnetize DFIG is taken from the grid. Thus, the post fault currents, shown in Fig. 4.9b, are high causing the voltage drop over the network impedance. This delays the voltage recovery as can be seen from Fig. 4.9c.

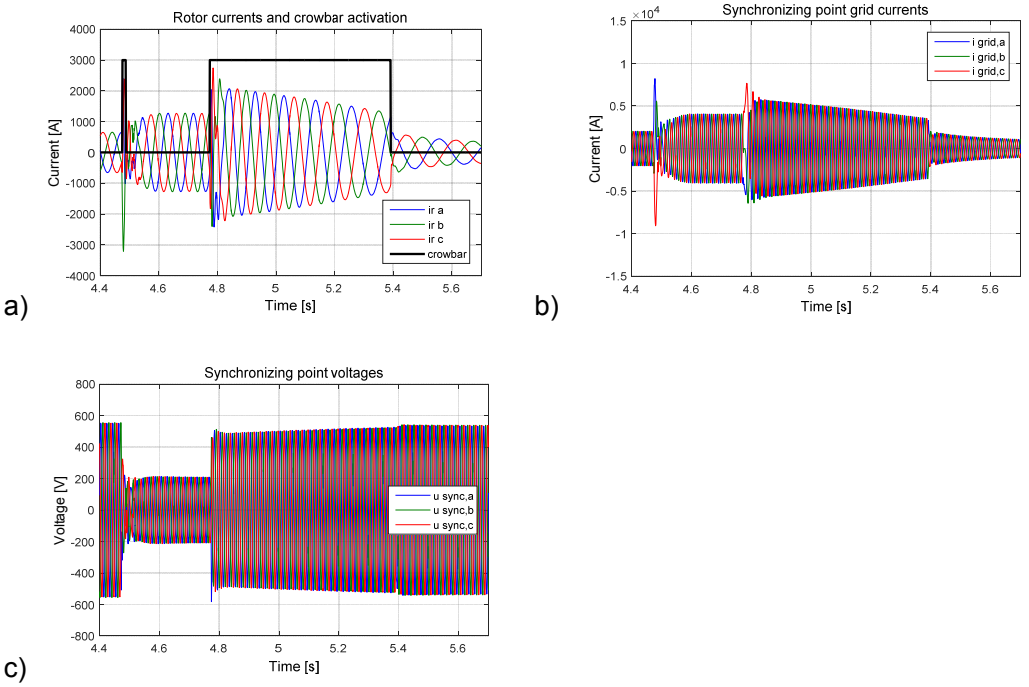

Fig. 4.9. DFIG during three-phase fault with R_{crow} = 0.5 pu: a) rotor currents and crowbar activation, b) synchronizing-point currents, c) synchronizing-point voltages.

The same fault is simulated with the crowbar resistance of 0.05 pu and the results are shown in Fig. 4.10. The slip reactive power curve is steeper compared to the previous case, which causes even higher reactive power absorption from the network. The post-fault steady state currents reaches almost 6 kA RMS (4.2 pu) as can be seen from Fig. 4.10b. The voltage recovery, shown in Fig. 4.10c, is delayed more than 3 seconds and the voltage magnitude decreases to 0.37 kV (0.54 pu). This kind of behavior of the wind turbines cannot be tolerated. Although the voltage stability is maintained even in this case, the connection of other induction generators or motors in the vicinity would decrease the voltage even more. This decreased voltage may lead to voltage collapse in the significant part of the nearby power system if the induction machines are not tripped.

The reason for the fast voltage recovery in simulations, shown in Investigation 4, is the utilization of the different crowbar resistances during the fault and voltage recovery. When the increased crowbar resistance is used, the absorbed reactive power remains low and the impact of the increased slip decreases. The increased crowbar resistance increases the rotor voltages during the crowbar connection. Therefore, the resistance should be selected so that the rotor voltages during the voltage recovery do not damage the isolation of the rotor windings. Also, the resistance value should be kept low enough to prevent the rotor voltages to increase over the DC-link voltage of the converter in order to prevent the

damaging of the DC-link capacitor due to an overvoltage. However, the capacitor damage due to the overvoltage can be prevented also by using the braking chopper in the DC-link.

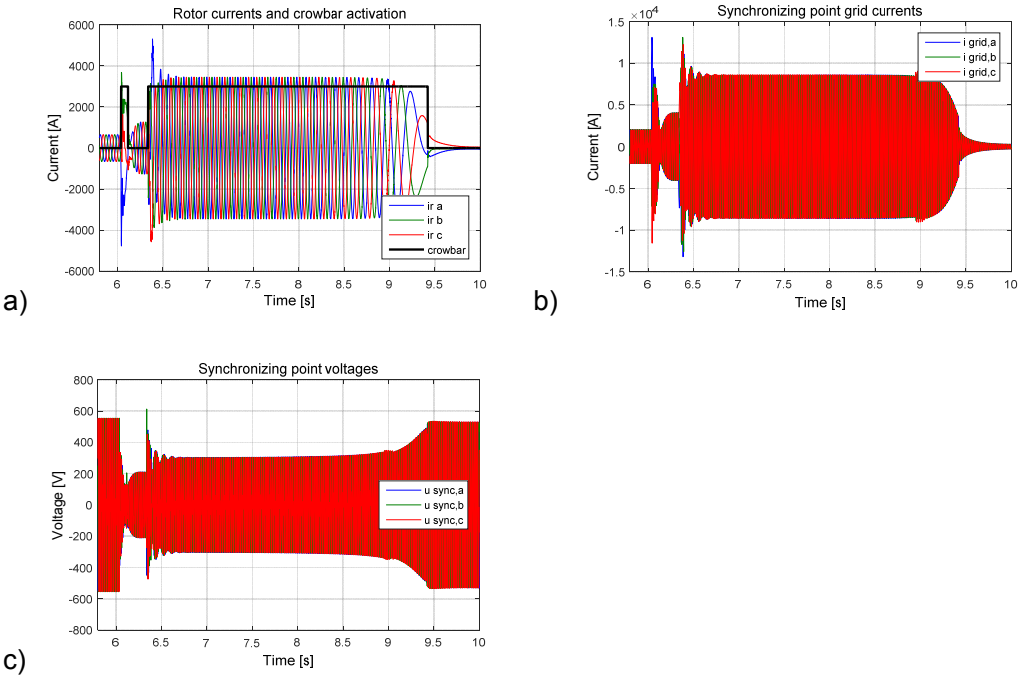

Fig. 4.10. DFIG during three-phase fault with R_{crow} = 0.05 pu: a) rotor currents and crowbar activation, b) synchronizing-point currents, c) synchronizing-point voltages.

4.5.2 Conclusion of Investigation 5

In Investigation 5, the impact of the active crowbar structure and the crowbar resistance on the operation of the DFIG wind turbine during the voltage recovery is analyzed. It is shown that the voltage recovery may be delayed, if small crowbar resistance, found in literature, is selected. This cannot be tolerated, because the delayed voltage recovery may escalate to a voltage collapse in a significant part of the power system, especially, if there are nearby located induction motor loads. This is the reason, why it is emphasized in [107] that the crowbar activation during the voltage recovery must be prevented. However, it was shown in Investigation 4, that the crowbar activation during the voltage recovery can be allowed without a delayed voltage recovery, if the modified crowbar structure is used. The modified crowbar structure utilizes different resistances during the fault and voltage recovery. The resistance during the voltage recovery should be selected as high as possible in order to minimize the reactive power consumption of the generator.

5. Laboratory test environment for wind turbine prototype

In this chapter, the RTDS/dSPACE-environment is extended to a PHIL-environment, where FPC-based GE is controlled by RTDS and small-scale laboratory prototype of wind turbine is controlled by using dSPACE. The target is to analyze the performance of the inexpensive commercial voltage source converter, which is configured to operate as GE.

The PHIL environment is described in Section 5.1 and the control system options of GE are depicted in Section 5.2, respectively. Closed-loop control systems are tuned by using the gain and phase margin measurements in Section 5.3. The performance of GE is analyzed by using frequency domain measurements in Section 5.4, and time domain measurements in Section 5.5. The future work related to the environment is discussed in Section 5.6.

5.1 Experimental test setup

A block diagram of the PHIL laboratory test environment for the wind-turbine prototype is shown in Fig. 5.1. A DC motor is used to emulate the operation of the wind turbine rotor by producing mechanical torque to rotor shaft. The operation of the DC motor is controlled by using a thyristor rectifier. Torque reference for the rectifier is obtained from the aerodynamic wind turbine model, which is simulated by dSPACE. The torque reference is computed on the basis of wind velocity and the measured rotational frequency of the rotor shaft.

PMSG is used as a wind turbine generator. The operation of the generator is controlled by using a three-level three-wire rectifier based on IGBT switches. The simplified speed control system shown in Fig. 2.3a instead of torque control system, which is standard in industrial applications, is implemented in Simulink and executed by dSPACE. The aim of the control system is to optimize the tip speed ratio in order to maximize the power generation under different wind conditions. Wind turbine NSC is a three-level four-wire IGBT-based converter, which controls the DC-link voltage to 750 V. NSC control system is synchronized by using phase-locked loop method presented in 2.3.1. Both GSC and NSC are sized to 10 kVA. The hardware arrangement and parameters of the laboratory test setup are presented in Appendix F.

The power network model, shown in Fig. F.2, is simulated by RTDS. PCC currents are measured and transferred into RTDS simulation. Hence, the wind turbine is modeled as a current source in the RTDS model. GE generates the reference voltages $\underline{u}^{*}_{\mathrm{PCC}}$, which are obtained from RTDS simulation, to PCC of the prototype. The GE control system is implemented by using second dSPACE, which generates the duty cycles for the GE converter. The GE hardware consists of the converter, LC-filter and 400/400V isolation transformer. An active emulator NSC transfers the power generated by the wind turbine prototype back to the network.

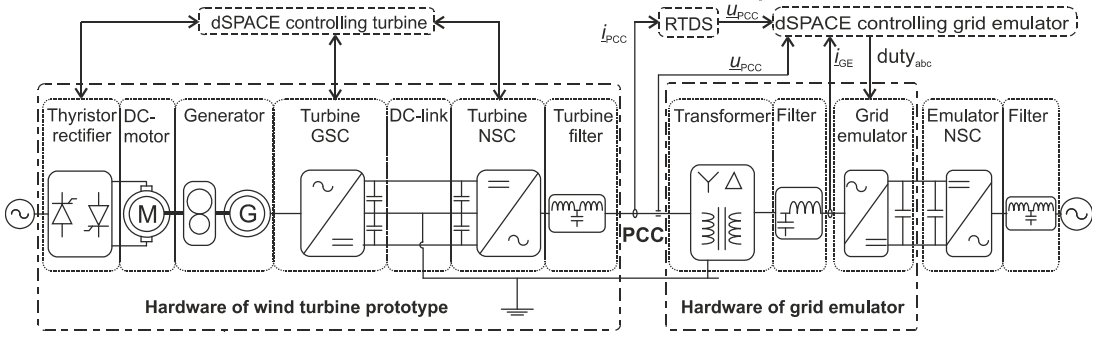

Fig. 5.1. Block diagram of the laboratory test setup.

5.2 Control system of grid emulator

A comparison of an open-loop control, closed-loop voltage control (V-control) and closed-loop-cascaded voltage and current control (VC-control) of GE is carried out in this thesis. This section presents the control systems.

The block diagram of the implementation of the open-loop-controlled GE is shown in Fig. 5.2. The measured PCC currents are transferred into RTDS Giga-Transceiver Analogue Input card (GTAI) [130], low-pass filtered (LPF) and scaled. The LPF cut-off frequency is selected to be 700 Hz. The currents are scaled so that the 10 kVA prototype represents 500 kVA wind turbine in the RTDS simulation. The Giga-Transceiver Analogue Output card (GTAO) [130] outputs are the PCC voltages, which are sent into dSPACE analog inputs. In the dSPACE model implemented in Simulink, the measured voltages are scaled so that the nominal line-to-line voltage of PCC is 690 $V_{\mathrm{l-l}}$. However, the nominal PCC voltage in the laboratory setup is 329 $V_{\mathrm{l-l}}$. The scaled voltages $u^{*}_{\mathrm{PCC,abc}}$ are Park transformed in order to express the voltages in dq-axis components $u^{*}_{\mathrm{PCC,dq}}$. The synchronous reference frame is oriented to the positive sequence component of the

RTDS-simulated reference voltage and the angle of the reference frame is provided by DSOGI-FLL. In the open-loop mode, $u^*_{GE,dq}$ correspond to the RTDS reference voltages and the inverse Park transformation is used to obtain the GE voltage references $u^*_{GE,abc}$. The aim of the feed forward term $\Delta\theta$ is to take into account the phase shift caused by the delta/star transformer of GE. Space-vector pulse width modulation (SWPWM) [123] is used to generate the duty cycles duty_{abc} for GE, which are fed from dSPACE into GE hardware via optical signals.

The control system block diagram of V-controlled GE is shown in Fig. 5.3. The PCC voltages $u_{PCC,abc}$ are measured and low pass filtered with the cut-off frequency of 700 Hz. Because the control system is implemented in the synchronous reference frame, the measured voltages are Park transformed. The GE reference voltages $u^*_{GE,abc}$ are provided by the voltage control PI-controllers.

The control system block diagram of VC-controlled GE is shown in Fig. 5.4. The control system contains fast inner loop for GE current control and slower outer loop for PCC voltage control. The measured currents are low pass filtered with the cut-off frequency of 700 Hz.

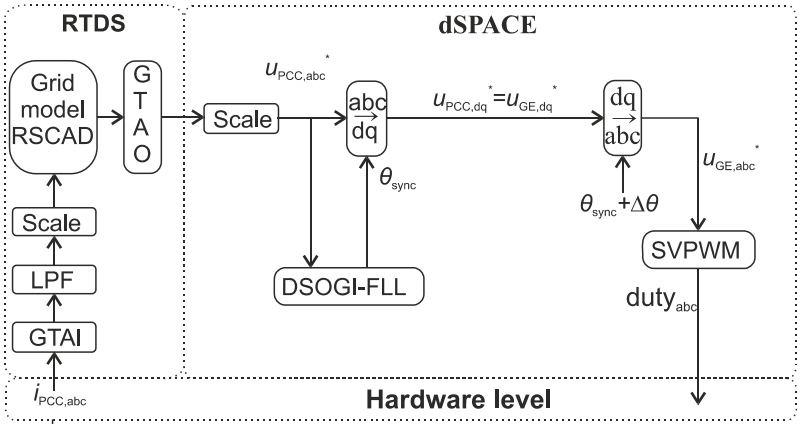

Fig. 5.2. Control system block diagram of open-loop-controlled GE.

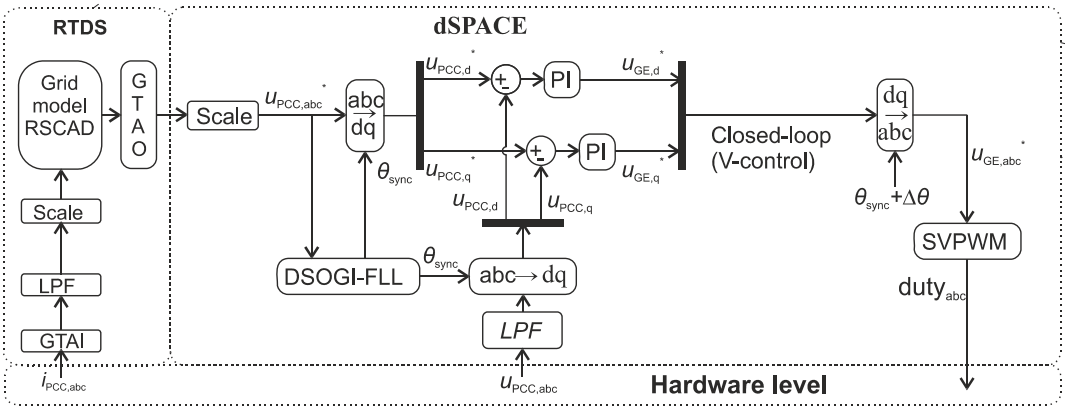

Fig. 5.3. Control system block diagram of voltage-controlled GE.

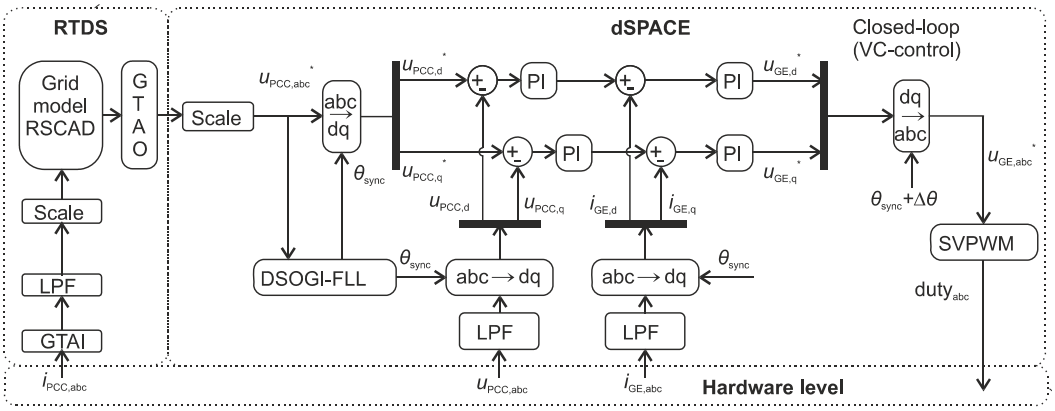

Fig. 5.4. Control system block diagram of voltage-current-controlled GE.

5.3 Controller tuning

The GE controllers are tuned by utilizing frequency response measurements. The measurements are carried out by using frequency analyzer by Venable Instruments. The measurement arrangement is depicted in Fig. 5.5. Variable frequency injections are added to the control reference, which are fed back to the frequency analyzer with the measured voltage. The analyzer calculates the gain and phase at the injection frequencies.

In Sections 5.3.1 and 5.3.2, the closed-loop transfer functions $u_\mathrm{d}/u_\mathrm{d}^*$ as well as $u_\mathrm{q}/u_\mathrm{q}^*$ are measured. The injection is added only to the d-component control reference and the q-channel injection voltage $u_{\mathrm{inj,q}}$ is set to zero, when the transfer function $u_\mathrm{d}/u_\mathrm{d}^*$ is measured. On the contrary, the injection is added only to the q-component reference in

the measurement of u_q / u_q^*. The open-loop transfer functions are calculated from the measured closed-loop transfer function in order to measure the gain margin (GM) and phase margin (PM). The PI-controller is tuned utilizing GM and PM.

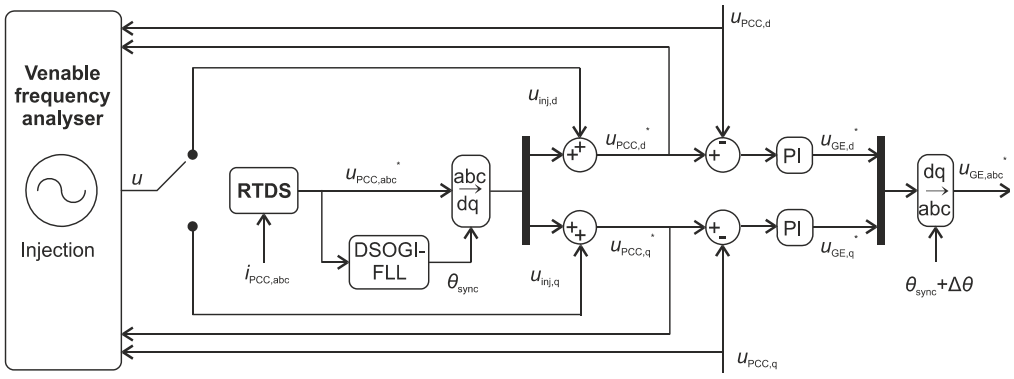

Fig. 5.5. Frequency response measurement with injection to dq-references.

5.3.1 Wind turbine connected to RTDS grid

The wind speed was set to nominal value 12 m/s during the measurements. When GE is operating in the voltage-control mode, the measured open and closed-loop transfer functions for d- and q-components are shown in Figs. 5.6a and b, respectively. The transfer functions in the voltage and current control mode are shown in Figs. 5.7a and b. The measured gain and phase margins as well as controller tuning parameters are given in Table 5.1.

Table 5.1. Measured GM, PM and controller tuning parameters.

	Control mode			
	Voltage control		Voltage – current control	
	d-channel	q-channel	d-channel	q-channel
Gain margin	7.63 dB (at 792Hz)	9.34 dB (at 800Hz)	6.49 dB (at 795Hz)	7.79 dB (at 800Hz)
Phase margin	101° (at 111Hz)	100° (at 107Hz)	82.2° (at 129Hz)	82.3° (at 127Hz)
	Voltage controller		Voltage controller	Current controller
Proportional gain	k = 0.32		k = 0.2	k = 1.8
Integrator time	T_i = 0.0006		T_i = 0.0038	T_i = 0.0006

According to [126], the reasonable values for GM and PM are 2-5 (= 2-6 in dBs) and 30-60°, respectively. Based on the measured GM and PM, it can be concluded that the GE performance cannot be significantly improved by choosing different parameters in PI-controllers without endangering the stability of the system.

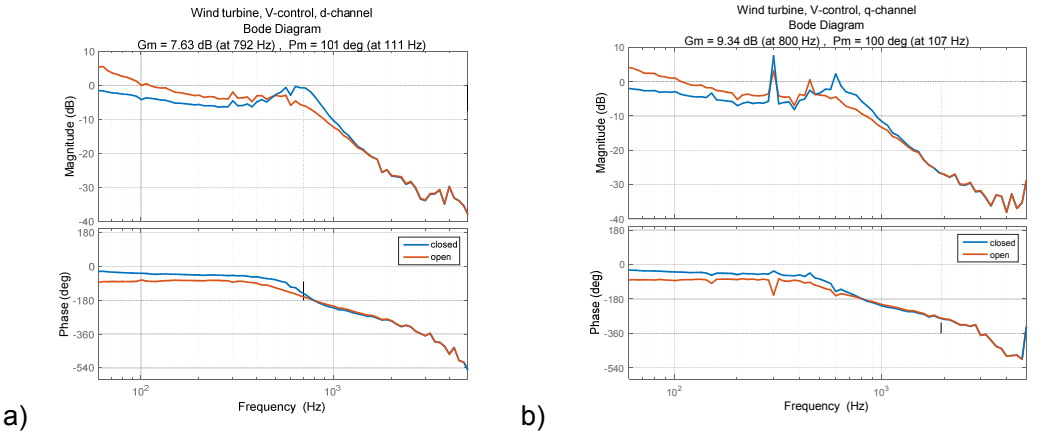

a) b)

Fig. 5.6. Measured frequency response when prototype is connected to V-controlled GE.

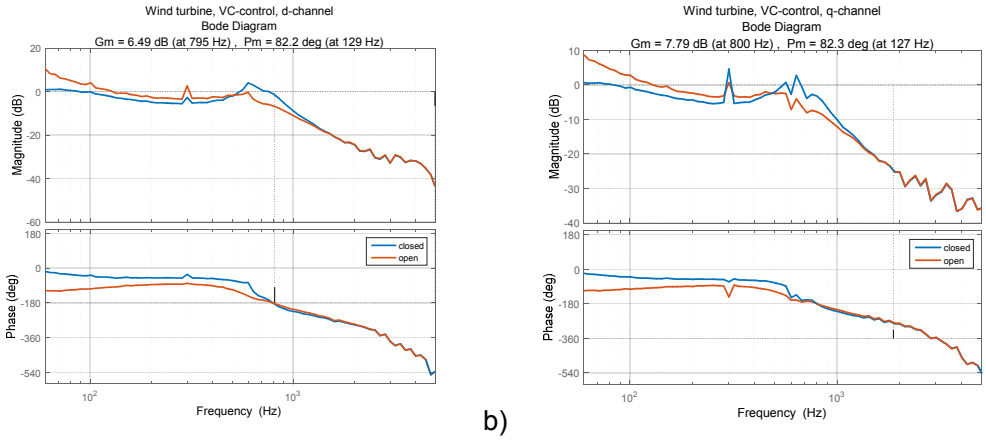

a) b)

Fig. 5.7. Measured frequency response, when prototype is connected to VC-controlled GE.

5.3.2 Resistive load connected to RTDS grid

In frequency response measurements shown in Figs. 5.8 and 5.9, the wind turbine prototype is replaced by the resistive load. The controller parameters are kept the same. Voltage-controlled GE transfer functions u_d / u_d^* as well as u_q / u_q^* are shown in Fig. 5.8. The transfer functions of voltage-current controlled GE are shown in Fig. 5.9. The measured voltage control gain and phase margins are given in Table 5.2.

Table 5.2. Measured GMs and PMs, when GE supplies resistive load.

	Control mode			
	Voltage control		Voltage – current control	
	d-channel	q-channel	d-channel	q-channel
Gain margin	9.57 dB (at 1080Hz)	11.9 dB (at 1100Hz)	8.09 dB (at 1050Hz)	10.5 dB (at 1070Hz)
Phase margin	101° (at 106Hz)	103° (at 103Hz)	85.9° (at 133Hz)	83.5° (at 126Hz)

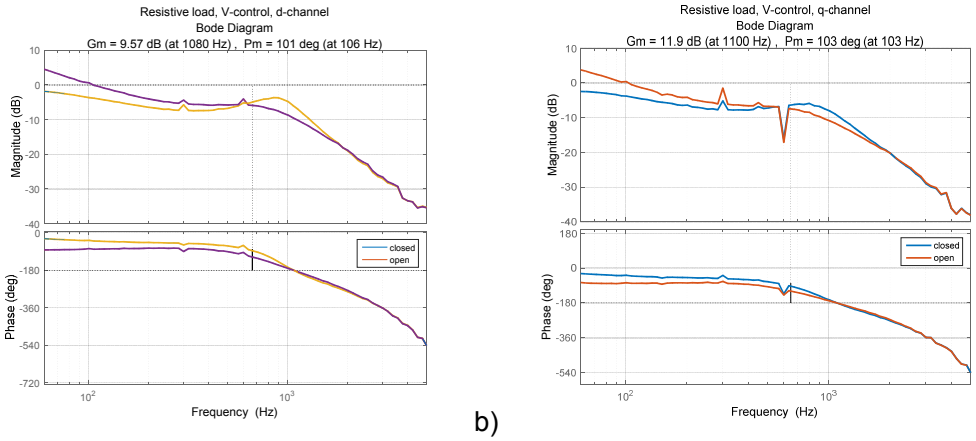

a) b)

Fig. 5.8. Measured frequency response, when resistive load is connected to V-controlled GE.

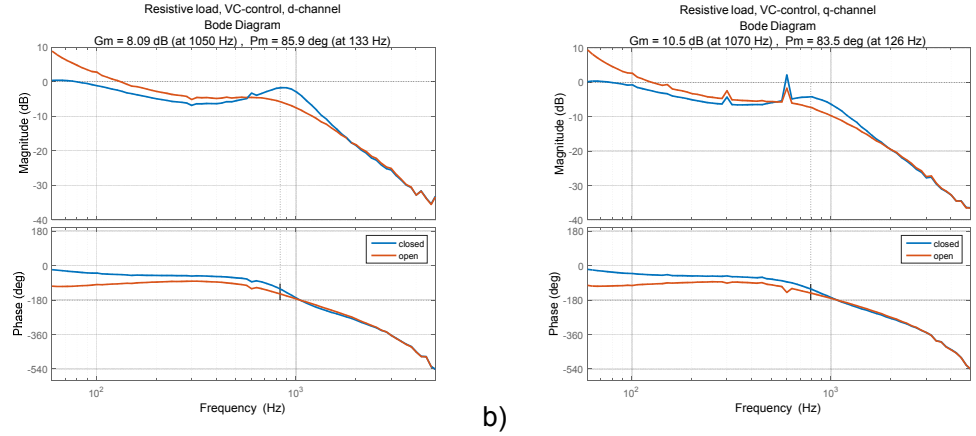

a) b)

Fig. 5.9. Measured frequency response, when resistive load is connected to VC-controlled GE.

It can be noticed that the change of the hardware under test from the prototype to resistive load increases GM although the controller parameters are kept the same. Thus, it can be concluded that the tuning of the GE controllers is dependent also on the hardware, which is connected to GE. Hence, it is not possible to have optimally tuned GE with fixed controller parameters independent on the connected hardware.

5.4 Investigation 6: Performance of GE in frequency domain

The performance of GE is analyzed in frequency domain in this investigation. The correct frequency response measurement of positive and negative sequence voltage components requires special measurement arrangement, which is analyzed in this investigation. Finally, the frequency responses of the sequence components are measured in cases, where GE supplies resistive load as well as wind turbine prototype.

5.4.1 Sequence components in synchronous reference frame

The operation of the power system is typically analyzed utilizing positive, negative and zero-sequence components. In this thesis, the performance of GE is assessed based on how well GE can generate the sequence components in different frequencies. Therefore, the frequency responses of the positive and negative sequence components are measured. The aim of this section is to reveal, how the sequence components appear in the synchronous reference frame oriented to the positive sequence voltage component. In addition, the frequency responses shown in Section 5.3, which are correctly measured to obtain the GM and PM values, are analyzed from the sequence components point of view.

Three-phase voltage vector $\underline{u}_{\mathrm{abc}}$, when positive or negative sequence n^{th}-order component $\underline{u}^{\mathrm{n}}$ is superimposed to the positive sequence voltage vector $\underline{u}^{+1}$ at the fundamental frequency, can be expressed as [33]

$$\underline{u}_{\mathrm{abc}} = \underline{u}^{+1}_{\mathrm{abc}} + \underline{u}^{\mathrm{n}}_{\mathrm{abc}} = \hat{u}^{+1}\begin{bmatrix} \cos(\omega t) \\ \cos\left(\omega t - \frac{2\pi}{3}\right) \\ \cos\left(\omega t + \frac{2\pi}{3}\right) \end{bmatrix} + \hat{u}^{\mathrm{n}}\begin{bmatrix} \cos(n\omega t) \\ \cos\left(n\omega t - \frac{2\pi}{3}\right) \\ \cos\left(n\omega t + \frac{2\pi}{3}\right) \end{bmatrix}, \tag{5.1}$$

where $\hat{u}$ denotes peak value of the phase voltage, n > 0 indicates the positive sequence component and n < 0 indicates the negative sequence component. The three-phase voltage vector can be expressed in stationary reference frame by

$$\underline{u}_{\alpha\beta} = \begin{bmatrix} u_\alpha \\ u_\beta \end{bmatrix} = [T_{\alpha\beta}]\underline{u}_{\mathrm{abc}} = \hat{u}^{+1}\begin{bmatrix} \cos(\omega t) \\ \sin(\omega t) \end{bmatrix} + \hat{u}^{\mathrm{n}}\begin{bmatrix} \cos(n\omega t) \\ \sin(n\omega t) \end{bmatrix}. \tag{5.2}$$

The voltage vector in the stationary reference frame can be transformed into the synchronous reference frame by

$$\underline{u}_{\mathrm{dq}} = \begin{bmatrix} u_{\mathrm{d}} \\ u_{\mathrm{q}} \end{bmatrix} = [T_{\mathrm{dq}}]\underline{u}_{\alpha\beta} = \hat{u}^{+1}\begin{bmatrix} \cos(\omega t - \theta') \\ \sin(\omega t - \theta') \end{bmatrix} + \hat{u}^{\mathrm{n}}\begin{bmatrix} \cos(n\omega t - \theta') \\ \sin(n\omega t - \theta') \end{bmatrix}. \tag{5.3}$$

The control systems of GE are oriented to the positive sequence component of the network voltage. Thus, the d-axis voltage component represents the magnitude of the positive sequence voltage and $\omega t = \theta'$. Hence, Eq. (5.3) can be given by

$$\underline{u}_{\mathrm{dq}} = \begin{bmatrix} u_{\mathrm{d}} \\ u_{\mathrm{q}} \end{bmatrix} = [T_{\mathrm{dq}}]\underline{u}_{\alpha\beta} = \hat{u}^{+1}\begin{bmatrix} 1 \\ 0 \end{bmatrix} + \hat{u}^{\mathrm{n}}\begin{bmatrix} \cos((n-1)\omega t) \\ \sin((n-1)\omega t) \end{bmatrix}. \tag{5.4}$$

Identities for the negative angles for sine and cosine can be given by

$$\begin{aligned} \sin(-x) &= -\sin(x) \\ \cos(-x) &= \cos(x) \end{aligned}. \tag{5.5}$$

Following observations can be made based on (5.4) and (5.5)

- Positive or negative sequence n^{th}-order component ($n \neq 1$) generates oscillating component to both d- and q-channel voltage components
- The frequency of oscillating component is $(n-1)\omega$
- The d-axis component leads q-axis component with 90 degrees if $(n - 1) > 0$
- The q-axis component leads d-axis component with 90 degrees if $(n - 1) < 0$

In the closed-loop frequency responses in Figs. 5.6 - 5.9, the injection voltage is set either to d- or q-axis and the other axis injection voltage is set to zero. The frequency responses do not represent the frequency responses of the sequence components, because the oscillations should appear in both d- and q-axis components according to (5.4). In the following, the frequency responses in Figs. 5.6 - 5.9 are analyzed with the help of an illustrative example.

Eq. (5.4) can be expressed as follows, if n is set to 3

$$\begin{bmatrix} u_{\mathrm{d}} \\ u_{\mathrm{q}} \end{bmatrix} = \hat{u}^{+1}\begin{bmatrix} 1 \\ 0 \end{bmatrix} + \hat{u}^{3}\begin{bmatrix} \cos((3-1)\omega t) \\ \sin((3-1)\omega t) \end{bmatrix} = \hat{u}^{+1}\begin{bmatrix} 1 \\ 0 \end{bmatrix} + \hat{u}^{3}\begin{bmatrix} \cos(2\omega t) \\ \sin(2\omega t) \end{bmatrix}. \tag{5.6}$$

In order to remove the oscillating part from the voltage q-axis component the fundamental-frequency negative-sequence component needs to be added to (5.6). Thus,

$$\begin{bmatrix} u_d \\ u_q \end{bmatrix} = \hat{u}^{+1}\begin{bmatrix} 1 \\ 0 \end{bmatrix} + \hat{u}^{3}\begin{bmatrix} \cos((3-1)\omega t) \\ \sin((3-1)\omega t) \end{bmatrix} + \hat{u}^{-1}\begin{bmatrix} \cos((-1-1)\omega t) \\ \sin((-1-1)\omega t) \end{bmatrix} \\ = \hat{u}^{+1}\begin{bmatrix} 1 \\ 0 \end{bmatrix} + \hat{u}^{3}\begin{bmatrix} \cos(2\omega t) \\ \sin(2\omega t) \end{bmatrix} + \hat{u}^{-1}\begin{bmatrix} \cos(-2\omega t) \\ \sin(-2\omega t) \end{bmatrix} \quad (5.7)$$

If $\hat{u}^{3} = \hat{u}^{-1}$ and taking (5.5) into account, the following is obtained

$$\begin{bmatrix} u_d \\ u_q \end{bmatrix} = \hat{u}^{+1}\begin{bmatrix} 1 \\ 0 \end{bmatrix} + \hat{u}^{3}\begin{bmatrix} \cos(2\omega t) \\ \sin(2\omega t) \end{bmatrix} + \hat{u}^{-1}\begin{bmatrix} \cos(-2\omega t) \\ \sin(-2\omega t) \end{bmatrix} \\ = \hat{u}^{+1}\begin{bmatrix} 1 \\ 0 \end{bmatrix} + \hat{u}^{3}\begin{bmatrix} \cos(2\omega t) \\ \sin(2\omega t) \end{bmatrix} + \hat{u}^{3}\begin{bmatrix} \cos(2\omega t) \\ -\sin(2\omega t) \end{bmatrix} = \hat{u}^{+1}\begin{bmatrix} 1 \\ 0 \end{bmatrix} + 2\hat{u}^{3}\begin{bmatrix} \cos(2\omega t) \\ 0 \end{bmatrix} \quad (5.8)$$

Eq. (5.8) represents the frequency response measurements shown in Figs. 5.6a - 5.9a at a point, where d-axis injection voltage frequency is 100 Hz (n = 2). In this situation, the symmetrical components rotating with 150 Hz and -50 Hz can be measured from the three-phase voltages. The magnitudes of both of the voltages are half the injection voltage.

Based on the discussion above, it can be concluded that the closed-loop frequency responses presented in Section 5.3 cannot be used to evaluate the GE performance to generate sequence components at different frequencies. Because the target in this study is to measure the frequency responses of the positive and negative sequence components, a new measurement method needs to be invented. One alternative is to generate 90 and -90 degrees phase shifter to injection voltages as indicated by (5.4). However, the injection added to the voltage control reference does not generate AC voltage components at the injection frequency, because the synchronous reference frame is rotating with fundamental frequency. Other alternative is to generate three-phase injection voltages from the injection voltage of the frequency analyzer. In this thesis, the latter method is used and analyzed in Section 5.4.2.

5.4.2 Measurement of sequence component frequency response

The measurement arrangement of the positive-sequence frequency response is shown in Fig. 5.10. The injection voltage from the frequency analyzer is fed to SOGI-FLL, which is implemented in dSPACE. The purpose of SOGI-FLL is to measure the rotational frequency $\omega_{inj}^{'}$ of the injection voltage. The injection angle $\theta_{inj}^{'}$ is obtained after integration of the frequency. $\theta_{inj}^{'}$ is fed to inverse Park transformation. The peak value of the injection voltage is used as d-axis input and zero is fed to q-axis input of the transformation. The outputs of the inverse Park transformation are symmetrical three-phase voltages at the

injection frequency. The control reference of the phase voltage $u^{*}_{PCC,CTRL,a}$ and measured phase voltage $u_{PCC,a}$ are fed to the frequency analyzer, which calculates the positive sequence frequency response.

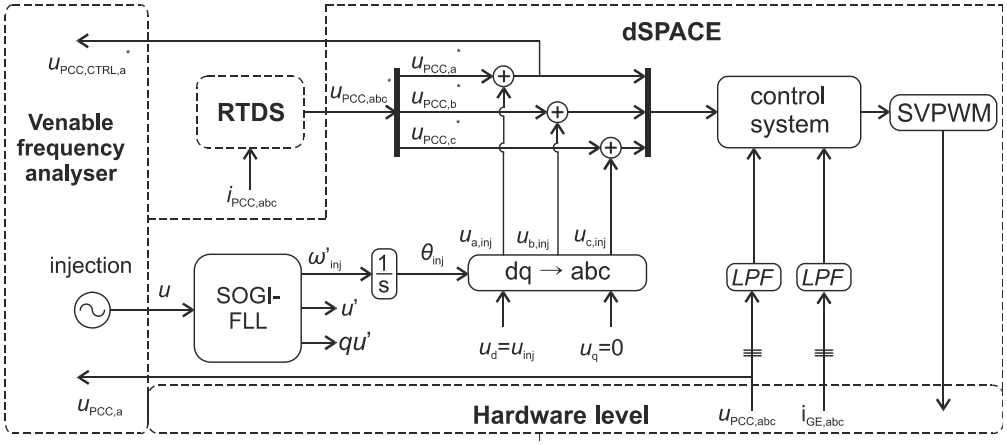

Fig. 5.10. Positive sequence frequency response measurement.

The measurement arrangement of the negative-sequence frequency response is shown in Fig. 5.11. Again, the outputs of the inverse Park transformation are the positive-sequence three-phase voltages. However, the injection voltage $u_{b,inj}$ is added to the control reference of the c-phase voltage $u^{*}_{PCC,c}$ and $u_{c,inj}$ is added to the control reference of the b-phase voltage $u^{*}_{PCC,b}$. The reference and measured values are fed to the frequency analyzer, which calculates the negative sequence frequency response.

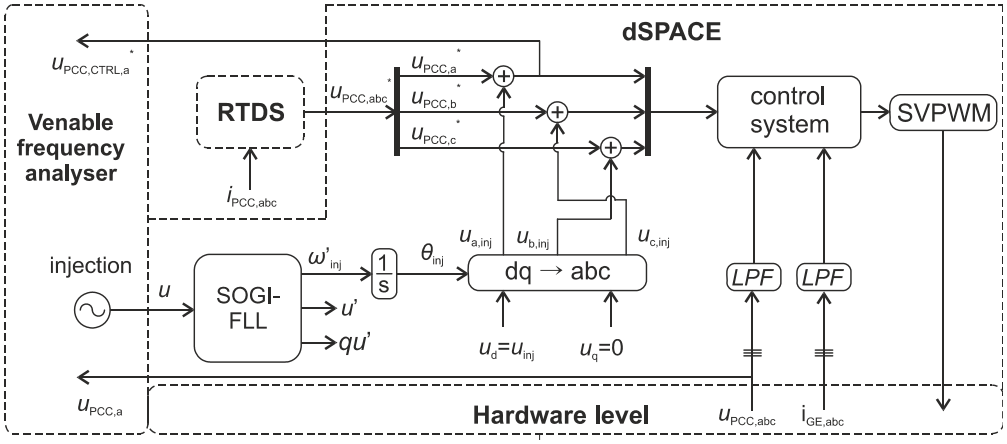

Fig. 5.11. Negative sequence frequency response measurement.

5.4.3 Performance of grid emulator

The system response for the positive and negative sequence voltage components within the frequency range of 10 Hz – 1300 Hz are measured in order to assess the performance of GE. The frequency responses are measured in cases, where GE supplies resistive load and wind turbine prototype. This way the impact of the hardware connected to GE can be analyzed. The frequency response measurements are carried out, when GE is open-loop-controlled, closed-loop V-controlled and closed-loop VC-controlled.

5.4.3.1 Resistive load connected to RTDS grid

The RTDS-controlled GE is set to supply resistive load. The measured open-loop-controlled, closed-loop V-controlled and closed-loop VC-controlled frequency responses are shown in Figs. 5.12a, b and c, respectively. The controller parameters defined in Section 5.3 are used. The critical frequencies from the viewpoint of GE performance are the positive and negative sequence 50 Hz. If the gain and phase are zero at positive sequence 50 Hz, GE can generate symmetrical fundamental frequency reference voltages perfectly. The network voltage asymmetry can be accurately represented, if the gain and phase are zero at negative sequence 50 Hz frequency.

In Fig. 5.12a, both the positive and negative sequence gains are approximately -0.5 dB at 50 Hz point. Hence, the peak value of the measured positive sequence voltage is about 15 V smaller than the peak value of the corresponding reference voltage. The positive and negative sequence gain remain close to 0 dB up to 300 Hz. The positive and negative sequence phase is close to zero up to 100 Hz after which the phase starts to decrease. The peak value of gain is 3.5 dB appearing at around 1 kHz.

The measured positive sequence gain of V-controlled GE, shown in Fig. 5.12b, is 0.035 dB at 50 Hz. Due to the closed-loop control of the voltages, the measured voltages correspond to the reference values accurately without noteworthy gain error. The measured phase at 50 Hz is 5°, which appears due to the low pass filters of the measurements. The negative-sequence gain and phase jump to zero near 50 Hz. This is an incorrect measurement result, which reveals the weakness of the used frequency response measurement arrangement. In this case, the frequency analyzer injects 50 Hz component, which is transformed into the negative-sequence injection by the measurement system. The analyzer measures the gain and phase at the injection frequency, which is 50 Hz. Due to the fact that the positive sequence voltage at 50 Hz is much greater (peak value at around 270 V) than the negative-sequence injection voltage (peak value 6 V), the gain and phase correspond to the positive-sequence measurement at 50 Hz. However, the correct gain and phase can be estimated from the values before

and after the 50 Hz point. Hence, it can be assumed that the gain and phase are approximately -2.5 dB and -37°, respectively. It can be seen from the frequency response that as the frequency increase the gain and phase decrease. However, like in the open-loop case, there is a notch, which appears in this case at the frequency around 900 Hz. The peak value of the notch is -4.5 dB.

The control-loop bandwidth is defined as the frequency, where the frequency response has declined 3 dB from 0 dB. [131] The bandwidth defined as above is not very useful measure of the accuracy of GE to generate the desired reference voltages. The frequency range, where the control system can generate the reference voltages without gain and phase errors, is a more relevant measure. However, the bandwidth gives indication on how fast the control system is able to generate the reference values during the voltage transients. In other words, the reference voltages after, for example, the symmetrical voltage dip can be executed faster as the bandwidth increases. The bandwidths of the positive and negative-sequence responses are approximately 165 Hz and 60 Hz, respectively.

The measured positive-sequence gain and phase of the VC-controlled GE, shown in Fig. 5.12c, are 0.035dB and 5°, respectively. As expected, the closed-loop control eliminates the steady state error from the positive sequence voltage at 50 Hz. The negative-sequence gain and phase are approximately -2 dB and -45°, respectively. The measured control system bandwidths for the positive and negative-sequence voltage controls are 220 Hz and 90 Hz, respectively. Again, there is a clear notch at around 900 Hz, where the peak value for the gain is -2 dB.

In Fig. 5.12d, the Bode diagram of the impedance of the GE passive components is shown. The components are a filter inductor and capacitor as well as an isolation transformer. The impedance has been calculated from the nameplate values of the components. It can be seen from Fig. 5.12d that there should be parallel resonance at 1060 Hz. However, there is a ±15%-tolerance in the filter inductance according to the nameplate. Thus, the resonant frequency may also appear at 986 Hz in theory. The notch at open-loop frequency response is caused by the resonance of the passive reactive elements. The peak of the notch in the closed-loop frequency response is shifted compared to the open-loop case due to the impact of the controllers.

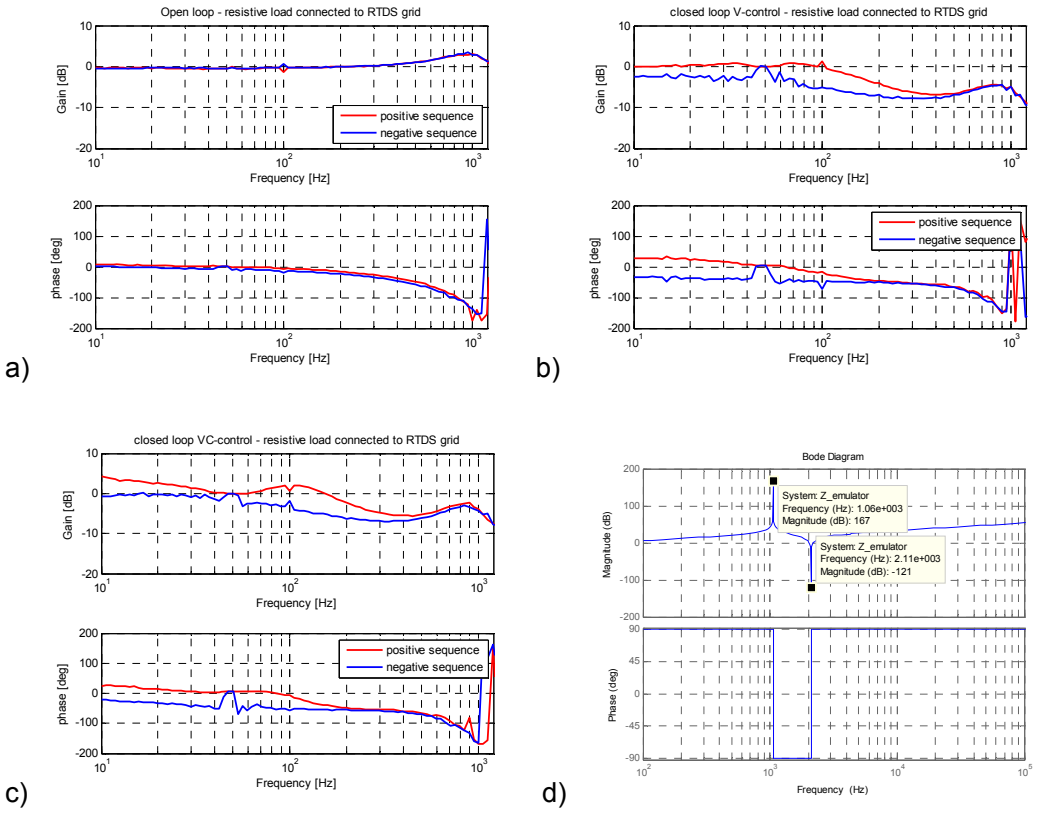

Fig. 5.12. Positive and negative sequence frequency response of GE connected to resistive load: a) open-loop mode, b) V-control mode, c) VC-control mode, d) Bode plot of GE impedance including isolation transformer.

5.4.3.2 Wind turbine connected to RTDS grid

The wind turbine prototype is connected to GE in the measurements of this section. The simulated wind speed is set to 12 m/s. The measured open-loop frequency response is shown in Fig. 5.13a. The positive and negative-sequence gains and phases are close to zero at low frequencies. It can be seen that the gains start to increase after the frequency of 150 Hz unlike in resistive load case, where the gain increases after 300 Hz. The positive sequence gain at 50 Hz point is 0.6 dB. This means that the peak value of the measured positive sequence voltage is around 20 V higher than the peak value of the reference voltages. The measured voltages are higher in this case due to the fact the direction of power and currents is reversed compared to the resistive load case. Therefore, the voltage drop over the impedance of the GE filter changes its polarity. The negative sequence gain and phase values at 50 Hz point are -0.7 dB and -11°, respectively. The highest gain in the open-loop response is 5 dB appearing approximately at 700 Hz, which is approximately 300 Hz lower frequency than the corresponding frequency in the resistive load case. The

peak-gain frequency corresponds to the resonance frequency of the wind turbine filter as visible in Fig. 5.13b.

The closed-loop V-control as well as VC-control frequency responses are shown in Figs. 5.13c and d, respectively. The positive and negative-sequence gain and phase values at 50 Hz by using V-control are 0.02 dB, 5°, -3 dB and -40°, respectively. The corresponding values for VC-control are 0.01 dB and 5°, 0 dB and -40°. The measured control system -3 dB bandwidths for the positive and negative-sequences are approximately 168 Hz and 50 Hz for V-controlled GE. The comparative VC-control bandwidths are approximately 220 Hz and 100 Hz. Like in the open-loop case, the peak gain appears at around 700 Hz. If the gain of the control system is increased, the gain at this frequency would increase significantly and, at some point, the control system would become unstable. Thus, the main limitation considering the control system gain comes from the resonance at 700 Hz, which was not existent in the case, where the resistive load was connected to GE.

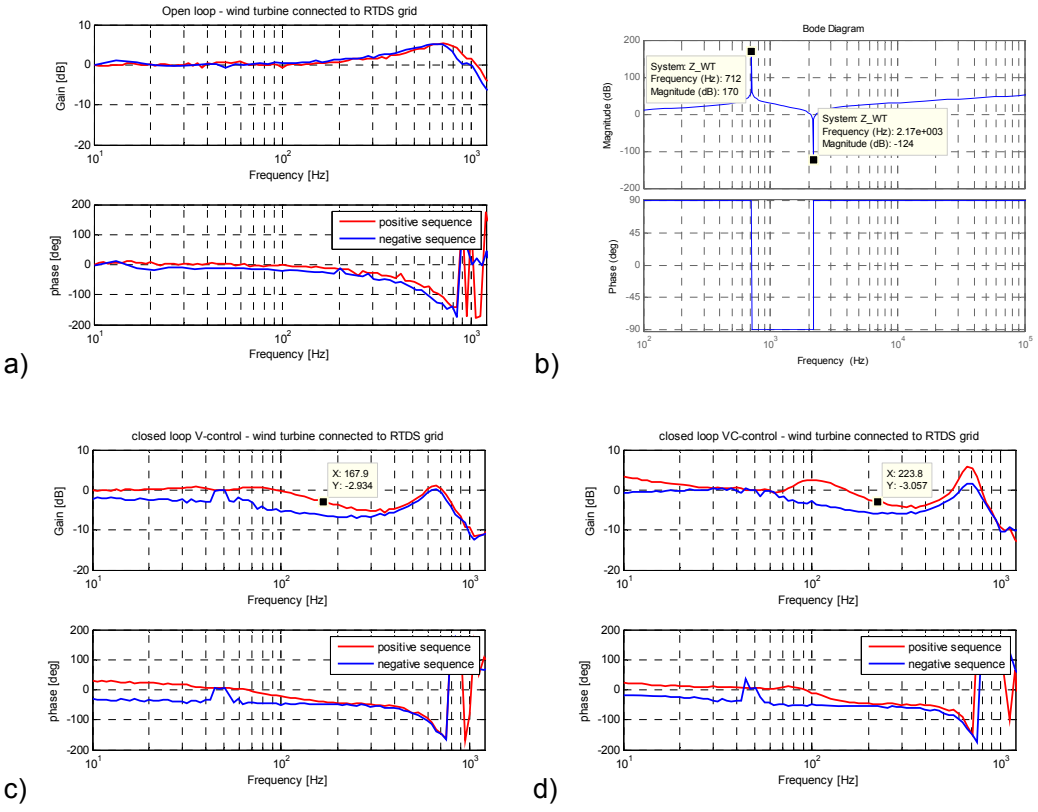

Fig. 5.13. Positive and negative sequence frequency response of GE, which supplies the wind turbine prototype: a) open-loop mode, b) Bode of plot wind turbine filter impedance, c) V-control mode, d) VC-control mode.

These measurements show that the bandwidth of the closed-loop control system is mainly limited by the resonances of the passive reactive components installed in the laboratory setup. In the case, when the wind turbine prototype is connected to GE, the bandwidth and performance of the GE control system is limited by the passive components of the wind turbine prototype. Thus, it can be concluded that the performance of GE is dependent on the hardware connected to GE in addition to design of the emulator itself.

5.4.4 Conclusion of investigation 6

In Investigation 6, the performance of GE is analyzed in frequency domain. The target is to measure the frequency response of the positive and negative sequence grid voltage components of GE. By this way, the performance of GE can be assessed. It is shown that the frequency response of the sequence components of the grid voltage cannot be measured simply by injecting voltage perturbations to the emulator voltage references, which is correct measurement method when GM and PM are measured, because the voltage controller operates in the rotating reference frame. An important contribution of this investigation is the detailed presentation of the arrangement to measure the frequency response of the sequence components.

The measurements of the sequence components are done in cases, where the resistive load and the wind turbine prototype is connected to GE. As the main contribution of these measurements, it is revealed that the bandwidth of the closed-loop control system of GE is mainly limited by the resonances created by the passive reactive components installed in the wind turbine prototype. Therefore, a generic conclusion is that the bandwidth may be limited due to the reactive components of the device connected to GE in addition to emulator design itself. This may not be recognized if GE performance is investigated only by using a pure resistive load as in [112]. In fact, the emulator may become unstable, if its control system is tuned using resistive load and then it is connected to supply other devices.

5.5 Investigation 7: Time domain experiments

In Investigation 7, GE is set to supply the wind turbine prototype and the performance of GE under symmetrical and unsymmetrical grid voltage dips is evaluated. The fault occurs in the RTDS simulated network shown in Appendix F. The wind speed is reduced from 12 m/s used in earlier experiments to 11 m/s in order to avoid the significant increment of DC-link voltage during the grid faults. The DC-link braking chopper is not implemented in the laboratory setup.

5.5.1 Symmetrical fault

The reference phase voltages from RTDS and measured voltages from PCC, when GE operates in the open-loop mode are shown in Fig. 5.14. The fault occurs at 1.503 s and lasts 100 ms. Due to the fact that the PCC voltages are not closed-loop controlled, the measured voltages are higher than the reference voltages even under steady-state operation. This is caused by the wind turbine generated currents, which create a voltage drop over the impedance of the GE filter. Thus, the error between the reference and measured voltages would increase if the wind speed increases. The decrement in the wind speed causes opposite effect. Hence, it can be concluded that the open-loop controlled GE cannot execute correct PCC voltages independent on the operation point of the wind turbine, which is determined by the output currents of the wind turbine. The result was also visible in the positive sequence frequency response measurement, shown in Investigation 6, where the gain and phase was not zero at 50 Hz.

The reference and measured voltages are shown in Fig. 5.15a, when GE is operating in the closed-loop V-control mode. Corresponding results by using the closed-loop VC-control mode are shown in Fig. 5.15b. The symmetrical fault lasts 100 ms in both cases and occurs at 1.62 s and 1.64 s under V-control and VC-control, respectively. It can be seen that the measured voltages correspond to the reference voltages accurately before and during the fault. In other words, the closed-loop control systems are able to generate the fundamental-frequency positive-sequence-voltage references accurately. This is expectable based on the frequency response results shown in Investigation 6. The high-frequency transients in the reference voltages after the fault cannot be realized by GE, because control system bandwidths are finite. However, it takes approximately 5 ms or less from the measured voltages to accurately reach the reference values in both cases. It can be concluded from the results shown in Figs. 5.15b and c that the PHIL environment with closed-loop-controlled GE is accurate enough for the symmetrical LVRT studies and tests for the wind turbine.

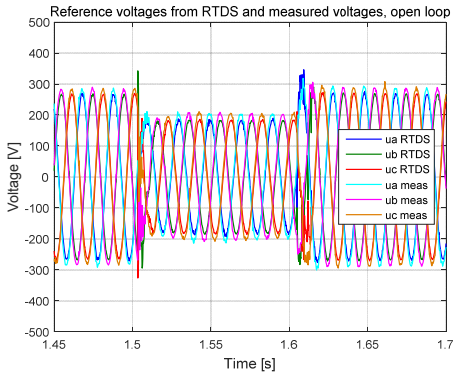

Fig. 5.14. Reference phase voltages from RTDS and measured voltages during symmetrical fault in RTDS network, when GE is open-loop controlled.

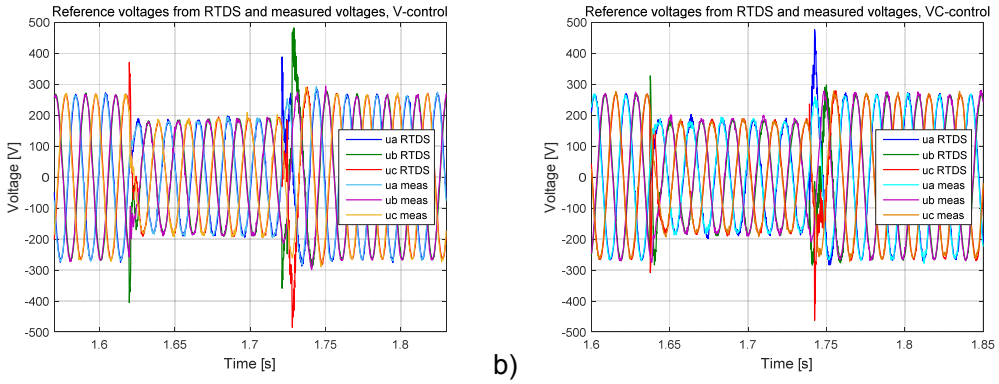

Fig. 5.15. Reference phase voltages from RTDS and measured voltages during symmetrical fault in RTDS network: a) closed-loop V-control, b) closed-loop VC-control.

5.5.2 Unsymmetrical fault

In this section, the operation of the PHIL test setup is investigated under the unsymmetrical grid fault. A single-phase-to-ground fault is propagated to two-phase voltage dip at PCC due to the delta/star transformer in the grid model. The RTDS reference voltages and measured voltages are shown in Fig. 5.16, when the GE is operating in the open-loop mode. The fault occurs at 1.47 s and lasts 100 ms.

The measured voltages are greater than the reference voltages during the fault. The reason is the uncontrolled positive-sequence 50 Hz voltage component. Therefore, GE cannot follow the positive-sequence-voltage reference given by RTDS, if current is flowing through the components of the laboratory setup. It should be noted also from Fig. 5.13a that the negative sequence gain and phase at 50 Hz are not zero. Although the gain and phase are close to zero, the impact of the non-zero values is visible also in time-domain

results. The difference between u_{aRTDS} and u_{ameas} voltages is smaller than the difference between u_{bRTDS} and u_{bmeas} due to the impact of the non-zero negative-sequence gain and phase at 50 Hz.

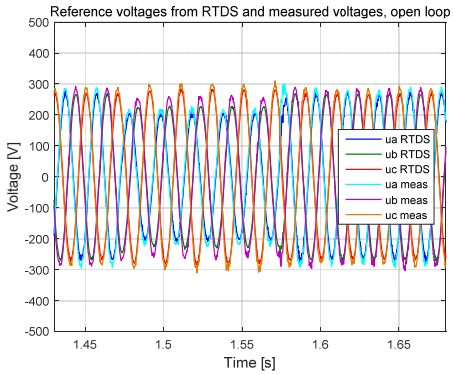

Fig. 5.16. Reference phase voltages from RTDS and measured voltages during unsymmetrical fault in RTDS network, when GE is open-loop controlled.

The reference and measured voltages are shown in Figs. 5.17a and b, when GE is operating in the closed-loop V-control and VC-control modes, respectively. The fault lasts 100 ms in both cases and occurs at 1.57 s and 1.595 s under V-control and VC-control, respectively.

It can be seen from Fig. 5.17a that u_{ameas} corresponds to u_{aRTDS} with very good accuracy during the fault. However, u_{bmeas} is clearly greater than its reference u_{bRTDS}, while u_{cmeas} is lower than u_{cRTDS}. Thus, the unbalanced PCC voltage references cannot be executed precisely although the positive-sequence reference voltages can be realized accurately. The reason is that V-controlled GE cannot generate perfectly the reference of the negative-sequence 50 Hz component as indicated by Fig. 5.13c.

Similar conclusion as above can be made also in the case, where GE is closed-loop VC-controlled. As shown in Fig. 5.13d, the positive and negative-sequence gains are 0 dB at 50 Hz, which means that no gain error exists. However, the unbalanced PCC voltages cannot be realized perfectly during the fault due to the non-zero phase of the negative sequence voltage component at 50 Hz.

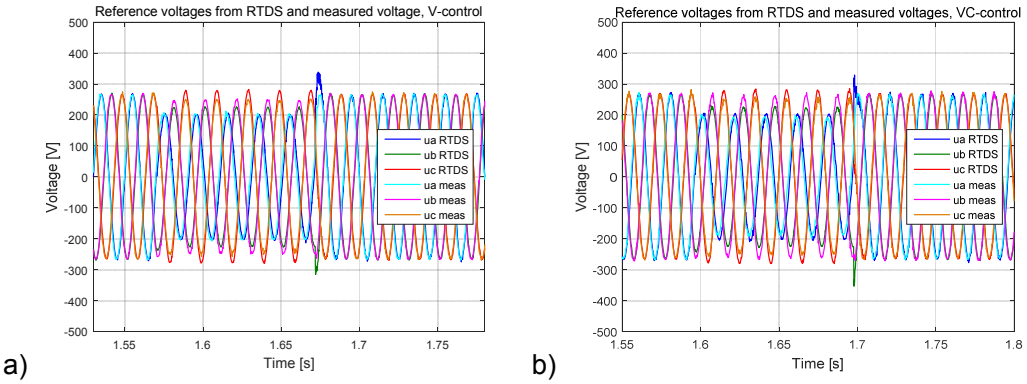

Fig. 5.17. Reference phase voltages from RTDS and measured voltages during asymmetrical fault in RTDS network: a) closed-loop V-control, b) closed-loop VC-control.

5.5.3 Performance improvement of grid emulator

It was shown in Investigation 6 that the control system bandwidth, and also the performance of GE, is limited by the resonance caused by the passive reactive components installed in the laboratory setup. More precisely, when the wind turbine prototype is connected to GE, the bandwidth is limited by the resonance caused by the filter components. According to mathematical calculation relying on the filter inductor and capacitor nameplate values, the resonance appears at 712 Hz. The frequency response measurements support this fact as well.

In order to improve the performance of GE, the reference voltages from RTDS has been fed through the notch filter tuned to 746 Hz. The Bode diagram of the notch filter (NF) is shown in Fig. 5.18a. The filter transfer function can be given as

$$\mathrm{NF(s)} = \frac{s^2 + 2.199 * 10^7}{s^2 + 4000s + 2.199 * 10^7}. \tag{5.9}$$

The purpose of NF is to prevent the controller impact at the resonant frequency. In other words, when the resonant-frequency voltage-reference components from RTDS are blocked, the control system cannot amplify the components at that frequency. As a result, the control system can be tuned to have a wider bandwidth.

The positive and negative sequence frequency responses of re-tuned V-controlled GE are shown in Fig. 5.18b. After the addition of NF, the control system proportional gain was increased from k=0.32 to k=0.57, while the integrator time was kept unchanged (T_i = 0.0006 s). The -3 dB bandwidth has increased significantly after the re-tuning of the voltage controller. The positive and negative-sequence bandwidths are approximately 700 Hz and

150 Hz, respectively. The negative-sequence gain is approximately -2 dB and the negative-sequence phase is approximately -30˚.

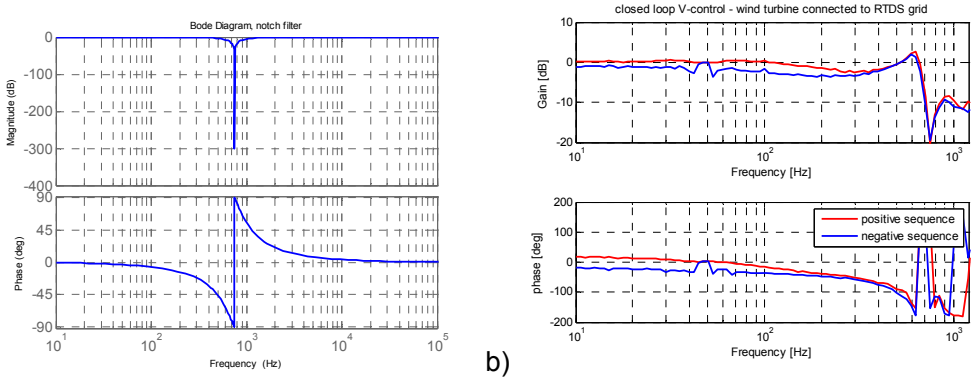

a) b)

Fig. 5.18. a) Bode diagram of NF, b) positive and negative-sequence frequency responses of re-tuned V-controlled GE.

The reference and measured voltages during the symmetrical fault is shown in Fig. 5.19a, when GE operates with re-tuned controller parameters. The voltage references are realized accurately after 3 ms from the beginning of the voltage dip. However, although the negative-sequence gain and phase have moved closer to 0 dB compared to the original tuning parameter case, the unbalanced voltages cannot be perfectly executed due to the non-zero gain and phase of the negative-sequence-voltage component at 50 Hz. However, it should be noticed according to Fig. 5.19b that the error between reference and measured voltages is smaller compared to the case, where the originally tuned controllers were used in Fig. 5.17a.

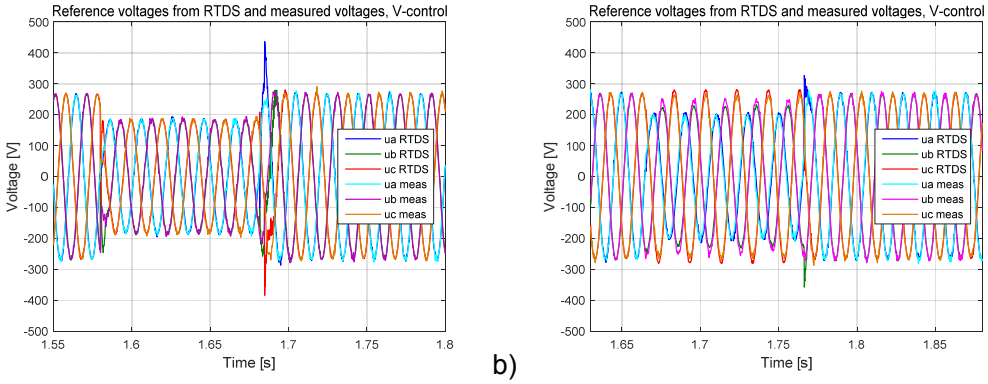

a) b)

Fig. 5.19. Reference phase voltages from RTDS and measured voltages with tuned V-controlled GE: a) symmetrical fault, b) unsymmetrical fault.

5.5.4 Conclusion of Investigation 7

In Investigation 7, the operation of open and closed-loop-controlled GE is studied under symmetrical and unsymmetrical grid faults. It is shown that closed-loop-controlled GE is able to generate the desired PCC voltages after symmetrical voltage dip in approximately 5 ms. This operation is clearly fast enough if the objective is to test the performance of wind turbine control system under the fault. For example, the defined fault clearance times of Scottish, German, Australia and Spain fault ride through requirements are 140 ms, 150 ms, 175 ms and 500 ms, respectively. [132] The drawback of open-loop-controlled GE is the lack of capability to execute the correct PCC positive-sequence voltages independent on the operation point of the wind turbine, which is normally determined by the wind conditions.

The unsymmetrical voltage dips are not generated accurately by GE. The reason is that the control system bandwidth is not wide enough to execute the negative-sequence 50 Hz component without the gain and phase errors. The root cause of the limited bandwidth is the resonance of the passive reactive elements interlinked to the laboratory setup. Notch filter can be used to reduce the impact of the resonance on the control bandwidth. However, the fundamental-frequency negative-sequence gain and phase errors were not totally eliminated.

Although the fundamental-frequency negative-sequence component cannot be perfectly generated with presented control method, the PHIL environment can be used to test the operation of the wind turbine control functionalities under asymmetrical network voltages. These functionalities can be for example a PCC voltage balancing or a positive-sequence reactive current injection.

5.6 Future work related to laboratory test setup

In order to improve the performance of GE in the future, the following aspects may be worth of considering.

- As shown in Section 5.5.3, the impact of reactive-component resonance on the control system can be decreased by using an additional notch filter in the control system. In the scope of this study, the second order notch filter was used. However, it may be possible to improve the GE tuning if higher order notch filter is used.
- The reactive components used in the PHIL test setup were not optimized specifically for this study. Based on the experience gained from this study, it may be possible to improve the performance of GE if the filter components of GE and

the wind turbine prototype components are selected so that the resonant frequencies would be higher.

- The positive and negative-sequence voltage components can be obtained from RTDS reference voltages as well as from the measured voltages using DSOGI-FLL. With these components, it would be possible to implement the control system to have closed-loop control for both positive and negative-sequence fundamental-frequency components. By this way, the unsymmetrical network voltages could be generated accurately.
- The control system of GE is implemented in a synchronous reference frame in the scope of this thesis. However, it would be reasonable to construct the control system in stationary reference frame by using resonant controllers. Because the resonant controller represents, in theory, an infinite gain at the positive and negative sequence fundamental frequency, it is probable that the operation of GE during unsymmetrical faults would improve. In addition, the resonant controllers could be added also to multiple frequencies.

6. Conclusion

The amount of grid connected wind turbines has increased tremendously in recent years due to their environmental friendly energy source. A large penetration of installed wind turbines in many areas has forced power system operators to create grid codes for the operation of wind turbines during the grid disturbances in order to guarantee the stable operation of the power system. In other words, the wind turbines should comply similar requirements during the grid disturbances as demanded from traditional grid connected synchronous generators. The wind turbines should be able to remain in operation and control intelligently their active as well as reactive power during the grid disturbances.

This thesis focuses on the control and operation of the DFIG and FPC wind turbine concepts during the grid disturbances. One of the main features of this thesis is the extensive utilization of real-time simulators in the research. Due to a tremendous number of open literature publications in the field of grid fault operation of the wind turbines, the scope of this thesis is restricted to following specific research areas:

- Impact of FPC wind turbine synchronizing methods on the low voltage ride through capability.
- Control and protection of a DFIG wind turbine during symmetrical voltage dips and voltage recovery.
- Utilization of real-time simulation environment consisting of RTDS and dSPACE real-time simulators in the low voltage ride through studies.
- Performance of extended real-time simulation environment including a wind turbine laboratory prototype and grid emulator.

6.1 Final conclusions

It is revealed in Investigation 1 that DDSRF-PLL may cause the wind turbine to generate undesired DC currents as a result of the symmetrical voltage dip. The problem is not easy to detect, because the unwanted operation occurs only if the loop filter gain of the SRF-PLL part is high enough and the gain normalization is used. It is asserted in this thesis that it is obligatory to limit the loop filter output in order to avoid the DC-current generation. In addition, it is recommended to use the integrator anti-windup arrangement in the loop filter. It is shown in this thesis that with these countermeasures the wind turbine is able to ride through the symmetrical grid fault also with the DDSRF-PLL synchronization method.

A comparison and performance evaluation of NSC synchronization methods SRF-PLL, DDSRF-PLL and DSOGI-FLL is carried out in Investigation 2. The operation of the methods during the symmetrical and unsymmetrical voltage dips, voltage recovery and under the presence of grid voltage harmonics are taken into account in the comparison. The purpose is to investigate the impact of the tuning parameter selection on the overall performance of the synchronization methods. The quality the synchronizing methods is assessed based on how well the wind turbine can generate fundamental-frequency positive sequence currents during the grid disturbances.

It can be concluded that performance of SRF-PLL is poor during the unbalanced grid faults and under the presence of grid voltage harmonics, if the SRF-PLL control bandwidth is high. The performance can be improved by decreasing the control bandwidth. However, this leads to slower response during symmetrical faults, which is undesired. DDSRF-PLL is not interfered by the voltage unbalance, but the operation under the harmonics is identical compared to SRF-PLL. In other words, the bandwidth may need to be limited if the wind turbine is connected to the polluted grid. The performance of DSOGI-FLL is determined by the bandpass filter gain and bandwidth of the normalized FLL gain. The increase of the bandpass filter gain leads to deterioration of harmonic performance. However, the operation becomes faster especially if the normalized FLL gain is small. It is shown that the performance of DDSRF-PLL and DSOGI-FLL are in great agreement with each other although their operations are based on phase and frequency locked loops, respectively. As a conclusion, the simulation results show that the synchronization to the positive-sequence voltage carried out by using DDSRF-PLL or DSOGI-FLL show a superior performance compared to the performance of traditional SRF-PLL.

Wide scale utilization of real-time simulators is one of the main targets of this thesis. The unique real-time simulation environment consisting of RTDS and dSPACE real-time simulators has been constructed in TUT laboratory. The real-time environment provides significant benefits such as very short simulation time, possibility to share the computation power between two simulators and possibility to change control parameters during the simulation. Furthermore, it is possible to use real devices such as electric machines, electric loads or protection relays as a part of the simulations. The operation of the environment is verified against the offline simulation results realized by using Matlab Simulink in Investigation 3. It is shown that the simulation results between the real-time environment and Simulink are in sufficient agreement with each other during steady-state operation. However, greater transients appear in the real-time environment due to the longer simulation step size of the real-time simulators. Approximately 20 ms after the three-phase fault in the verification study, the operations of both simulation environments are in agreement with each other. Therefore, it can be concluded that the real-time

simulation environment is a reliable tool for studies considering the control functions of the grid connected wind turbines. However, when operation of power electronic devices during transients are investigated, the real time simulation environment cannot be considered truly reliable.

Real-time simulation model is implemented also for the DFIG wind turbine. The influence of the transient flux and its compensation control on DFIG operation during the symmetrical voltage dip is analyzed in Investigation 4. The transient flux is computed with help of DSOGI-FLL. Based on the estimated transient flux, the current references to cancel the transient flux are generated. It is shown that the whole RSC current capacity can be utilized for reactive power injection with the transient flux control strategy. Therefore, the reactive current injection and capacitive reactive power generation can be maximized without a fear of repetitive crowbar activation. It can also be noticed that the transient flux compensation control enhances the quality of generated currents during the fault compared to the case, where the transient flux is not compensated in the control system of RSC.

The operation of DFIG during voltage recovery is analyzed in Investigation 5. It is shown that the voltage recovery may be significantly delayed if too small crowbar resistance, proposed in some literature publications, is used. The delayed voltage recovery should be avoided, because it may lead even to the network voltage collapse, especially, if there are induction motor loads connected to the vicinity grid. It is proposed that the crowbar structure with different crowbar resistances during the fault and under the voltage recovery should be used. By this way, the impact of the crowbar activation during the voltage recovery, which is the root cause of the delayed voltage recovery, can be decreased.

The laboratory test setup for a wind turbine prototype is constructed in TUT laboratory. The setup can be considered as an extended real-time simulation environment, because it utilizes RTDS and dSPACE simulators in addition to the low-power-scale prototype of the wind turbine. The PCC voltages for the prototype wind turbine are executed by GE based on the RTDS simulation. The performance of GE is analyzed in detail by using frequency and time domain measurements. The target of the research is to find out how well GE can generate the RTDS-given-reference voltages to the PCC of the prototype and what are the factors, which limits the bandwidth of the emulator voltage control. It is shown that in steady state, the open-loop-controlled GE cannot execute correctly the PCC voltages independent on the operation point of the wind turbine. However, the positive-sequence fundamental-frequency voltages can be generated if GE is closed-loop controlled.

It is revealed in Investigation 6 that the frequency-response measurement of the grid-voltage sequence components is not straightforward and requires a special measurement arrangement. It can also be seen from the frequency response measurements that the control bandwidth of GE is limited. The main limiting factors are the resonances of the passive reactive components, which are mainly converter filters, installed in the laboratory setup. It is also revealed that the tuning of the emulator voltage control loop is dependent on the reactive components associated to the connected device in addition to the emulator filter components. In other words, the optimal tuning of the emulator cannot be done in a situation, when the emulator supplies only resistive load. The impact of the resonance to the control bandwidth was decreased by using a notch filter in the resonant frequency in the control system. However, the fundamental-frequency negative-sequence gain and phase errors were not totally eliminated. Therefore, as analyzed in Investigation 7, the closed-loop-controlled emulator is not able to generate asymmetrical voltage dips perfectly in time domain. Nevertheless, the accuracy of the emulator is sufficient for the testing and verifying the operation of wind turbine control functions under the symmetrical and unsymmetrical voltage dips. These functions may include, for example, balancing of the PCC voltages or positive-sequence reactive-current injection during the fault.

6.2 Future research topics

The research carried out as a part of this thesis elucidated various questions that could be potential future research topics.

- Asymmetrical operation of the wind turbines would be interesting subject from the research point of view although the grid codes do not typically require it. [33, 97] From the power system point of view, the wind turbine with this capability should not be seen only as a source of positive-sequence active and reactive currents anymore. As a matter of fact, the wind turbine would operate as an active power generating compensator (e.g. STATCOM) from the power system point of view. It is possible to implement this functionality to the control system of the wind turbine.
- How wind turbine control system should be designed to actively detect the islanding of the power system? In other words, how the wind turbine should be controlled to force the network voltage or frequency outside the boundary settings of the islanding protection in the case of islanding of a radial feeder? This question is strongly related to the operation of the NSC synchronization system. The active islanding detection is a challenging task, because the islanding should be detected reliably and quickly without adverse impact to the generated power quality during

normal operation. In addition, the islanding detection should not be in conflict with the low voltage ride through.

- Impact of reactive power support of the wind turbine during the fault and voltage recovery on the stability of nearby located induction machines. As explained in Section 4.5, the operation of induction motor during the voltage recovery is problematic because of the increased reactive power consumption. Can the reactive power support of wind turbines prevent the induction motor stalling during the voltage recovery? What is the impact of the network strength and motor loading? The PHIL environment introduced in Chapter 5 would be suitable environment for studies of this topic.
- The inertia in the networks located, for example, in islands is typically small due to the small number of synchronous machines installed in the network. At the same time, the wind conditions may be good from the wind power generation point of view. Therefore, the wind turbines should be able to provide inertia to the small sized network. For example, the FPC wind turbine does not naturally counteract against the grid-voltage frequency changes. Thus, the capability of variable-speed wind turbine to generate artificial inertia would be important research subject.

References

[1] World Wind Energy Association, “World wind energy report 2014,” World Wind Energy Association, 2014.

[2] T. Ackermann, *Wind power in power systems*, Chichester, West Sussex: John Wiley & Sons Ltd, 2005, p. 691.

[3] MHI Vestas Offshore Wind, “V164-8.0 MW breaks world record for wind energy production,” MHI Vestas Offshore Wind, 21 10 2014. [Online]. Available: http://www.mhivestasoffshore.com/v164-8-0-mw-breaks-world-record-for-wind-energy-production/. [Accessed 31 12 2015].

[4] F. Blaabjerg and K. Ma, “Future on power electronics for wind turbine systems,” *IEEE Journal of Emerging and Selected Topics in Power Electronics,* vol. 1, no. 3, pp. 139-152, 2013.

[5] European Wind Energy Association, “Wind energy's frequently asked questions,” European Wind Energy Association, 31 12 2015. [Online]. Available: http://www.ewea.org/wind-energy-basics/wind-energy-faq/. [Accessed 31 12 2015].

[6] V. Yaramasu, B. Wu, P. Sen, S. Kouro and M. Narimani, “High-power wind energy conversion systems: State-of-the-art and emerging technologies,” *Proceedings of the IEEE,* vol. 103, no. 5, pp. 740-788, 2015.

[7] J. M. Carrasco, L. G. Franquelo, J. T. Bialasiewicz, E. Galvan, R. C. Guisado, M. Prats, J. I. Leon and N. Moreno-Alfonso, “Power-electronic systems for the grid integration of renewable energy sources: a survey,” *IEEE Transactions on Industrial Electronics,* vol. 53, no. 4, pp. 1002-1016, 2006.

[8] S. Muller, M. Deicke and R. W. De Doncker, "Doubly fed induction generator systems for wind turbines," *IEEE Industry Application Magazine,* vol. 8, no. 3, pp. 26-33, 2002.

[9] R. Cardenas, R. Pena, S. Alepuz and G. Asher, "Overview of control systems for operation of DFIGs in wind energy applications," *IEEE Transactions on Industrial Electronics,* vol. 60, no. 7, pp. 2776-2798, 2013.

[10] M. Liserre, R. Cardenas, M. Molinas and J. Rodriguez, "Overview of multi-MW wind turbines and wind parks," *IEEE Transactions on Industrial Electronics,* vol. 58, no. 4, pp. 1081-1095, 2011.

[11] N. Jenkins, R. Allan, P. Crossley, D. Kirschen and G. Strbac, *Embedded generation*, London: IEE Power and Energy Series 31, 2000, p. 273.

[12] UCTE Disturbance Investigation Commitee, "Final report system disturbance on 4 november 2006," Union for the Co-ordination of Transmission of Electricity, Brussels, 2006.

[13] European Regulator's Group for Electricity and Gas, "The lessons to be learned from the large disturbance in the European power system on the 4th of November 2006," European Regulator's Group for Electricity and Gas, Bussels, 2007.

[14] E.ON Netz Gmbh, "Grid code - High and extra high voltage," 2006.

[15] M. Mohseni and S. M. Islam, "Review of international grid codes for wind power integration: Diversity, technology and a case for global standard," *Renewable and Sustainainable Energy Reviews,* vol. 16, no. 6, pp. 3876-3890, 2012.

[16] M. Tsili and S. Papathanassiou, "A review of grid code technical requirements for wind farms," *IET Renewable Power Generation,* vol. 3, no. 3, pp. 308-332, 2009.

[17] M. Altin, Ö. Göksu, R. Teodorescu, P. Rodriguez, B. B. Jensen and L. Helle, "Overview of recent grid codes for wind power integration," in *12th International Conference on Optimization of Electrical and Electronic Equipment, OPTIM*, Basov, Russia, 2010, pp. 1152-1160.

[18] ENTSO-E, "Network code for "requirements for grid connection applicaple to all generators"," 2013.

[19] Fingrid Plc., "Specifications for the operational performance of power generating facilities," 2013.

[20] R. Ottersten, A. Petersson and K. Pietiläinen, "Voltage sag response of PWM rectifiers for variable speed wind turbines," in *Proceedings of IEE Nordic Workshop on Power and Industrial Electronics*, Trondheim, 2004, p. 8.

[21] K. Pietiläinen, Voltage sag ride-through of AC drives: control and analysis, Doctoral thesis, Department of Electrical Energy Systems, Royal Institute of Technology, Stockholm, 2005, p. 51.

[22] R. A. Epperly, F. L. Hoadley and R. W. Piefer, "Considerations when applying ASD's in continuous processes," *IEEE Transactions on Industry Applications,* vol. 33, no. 2, pp. 389-396, 1997.

[23] C. J. Abbey, "Effect of low voltage ride through (LVRT) characteristic on voltage stability," in *IEEE Power Engineering Society General Meeting*, 2005, pp. 2576-2582.

[24] J. Duran-Gomez, P. N. Enjeti and A. Von Jouanne, "An approach to achieve ride-through of an adjustable-speed drive with flyback converter modules powered by supercapacitors," *IEEE Transactions on Industrial Applications ,* vol. 38, no. 2, pp. 514-522, 2002.

[25] M. Molinas, B. Neass, W. Gullvik and T. Undeland, "Robust wind turbine system against voltage sag with induction generators interfaced to the grid by power electronic converters," *IEEJ Transactions on Industry Applications,* vol. 126, no. 7, pp. 865-871, 2006.

[26] J. F. Conroy and R. Watson, "Low-voltage ride through of a full converter wind turbine with permanent magnet generator," *IET Renewable Power Generation,* vol. 1, no. 3, pp. 182-189, 2007.

[27] G. Michalke, A. D. Hansen and T. Hartkopf, "Fault ride through and voltage support of permanent magnet synchronous generator wind turbines," in *Nordic Wind Power Conference NWPC07*, Roskilde, 2007, p. 7.

[28] J. Morren, J. T. Pietrik and S. W. De Haan, "Voltage dip ride through control of direct-drive wind turbines," in *39th International Universities Power Engineering Conference UPEC*, Bristol, 2004, pp. 934-938.

[29] A. S. Mäkinen, O. Raipala, K. Mäki, S. Repo and H. Tuusa, "Fault-ride through capability of full-power converter wind turbine," *Journal of Energy and Power Engineering,* vol. 4, no. 1, pp. 29-45, 2010.

[30] R. J. Nelson, H. Ma and N. M. Goldenbaum, "Fault ride-through capabilities of Siemens full-converter wind turbines," in *IEEE Power and Energy Society General Meeting*, San Diego, 2011, p. 5.

[31] V. Akhmatov, “Modelling and ride-through capability of variable speed wind turbines with permanent magnet generators,” *Wind Energy,* vol. 9, no. 4, pp. 313-326, 2006.

[32] A. S. Mäkinen and H. Tuusa, "Analysis, comparison and performance evaluation of wind turbine synchronizing methods," in *IEEE International Conference on Computer as a Tool, EUROCON*, Zagreb, 2013, p. 8.

[33] R. Teodorescu, M. Liserre and P. Rodriguez, *Grid converters for photovoltaic and wind power systems*, West Sussex, United Kingdom: John Wiley & Sons, Ltd, 2011, p. 398.

[34] S. K. Chung, "A phase tracking system for three phase utility interface inverters," *IEEE Transactions on Power Electronics,* vol. 15, no. 3, pp. 431-438, 2000.

[35] F. Blaabjerg, R. Teodorescu, M. Liserre and A. V. Timbus, "Overview of control and grid synchronization for distributed power generation systems," *IEEE Transactions on Industrial Electronics,* vol. 53, no. 5, pp. 1398-1409, 2006.

[36] V. Kaura and V. Blasko, “Operation of a phase locked loop system under distorted utility conditions,” *IEEE Transactions on Industry Applications,* vol. 33, no. 1, pp. 58-63, 1997.

[37] M. Boyra and J. Thomas, "A review on synchronizing methods for grid-connected three-phase VSC under unbalanced and distorted conditions," in *14th European Conference on Power Electronics and Applications, EPE*, Birmingham, 2011, p. 10.

[38] P. Rodriguez, J. Pou, J. Bergas, J. I. Candela, R. P. Burgos and D. Boroyevich, "Decoupled double synchronous reference frame PLL for power converters control," *IEEE Transactions on Power Electronics,* vol. 22, no. 2, pp. 584-592, 2007.

[39] P. Rodriguez, R. Teodorescu, I. Candela, A. V. Timbus, M. Liserre and F. Blaabjerg, "New positive sequence voltage detector for grid synchronization of power converters under faulty grid conditions," in *IEEE 37th Power Electronics Specialists Conference*, Jeju, Korea, 2006, pp. 1492-1498.

[40] X. Guo, W. Wu and Z. Chen, "Multiple-complex coefficient-filter-based phase-locked-loop and synchronization technique for three-phase grid-interfaced converters in distributed utility networks," *IEEE Transactions on Industrial Electronics,* vol. 58, no. 4, pp. 1194-1204, 2011.

[41] C. Blanco, D. Reigosa, F. Briz, J. M. Guerrero and P. Garcia, "Grid synchronization of three-phase converters using cascaded complex vector filter PLL," in *IEEE Energy Conversion Congress and Exposition, ECCE*, Raleigh, 2012, pp. 196-203.

[42] F. Wang, M. C. Benhabib, J. L. Duarte and M. A. Hendrix, "High performance stationary frame filters for symmetrical sequences or harmonics separation under a variety of grid conditions," in *IEEE Applied Power Electronics Conference and Exposition, APEC*, Washington DC, 2009, pp. 1570-1576.

[43] P. Rodriguez, A. Luna, R. S. Munoz-Aguilar, I. Etxeberria-Otadui, R. Teodorescu and F. Blaabjerg, "A stationary reference frame grid synchronization systems for three-phase grid connected power converters under adverse grid conditions," *IEEE Transactions on Power Electronics,* vol. 27, no. 1, pp. 99-112, 2012.

[44] P. Rodriguez, A. Luna, M. Ciobotaru, R. Teodorescu and F. Blaabjerg, "Advanced grid synchronization system for power converters under unbalanced and distorted operating conditions," in *IEEE 32nd Annual Conference on Industrial Electronics, IECON*, Paris, 2006, pp. 5173-5178.

[45] P. Rodriguez, A. Luna, I. Candela, R. Teodorescu and F. Blaabjerg, "Grid synchronization of power converters using multiple second order generalized integrators," in *IEEE 34th Annual Conference on Industrial Electronics, IECON*, Orlando, 2008, pp. 755-760.

[46] J. Lopez, P. Sanchis, X. Roboam and L. Marroyo, "Dynamic behaviour of the doubly fed induction generator during three-phase voltage dips," *IEEE Transactions on Energy Conversion,* vol. 22, no. 3, pp. 709-717, 2007.

[47] J. Niiranen, "Second generation active crowbar for doubly fed generators," in *Nordic Wind Power Conference, NORPIE*, Espoo, 2006, p. 4.

[48] A. D. Hansen and G. Michalke, “Fault ride-through capability of DFIG wind turbines,” *Renewable Energy,* vol. 32, no. 9, pp. 1594-1610, 2007.

[49] F. Sulla, Fault behavior of wind turbines, Doctoral thesis, Department of Measurement Technology and Industrial Electrical Engineering, Lund University, 2012, p. 140.

[50] C. Chen, J. Guerrero and F. Blaabjerg, “A review of the state of the art of power electronics for wind turbines,” *IEEE Transactions on Power Electronics,* vol. 24, no. 8, pp. 1859-1875, 2009.

[51] M. Rodriquez, G. Abad, I. Sarasola and A. Gilabert, "Crowbar control algorithms for doubly fed induction generator during voltage dips," in *European Conference on Power Electronics and Applications, EPE*, Dresden, 2005, p. 10.

[52] Z. Peng and H. Yikang, "Control strategy of an active crowbar for DFIG based wind turbine under grid voltage dips," in *International Conference on Electrical Machines and Systems, ICEMS*, Seoul, 2007, pp. 259-264.

[53] G. Pannel, D. J. Atkinson and B. Zahawi, "Minimum-threshold crowbar for a fault-ride-through grid-code-compliant DFIG wind turbine," *IEEE Transactions on Energy Conversion,* vol. 25, no. 3, pp. 750-759, 2010.

[54] J. Morren and S. W. de Haan, "Ridethrough of wind turbines with doubly-fed induction generator during a voltage dip," *IEEE Transactions on Energy Conversion,* vol. 20, no. 2, pp. 435-441, 2005.

[55] J. Lopez, E. Gubia, E. Olea, J. Ruiz and L. Marroyo, “Ride through of wind turbines with doubly fed induction generator under symmetrical voltage dips,” *IEEE Transactions on Industrial Electronics,* vol. 56, no. 10, pp. 4246-4254, 2009.

[56] F. K. Lima, A. Luna, P. Rodriguez, E. H. Watanabe and F. Blaabjerg, "Rotor voltage dynamics in the doubly fed induction generator during grid faults," *IEEE Transactions on Power Electronics,* vol. 25, no. 1, pp. 118-130, 2010.

[57] J. Yang, J. E. Fletcher and J. O'Reilly, "A series-dynamic-resistor-based converter protecton scheme for doubly-fed induction generator during various fault conditions," *IEEE Transactions on Energy Conversion,* vol. 25, no. 2, pp. 422-432, 2010.

[58] G. Pannel, B. Zahawi, D. J. Atkinson and P. Missailidis, "Evaluation of the performance of a DC-link brake chopper as a DFIG low voltage ride through device," *IEEE Transactions on Energy Conversion,* vol. 28, no. 3, pp. 535-542, 2013.

[59] A. H. Kasem, E. F. El-Saadany, H. H. El-Tamaly and M. A. Wahab, “An improved fault ride through strategyfor doubly fed induction generator based wind turbines,” *IET Renewable Power Generation,* vol. 2, no. 4, pp. 201-214, 2008.

[60] C. Wessels, F. Gebhardt and F. W. Fuchs, "Fault ride-through of a DFIG wind turbine using a dynamic voltage restorer during symmetrical and asymmetrical grid faults," *IEEE Transactions on Power Electronics,* vol. 26, no. 3, pp. 807-815, 2011.

[61] W. Qiao, G. K. Venayagamoorthy and R. G. Harley, "Real-time implementation of a STATCOM on a wind farm equipped with doubly fed induction generators," *IEEE Transactions on Industry Applications,* vol. 45, no. 1, pp. 98-107, 2009.

[62] M. Mohammadi, M. Gitizadeh and A. Roosta, "Dynamic stability improvement of a power system incorporating DFIG wind power plant using optimized control parameters of a SVC," in *IEEE International Power Engineering and Optimization Conference, PEDCO*, Melaka, 2012, pp. 416-421.

[63] C. Wessel and F. W. Fuchs, "Fault ride through of DFIG wind turbines during symmetrical voltage dip with crowbar or stator current feedback solution," in *IEEE Energy Conversion Congress and Exposition, ECCE*, Atlanta, 2010, pp. 2771-2777.

[64] J. Lopez, E. Gubia, P. Sanchis, X. Roboam and L. Marroyo, "Wind turbines based on doubly fed induction generator under asymmetrical voltage dips," *IEEE Transactions on Energy Conversion,* vol. 23, no. 1, pp. 321-330, 2008.

[65] S. Seman, J. Niiranen and A. Arkkio, "Ride-through analysis of doubly fed induction wind-power generator under unsymmetrical network disturbance," *IEEE Transactions on Power systems,* vol. 21, no. 4, pp. 1782-1789, 2006.

[66] K. Mäki, A. Kulmala, S. Repo and P. Järventausta, "Studies of grid impacts of distributed generation on a combined real-time simulation environment," in *7th International Conference on Power System Transients*, Lyon, 2007, p. 6.

[67] A. Mäkinen and H. Tuusa, "Wind turbine and grid interaction studies using integrated real-time simulation environment," in *Nordic Workshop on Power and Industrial Electronics*, Espoo, 2008, p. 8.

[68] J. G. Slootweg and W. L. Kling, "Is the answer blowing in the wind," *IEEE Power & Energy Magazine,* vol. 1, no. 6, pp. 26-33, 2003.

[69] W. Li, G. Joos and J. Belanger, "Real-time simulation of a wind turbine generator coupled with a battery supercapacitor energy storage system," *IEEE Transactions on Industrial Electronics,* vol. 57, no. 4, pp. 1137-1145, 2010.

[70] J. Langston, M. Steurer, S. Woodruff, T. Baldwin and J. Tang, "A generic real-time computer simulation model for superconducting fault current limiters and its application in system protection studies," *IEEE Transactions on Applied Superconductivity,* vol. 15, no. 2, pp. 2090-2093, 2005.

[71] A. Mackay, S. Galloway, C. Booth and J. R. McDonald, "Real-time assessment of relay protection schemes on integrated full electric propulsion systems," in *IEEE Electric Ship Technologies Symposium*, Philadelphia, 2005, pp. 230-236.

[72] J. H. Jeon, J. Y. Kim, H. M. Kim, S. K. Kim, C. Cho, J. M. Kim, J. B. Ahn and K. Y. Nam, "Development of hardware in-the-loop simulation system for testin operation and control functions of microgrid," *IEEE Transactions on Power Electronics,* vol. 25, no. 12, pp. 2919-2929, 2010.

[73] G. H. Kim, J. Y. Kim, J. H. Jeon, S. K. Kim, E. S. Kim, J. H. Lee, M. Park and I. K. Yu, "Hardware-in-the-loop simulation method for a wind farm controller using real time digital simulator," *Journal of Electrical Engineering Technology,* vol. 9, no. 5, pp. 1489-1494, 2014.

[74] Y. Li, D. M. Vilathgamuwa and P. C. Loh, "Design, analysis and real-time testing of a controller for multibus microgrid system," *IEEE Transactions on Power Electronics,* vol. 19, no. 5, pp. 1195-1204, 2004.

[75] S. Ayasun, S. Vallieu, R. Fischi and T. Chmielewski, "Electric machinery diagnostic/testing system and power hardware-in-the-loop studies," in *4th IEEE International Symposium on Diagnostics for Electric Machines, Power Electronics and Drives, SDEMPED*, Atlanta, 2003, pp. 361-366.

[76] P. Kotsampopoulos, V. Kleftakis, G. Messinis and N. Hatziargyriou, “Design, development and operation of a PHIL environment for distributed energy resources,” in *Annual Conference on IEEE Industrial Electronics Society, IECON*, Montreal, Canada, 2012, pp. 4765-4770.

[77] G. Byeon, I. K. Park and G. Jang, "Modeling and control of a doubly fed induction generator (DFIG) wind power generation system for real-time simulations," *Journal of Electrical Engineering & Technology,* vol. 5, no. 1, pp. 61-69, 2010.

[78] M. Singh, E. Muljadi and V. Gevorgian, "Test cases for wind power plant dynamic models on real time digital simulator," in *IEEE Symposium on Power Electronics and Machines in Wind Applications*, Denver, 2012, p. 7.

[79] P. P. Groenewoud, R. L. Hendriks, B. C. Ummels and W. L. Kling, "Real-time digital simulation of a VSC-connected offshore wind farm," in *Nordic Wind Power Conference, NWPC*, Roskilde, 2007, p. 7.

[80] P. Mitra and L. Zhang, "Real-time simulation of a wind connected HVDC grid," in *10th IET International Conference on AC and DC Power Transmission, ACDC*, Birmingham, 2012, p. 6.

[81] R. Teodorescu and F. Blaabjerg, "Flexible control of small wind turbines with grid failure detection operating in stand-alone and grid connected mode," *IEEE Transactions on Power Electronics,* vol. 19, no. 5, pp. 1323-1332, 2004.

[82] J. A. Suul, A. Luna, P. Rodriguez and T. Undeland, "Voltage-sensor-less synchronization to unbalanced grids by frequency-adaptive virtual flux estimation," *IEEE Transactions on Industrial Electronics,* vol. 59, no. 7, pp. 2910-2922, 2012.

[83] P. Lauttamus and H. Tuusa, "Model-based cascade control of three-level STATCOM with tuned LCL-filter," in *26th Annual IEEE Applied Power Electronics Conference and Exposition, APEC*, Forth Worth, 2011, pp. 1569-1575.

[84] P. Parkatti, H. Tuusa, H. Saren, K. Kuusela and M. Björkman, "Analysis and performance of a high-efficiency transformerless hybrid active filter," *Inernational Review of Electrical Engineering, I.R.E.E.,* vol. 6, no. 2, pp. 537-546, 2011.

[85] A. S. Mäkinen, T. Messo and H. Tuusa, "Power hardware-in-the-loop laboratory test environment for small scale wind turbine," in *16th European Conference on Power Electronics and Applications, EPE*, Lappeenranta, 2014, p. 10.

[86] A. S. Mäkinen, P. Lauttamus, O. Raipala, S. Repo and H. Tuusa, "Fault ride through study of doubly fed induction generator wind turbine in real time simulation environment," in *14th European Conference on Power Electronics and Applications, EPE*, Birmingham, 2011, p. 10.

[87] A. S. Mäkinen, O. Rapala, S. Repo and H. Tuusa, "Influence of DFIG wind turbine protection and control during voltage dip on circuit breaker operation," *Journal of Energy and Power Engineering,* vol. 7, no. 1, pp. 126-138, 2013.

[88] K. Mäki, A. Kulmala, S. Repo, P. Järventausta, P. Parkatti and H. Tuusa, "Real-time simulation environment for power system studies using RTDS and dSPACE simulators," in *Nordic Workshop on Power and Industrial Electronics, NORPIE*, Lund, 2007, p. 7.

[89] R. Pöllänen, L. Kankainen, J. Pääkkönen, S. Ollila and S. Strandberg, “Full-power converter based test bench for low voltage ride-through testing of wind turbines,” in *14th European Conference on Power Electronics and Applications, EPE11*, Birmingham, Great Britain, 2011, p. 10.

[90] C. Wessels, T. Wehrend and F. W. Fuchs, “Transformer based voltage sag generator to test renewable energy systems during grid faults in the lapaboratory,” in *EPE Wind Energy Chapter Symposium*, Stafford, United Kingdom, 2010, p. 8.

[91] M. Garcia-Gracia, M. P. Comech, J. Sallan and D. Lopez-Andia, “Voltage dip generator for wind energy systems up to 5MW,” *Applied Energy,* vol. 86, no. 4, pp. 565-574, 2009.

[92] J. Niiranen, “Experiences on voltage dip ride through factory testing of synchronous and doubly fed generator drives,” in *European Conference on Power Electronics and Applications, EPE*, Dresden, Germany, 2005, p. 11.

[93] S. Seman, J. Niiranen, R. Virtanen and J. P. Matsinen, "Low voltage ride-through analysis of 2 MW DFIG wind turbine - grid code compliance validations," in *Power and Energy Society General Meeting*, Pittsburgh, 2008, p. 6.

[94] S. Lentijo, S. D'Arco and A. Monti, "Comparing the dynamic performances of power hardware-in-the-loop interfaces," *IEEE Transactions on Industrial Electronics,* vol. 57, no. 4, pp. 1195-1207, 2010.

[95] W. Ren, M. Sloderbeck, M. Steurer, V. Dinavahi, T. Noda, S. Filizadeh, A. R. Chevrefils, M. Matar, R. Iravani, C. Dufour, J. Belanger, M. O. Faruque, K. Strunz and J. A. Martinez, "Interfacing issues in real-time digital simulators," *IEEE Transactions on Power Delivery,* vol. 26, no. 2, pp. 1221-1230, 2011.

[96] N. R. Averous, M. Stieneker, S. Kock, C. Andrei, A. Helmedag, R. W. De Doncker, K. Hameyer, G. Jacobs and A. Monti, "Development of a 4 MW full-size wind-turbine test bench," in *6th International Symposium on Power Electronics for Distributed Generation Systems, PEDG*, Aachen, 2015, p. 8.

[97] P. Rodriguez, A. V. Timbus, R. Teodorescu, M. Liserre and F. Blaabjerg, "Flexible active power control of distributed power generation systems during grid faults," *IEEE Transactions on Industrial Electronics,* vol. 54, no. 5, pp. 2583-2592, 2007.

[98] A. H. Al-Mubarak, B. Thorvaldsson, M. Halonen and M. Z. Al-Kadhem, "Hybrid and classic SVC technology for improved efficiency and reliability in Saudi transmission grid," in *IEEE PES T&D Conference and Exposition*, Chigaco, 2014, p. 8.

[99] A. Luna, C. Citro, C. Gavriluta, J. Hermoso, I. Candela and P. Rodriguez, "Advanced PLL structures for grid synchronization in distributed generation," in *International Conference on Renewable Energies and Power Quality*, Santiago de Compostela, 2012, p. 10.

[100] S. Gao and M. Barnes, "Phase-locked loop for AC systems: analysis and comparison," in *6th International Conference on Power Electronics and Drives*, Bristol, 2012, p. 6.

[101] J. Morren and S. W. H. de Haan, “Short-circuit current of wind turbines with doubly fed induction generator,” *IEEE Transactions on Energy Conversion,* vol. 22, no. 1, pp. 174-180, 2007.

[102] B. Gong, D. Xu and B. Wu, “Cost effective method for DFIG fault ride through during symmetrical voltage dip,” in *36th Annual Conference on IEEE Industrial Electronics Society*, Glendale, 2010, pp. 3269-3274.

[103] V. Akhmatov, Analysis of dynamic behaviour of electric power systems with large amount of wind power, Doctoral thesis, Electric Power Engineering, Technical University of Denmark, Lyngby, 2003, p. 261.

[104] A. Perdana, Dynamic models of wind turbines, Doctrola thesis, Department of Energy and Environment, Chalmers University of Technology, Göteborg, 2008, p. 199.

[105] T. Sun, Z. Chen and F. Blaabjerg, “Voltage recovery of grid connected wind turbines with DFIG after short-circuit fault,” in *Annual IEEE Power Electronic Specialists Conference*, Aachen, 2004, pp. 1991-1997.

[106] P. Kundur, J. Paserba, V. Ajjarapu, G. Andersson, A. Bose, C. Canizares, N. Hatziargyriou, D. Hill, A. Stankovic, C. Taylor, T. Van Cutsem and V. Vittal, “Definition and classification of power system stability,” *IEEE Transactions on Power Systems,* vol. 19, no. 2, pp. 1387-1401, 2004.

[107] I. Erlich, H. Wrede and C. Feltes, “Dynamic behaviour of DFIG-based wind turbines during grid faults,” in *Power Conversion Conference*, Nagoya, 2007, pp. 1195-1200.

[108] A. Mäkinen and H. Tuusa, "Effect of transient flux compensation control on fault ride through of doubly fed induction generator wind turbine," in *International Conference on Renewable Energies and Power Quality*, Las Palmas, 2011, p. 6.

[109] D. Xiang, L. Ran, P. J. Tavner and S. Yang, "Control of a doubly fed induction generator in a wind turbine during grid fault ride-through," *IEEE Transactions on Energy Conversion,* vol. 21, no. 3, pp. 652-662, 2006.

[110] A. J. Roscoe, A. Mackay, G. M. Burt and J. R. McDonald, “Architecture of a network in-the-loop environment for AC power system behaviour,” *IEEE Transactions on Industrial Electronics,* vol. 57, no. 4, pp. 1245-1253, 2010.

[111] M. Steurer, C. S. Edrinton, M. Sloderbeck, W. Ren and J. Langston, "A megawatt-scale power hardware-in-the-loop setup for motor drives," *IEEE Transactions on Industrial Electronics,* vol. 57, no. 4, pp. 1254-1260, 2010.

[112] R. Lohde and F. W. Fuchs, "Laboratory type PWM grid emulator for generating disturbed voltages for testing grid connected devices," in *13th European Conference on Power Electronics and Applications*, Barcelona, 2009, p. 9.

[113] S. Heier, *Grid integration of wind energy conversion systems*, Chicester, West Sussex: John Wiley & Sons Ltd, 1998, p. 385.

[114] P. Kundur, *Power system stability and control*, McGraw-Hill, Inc, 1994, p. 1176.

[115] P. Vas, *Electrical machines and drives: a space vector approach*, Oxford: Clarendon Press, 1992, p. 808.

[116] B. K. Bose, *Power electronics and variable frequency drives*, technology and applications, New York: IEEE Press, 1997, p. 640.

[117] J. G. Njiri, D. Söffker, "State-of-the-art wind turbine control: Trends and challenges," Renewable and Sustainable Energy Reviews, vol. 60, issue C, pp. 377-393, 2016.

[118] G. Michalke, A. D. Hansen and T. Hartkopf, "Control strategy of a variable speed wind turbine with multipole permanent magnet synchronous generator," in *European Wind Energy Conference*, Milan, Italy, 2007, p. 8.

[119] M. Liserre, F. Blaabjerg and S. Hansen, "Design and control of an LCL-filter based three-phase active rectifier," *IEEE Transactions on Industry Applications,* vol. 41, no. 5, pp. 1281-1291, 2005.

[120] M. Liserre, F. Blaabjerg and A. Dell' Aquila, "Step-by-step procedure for a grid-connected three-phase PWM voltage source converter," International Journal of Electronics, vol 91, no. 8, pp. 445-460, 2004.

[121] V. Blasko and V. Kaura, "A novel control to actively damp resonance in input LC filter of a three-phase voltage source converter," IEEE Transactions on Industry Applications, vol. 33, no. 2, pp. 542-550, 1997.

[122] P. Vas, *Vector control of AC machines*, Oxford: Clarendon Press, 1990, p. 332.

[123] P. Parkatti, Transformerless active harmonic filtering using series-connected supply filter capacitors, Doctoral thesis, Department of Electrical Energy Engineering, Tampere University of Technology, 2011, p. 159.

[124] G. F. Franklin, J. D. Powell and M. Workman, *Digital control of dynamic systems*, 3rd edition, Addison Wesley Longman, Inc, 1998, p. 742.

[125] H. Akagi, E. H. Watanabe and M. Aredes, *Instantaneous power theory and applications to power conditioning*, New Jersey, United States: John Wiley & Sons, Inc, 2007, p. 379.

[126] K. J. Åström and T. Hägglund, *Advanced PID control*, United States: ISA - Instrumentation, Systems nd Automation Society, 2006, p. 460.

[127] H. Markiewicz and A. Klajn, "Voltage disturbances. Standard EN 50160 - Voltage characteristics in public distribution systems," July 2014. [Online]. Available: http://www.leonardo-

energy.org/repository/Library/PQGuide/5.Voltage%20Disturbances/5.4.2%20Standard%20EN50160.pdf.. [Accessed 1 October 2012].

[128] R. Pena, J. C. Clare and G. M. Asher, "Doubly fed induction generator using back-to-back PWM converters and its application to variable-speed wind-energy generation," *IEE Proceedings - Electric Power Applications,* vol. 143, no. 3, pp. 231-241, 1996.

[129] E. W. Kimbark, *Power system stability*, Volume III, New York: A John Wiley & Sons, Inc., 1995, p. 998.

[130] RTDS Technologies, [Online]. Available: https://www.rtds.com/the-simulator/our-hardware/gtio-cards/. [Accessed 14 3 2015].

[131] R. C. Dorf and R. H. Bishop, *Modern control system*, 9 ed., Upper Saddle River, New Jersey, United States: Prentice Hall, Inc, 2001, p. 831.

[132] W. Qiuwei, X. Zhao and J. Ostergaard, “Grid integration issues for large scale wind power plants (WPPs),” in *IEEE Power and Energy Society General Meeting*, Minneapolis, USA, 2010, p. 6.

[133] K. E. Johnson, L. Y. Pao, M. J. Balas and L. J. Fingersh, “Control of variable-speed wind turbines: standard and adaptive techniques for maximizing energy capture,” *IEEE Control Systems*, vol. 26, no. 3, pp.70-81, 2006.

Appendix A

Torque control of GSC

The standard generator torque controller can be expressed as

$$t_e^* = K_T \omega_r^2 \tag{A.1}$$

where K_T is given by

$$K_T = \frac{1}{2}\rho\pi R^5 \frac{c_{pmax}(\beta_{opt}, \lambda_*)}{\lambda_*^3} = \frac{1}{2}\rho A R^3 \frac{c_{pmax}(\beta_{opt}, \lambda_*)}{\lambda_*^3}. \tag{A.2}$$

Here, c_{pmax} corresponds to maximum performance coefficient, β_{opt} is optimal blade pitch angle and λ_* is optimal tip speed ratio to extract maximum power from the wind. The angular acceleration of the generator rotor can be given as

$$\frac{d}{dt}\omega_r = \frac{1}{J'}\left(t_t - t_e^*\right), \tag{A.3}$$

where t_t is aerodynamic torque given by

$$t_t = \frac{P_t}{\omega_r} = \frac{\frac{1}{2}A\rho c_p(\lambda,\beta)v_w^3}{\omega_r} = \frac{\frac{1}{2}AR\rho c_p(\lambda,\beta)v_w^2}{\lambda} = \frac{\frac{1}{2}AR^3\rho\omega_r^2 c_p(\lambda,\beta)}{\lambda^3}. \tag{A.4}$$

Combining Eqs. (A.3) and (A.4) yields

$$\frac{d}{dt}\omega_r = \frac{1}{2J'}AR^3\rho\omega_r^2\left(\frac{c_p(\beta,\lambda)}{\lambda^3} - \frac{c_{pmax}(\beta_{opt},\lambda_*)}{\lambda_*^3}\right). \tag{A.5}$$

Because the turbine inertia, rotor swept area, rotor radius, air density and rotor squared speed are always positive, the sing of the angular acceleration is dependent on the sign if the difference in (A.5). When tip speed ratio in given wind conditions is higher than the optimal tip speed ratio, the difference gives negative output and the generator speed decelerates. On the other hand, when the tip speed ratio is smaller than the optimal tip speed ratio, the generator starts to accelerate. This relation holds true as long as the tip speed ratio is higher than the certain minimum limit. In [133], the limit value for tip speed ratio is 3.3.

Appendix B

Parameter selection in Investigation 2

In this Appendix, the mathematical background for parameter selection in Investigation 2 is presented. It is shown how the normalized FLL gain is selected in order to obtain identical -3 dB bandwidths for FLL and PLL. In addition, it is expressed how the SOGI gain is selected to obtain similar transfer functions for DSOGI and the decoupling network used by DDSRF-PLL.

Analysis of FLL and SRF-PLL

The averaged dynamics of FLL near frequency locked state (ω' ≈ ω) can be expressed as follows [33]

$$\bar{\omega}' = -\frac{\gamma U^2}{k_{\text{SOGI}}\omega'}\left(\bar{\omega}' - \omega\right). \tag{B.1}$$

Taking into account the normalized FLL gain selection in (2.76), the transfer function of the frequency locking loop shown in Fig. B.1 can be given as

$$H_{\text{FLL}} = \frac{\bar{\omega}'}{\omega} = \frac{\Gamma}{s+\Gamma}. \tag{B.2}$$

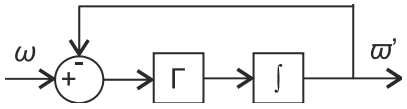

Fig. B.1. Linearized frequency locked loop with normalized FLL gain.

The normalized form transfer function of linearized SRF-PLL (2.54) is represented in below for convenience

$$H_{\text{cl}}(s) = \frac{\theta_{\text{sync}}}{\theta} = \frac{2\varsigma\omega_{\text{n}}s + \omega_{\text{n}}^2}{s^2 + 2\varsigma\omega_{\text{n}}s + \omega_{\text{n}}^2}. \tag{B.3}$$

It can be seen from Fig. B.2a, that the -3 dB bandwidth of SRF-PLL and FLL is 64.5 rad/s when the tuning parameters are selected as follows: ω_{n} = 2π*5 Hz, ς = 0.707 and Γ= 64.5 rad/s. Thus, the x-axis in Investigation 3 consists of Γ values (64.5, 193, 387, 645), which are comparable to SRF-PLL ω_{n} values (2π*5 Hz, 2π*15 Hz, 2π*30 Hz, 2π*50 Hz).

However, it should be noted that the -3 dB bandwidths are not equal anymore, if the damping factor differs from 0.707 as can be seen from Fig. B.2b.

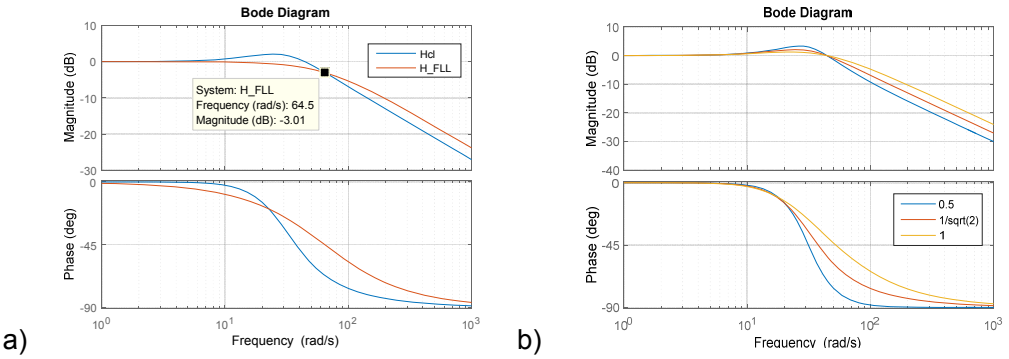

a) b)

Fig. B.2. a) Bode diagram of $H_{\_FLL}$ and $H_{cl}(s)$, b) Bode diagram of linearized SRF-PLL with different damping factors and with ω_h = 2*π*5Hz.

Analysis of decoupling network and DSOGI

The transfer function from positive sequence voltage vector to the grid-voltage vector in the stationary reference frame using DSOGI was calculated in (2.72) and it is expressed in below for convenience

$$\begin{bmatrix} u_\alpha^+ \\ u_\beta^+ \end{bmatrix} = \left[T_{\alpha\beta}^+\right]\begin{bmatrix} u_\alpha \\ u_\beta \end{bmatrix} = \frac{1}{2}\begin{bmatrix} 1 & -q \\ q & 1 \end{bmatrix}\begin{bmatrix} u_\alpha \\ u_\beta \end{bmatrix} = \frac{1}{2}\begin{bmatrix} D(s) & -Q(s) \\ Q(s) & D(s) \end{bmatrix}\begin{bmatrix} u_\alpha \\ u_\beta \end{bmatrix} \\ = \frac{1}{2}\frac{k_{SOGI}\omega'}{s^2 + k_{SOGI}\omega' s + \omega'^2}\begin{bmatrix} s & -\omega' \\ \omega' & s \end{bmatrix}\begin{bmatrix} u_\alpha \\ u_\beta \end{bmatrix}. \quad \text{(B.4)}$$

The transfer function of the decoupling network after conversion into the stationary reference frame can be given as [33]

$$\begin{bmatrix} u_\alpha^+ \\ u_\beta^+ \end{bmatrix} = \frac{\omega_f}{s^2 + 2\omega_f s + \omega'^2}\begin{bmatrix} s & -\omega' \\ \omega' & s \end{bmatrix}\begin{bmatrix} u_\alpha \\ u_\beta \end{bmatrix}, \quad \text{(B.5)}$$

where the ω' is the frequency detected by the PLL.

It can be seen from the equations (B.4) and (B.5) that the transfer functions of DSOGI and the decoupling network are similar, when the following selection for the SOGI gain is chosen

$$k_{\mathrm{SOGI}} = \frac{2\omega_{\mathrm{f}}}{\omega'} . \tag{B.6}$$

This means that the dynamic response of DSOGI and the decoupling network should be in agreement with each other. However, the response of DSOGI depends on the performance of FLL and the response of the decoupling network depends on the PLL performance.

Appendix C

Simulation parameters and network model in Investigations 1 and 2

The wind turbine NSC and filter parameters are shown in Table C.1 and NSC control parameters are presented in Table C.2. The filter design is based on procedure depicted in [119]. Although the converter switching is not modeled, the design of the filter is based on the assumption of 3.6 kHz switching frequency. The filter resonance frequency f_{res} is 1072 Hz. The network model consisting of two parallel feeders is shown in Fig. C.1. In both Investigations, the fault occurs at point Fault 2. The fault is cleared by opening the circuit breakers Cb_{f21} and Cb_{f22}. The network model parameters are shown in Table C.3.

Table C.1. Filter and NSC parameters.

L_1 = 300 μH	L_2 = 83 μH	R_1 = 2.4 mΩ	R_2 = 1 mΩ	C_f = 0.2 mF
R_{cf} = 0.25 Ω	u_{dc}^* = 1100 V	C_{dc} = 22mF	R_{dc} = 2 Ω	$L_{\sigma TF}$ = 90 μH

Table C.2. NSC controller parameters.

Controller	Current	DC-link	Reactive power
Gain	k_i = 0.6	k_{udc} = 4	k_q = -0.45
Integrator time	T_{i_i} = 3 ms	T_{i_udc} = 25 ms	T_{i_q} = 40 ms
Sampling time	T_{s_i} = 100 μs	T_{s_udc} = 100 μs	T_{s_q} = 100 μs
Limitation	$\lvert u_{Lmax} \rvert$ = 100 V	$\lvert i_{L1dmax} \rvert$ = 900 A	$\lvert i_{L1qmax} \rvert$ = 700 A

Table C.3. Network model parameters.

Grid parameters			
V_g = 114 kV	f_g = 50 Hz	R_g = 2.51 Ω	L_g = 0.02 H
R_{f11} = 25.51 Ω	R_{f12} = 1.676 Ω	R_{f21} = 3.351 Ω	R_{f22} = 1.676 Ω
L_{f11} = 0.157 H	L_{f12} = 0.0136 H	L_{f21} = 0.0272 H	L_{f22} = 0.136 H
Transformer parameters			
S_{nTF1} = 20 MVA	S_{nTF2} = 16 MVA	S_{nTF3} = 0.5 MVA	
R_{TF1} = 0.022 pu	R_{TF2} = 0.021 pu	R_{TF3} = 0.001 pu	
L_{TF1} = 0.00117 pu	L_{TF2} = 0.00271 pu	L_{TF3} = 0.03 pu	
TF1: U_1/U_2 = 110/20 kV YΔ	TF2: U_1/U_2 = 110/20 kV YΔ	TF3: U_1/U_2 = 21/0.69 kV ΔY	

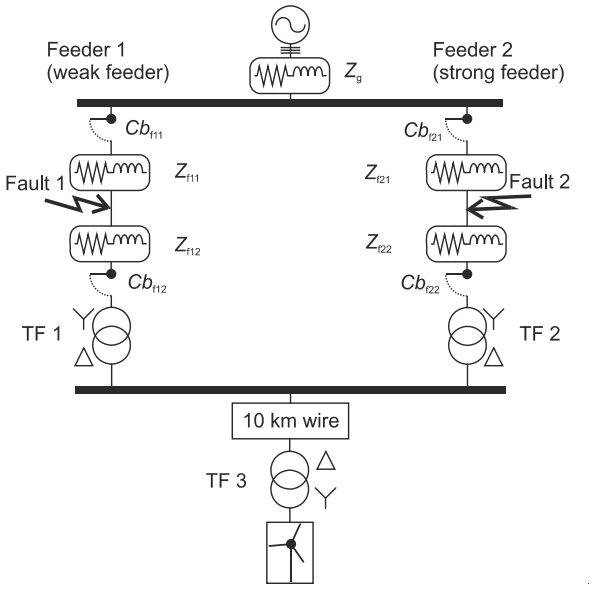

Fig. C.1. Network model used in Investigations 1 and 2.

Appendix D

Wind turbine parameters and grid model used in Investigation 3

The network model used in the verification study is presented in Fig. D.1. The simple network model consists of the ideal wind turbine transformer, two wires, inductive-resistive load and voltage source hidden behind the grid impedance. The wind turbine model is presented in Chapter 2 and the wind turbine parameters are shown in Table D.1. The network model parameters are depicted in Table D.2.

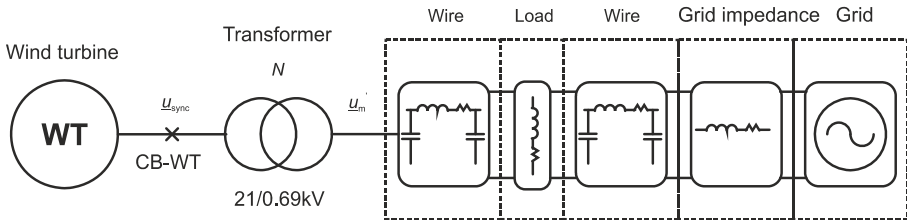

Fig. D.1. Network model used in the verification study.

Table D.1. Parameters wind turbine model.

parameter	value	parameter	value
air density	ρ = 1,25 [kg/m^3]	rotor diameter	37 [m]
permanent magnet flux linkage	ψ_m = 2.29 [Wb]	pole pairs	p = 6
gearbox transmission ratio	n = 10	PMSG power	S = [500kVA]
friction constant	B =0.25 [Nms/rad]	stator inductance	L_d = 0.83 [mH]
aggregated wind turbine inertia	J = 15 [kNms^2/rad]	stator inductance	L_q = 0.88 [mH]
DC-link voltage	u_{dc} = 1100 [V]	filter inductance	L_1 = 350 [µH]
DC-link capacitor	C_{dc} = 5 [mF]	DC chopper resistance	R_{dc} = 2 [Ω]
resonant frequency	f_{res} = 500 [Hz]	filter capacitor	C_f = 1.6 [mF]
filter and transformer inductance	$L_2 + L_\sigma$ = 108 [µH]	switching frequency	f_{sw} = 3000 [Hz]
transformer ratio	N = 29	damping resistance	R_{damp} = 50 [mΩ]

Table D.2. Parameters of the network model.

parameter	**value**	**parameter**	**value**
grid voltage	u_{grid} = 20000 [V]	wire inductance	L_w = 0.0117 [H]
wire resistance	R_w = 5.78 [Ω]	wire capacitance	C_w = 0.1 [μF]
grid resistance	R_{grid} = 5.78 [Ω]	grid inductance	L_{grid} = 0.0117 [H]
load resistance	R_{load} = 361 [Ω]	load inductance	L_{load} = 0.378 [H]

Appendix E

DFIG wind turbine in real-time simulation environment and network model for Investigations 4 and 5

The practical implementation of the DFIG wind turbine model in the real-time simulation environment consisting of RTDS and dSPACE simulators is shown in Fig. E.1. Data transmission between the real-time simulators is done through analogue signals. dSPACE receives the stator voltages $u_{s(a,b,c)}$ from RTDS and gives back the grid currents in two axis components $i_{grid(\alpha,\beta)}$. Thus, the wind turbine is modeled as a current source in RTDS. The interrupt signal *int* is used to synchronize the computation step times of the simulators. dSPACE and RTDS operate with simulation step sizes of 100 µs and 50 µs, respectively.

The grid model is presented in Fig. E.2 and the model parameters are collected in Table E.1. The induction generator, frequency converter and filter models are presented in Chapter 2 and the equivalent circuit of DFIG is shown in Fig. E.3. The parameters of DFIG, RSC and NSC are gathered to Tables E.2, E.3 and E.4, respectively.

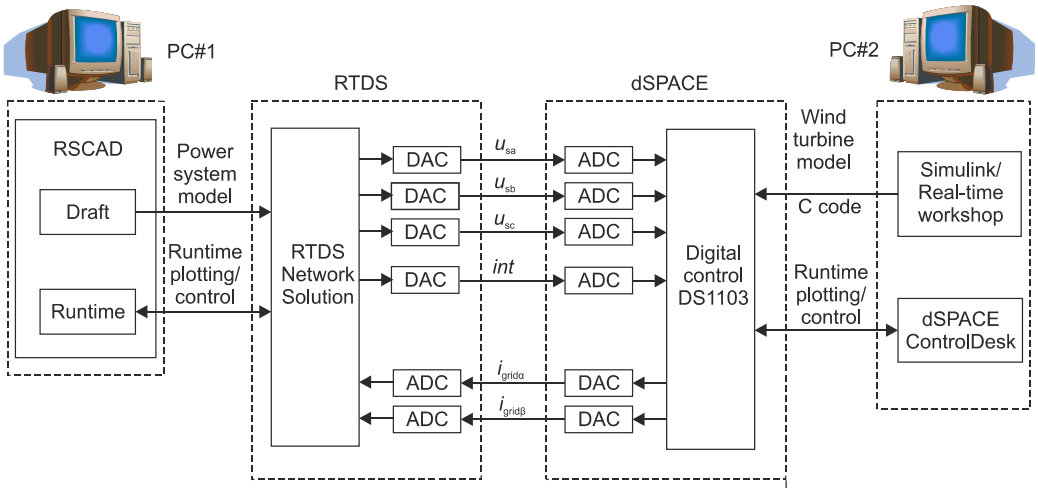

Fig. E.1. Practical implementation of real-time simulation environment for DFIG wind turbine.

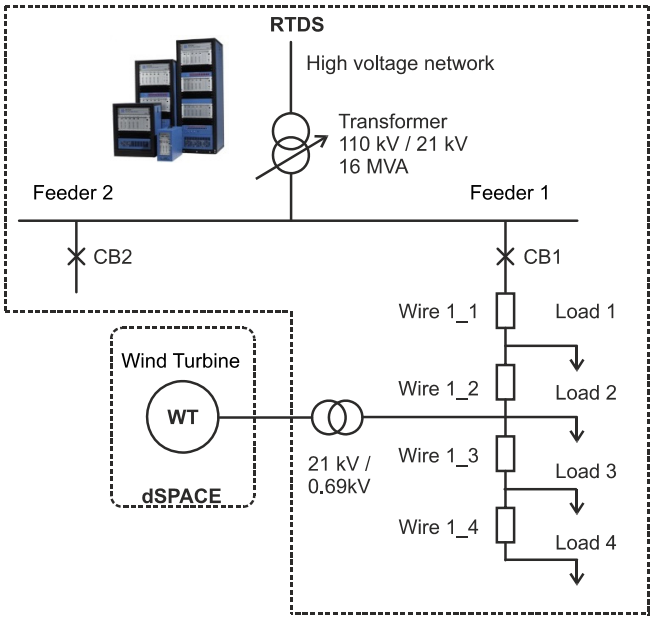

Fig. E.2. Network model used in real-time simulations in Investigations 4 and 5.

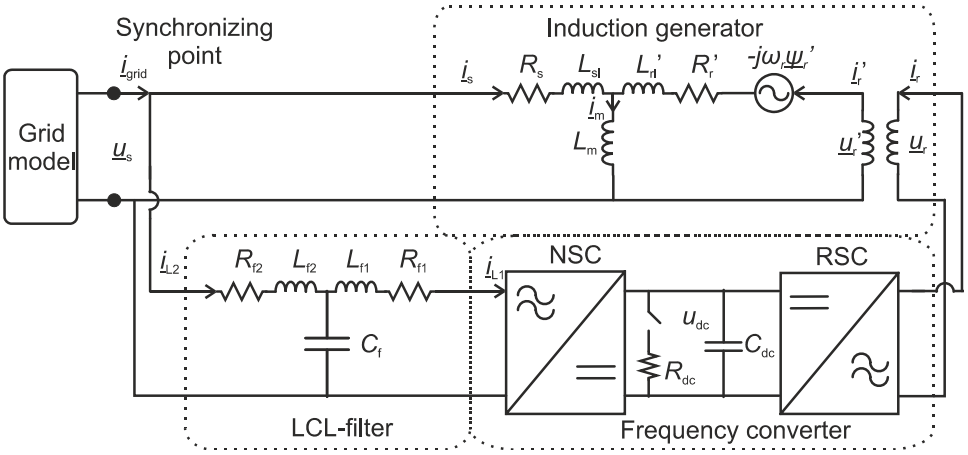

Fig. E.3. Equivalent circuit of DFIG.

Table E.1. Parameters of network model.

Network			
u_g = 110.4 kV	f = 50 Hz	$\left\|Z_g^+\right\|$ = 48 Ω	$\angle Z_g^+$ = 65.8 °
Transformer 110 / 21 kV YY			
S = 16 MVA	L_σ = 0.103pu	No load losses = 0.006 pu	
Load impedance			
R_1 = 3992 Ω	L_1 = 3.6398 H	R_2 = 2481 Ω	L_2 = 2.254 H
R_3 = 6316 Ω	L_3 = 5.7226 H	R_4 = 10967 Ω	L_4 = 9.909 H
Wire 1_1			
R_{w1} = 3.33 Ω	X_{lw1} = 3.27 Ω	B_{cw1} = 0.04 mS	
Wire 1_2			
R_{w2} = 5.31 Ω	X_{lw2} = 3.48 Ω	B_{cw2} = 0.031 mS	
Wire 1_3			
R_{w3} = 7.5 Ω	X_{lw3} = 2.51 Ω	B_{cw3} = 0.019 mS	
Wire 1_4			
R_{w4} = 10.49 Ω	X_{lw4} = 3.7 Ω	B_{cw4} = 0.028 mS	
Transformer 21 / 0.69 kV YD			
S = 1.75 MVA	L_σ = 0.06 pu	No load losses = 0.01 pu	

Table E.2. Parameters of DFIG.

Turbine	R = 38 m	n_{gear} = 100	J = 500 kgm^2	
Generator	P_n = 1700 kW	u_{ll} = 690 V	p = 2	N_r / N_s = 2.73
	L_{sl} = 89 μH	L_{rl} = 92 μH	R_s = 2.7 mΩ	R_r = 2.7 mΩ
	L_m = 3.8 mH			
Filter	L_{f1} = 190 μH	L_{f2} = 125 μH	R_{f1} = 15 mΩ	R_{f2} = 5 mΩ
	C_f = 70 μF			
Converter	u_{dc}^* = 1100V	C_{dc} = 22 mF	R_{dc} = 1.25 Ω	

Table E.3. Control parameters of RSC.

Controller	**Current**	**Torque**	**Speed**	**Reactive power**
Gain	k_i = 1.67	k_t = -0.1	k_w = 300	k_q = -0.5
Integrator time	T_{i_i} = 8 ms	T_{i_t} = 50 ms	T_{i_w} = 5 s	T_{i_q} = 25 ms
Sampling time	T_{s_i} = 100 μs	T_{s_t} = 100 μs	T_{s_w} = 5 ms	T_{s_q} = 100 μs

Table E.4. Control parameters of NSC.

Controller	**Current**	**DC-link**
Gain	$k_i = 0.7$	$k_{udc} = 4$
Integrator time	$T_{i\_i} = 8$ ms	$T_{i\_udc} = 41$ ms
Sampling time	$T_{s\_i} = 100$ µs	$T_{s\_udc} = 100$ µs

Appendix F

Power hardware-in-the-loop environment

The hardware arrangement of the PHIL laboratory test setup analyzed in Investigations 6 and 7 is depicted in Fig. F.1. The wind turbine prototype parameters are collected in Table F.1. The isolation transformer, grid emulator as well as network model parameters are depicted in Tables F.2, F.3 and F.4, respectively. The RTDS network model is presented in Fig. F.2.

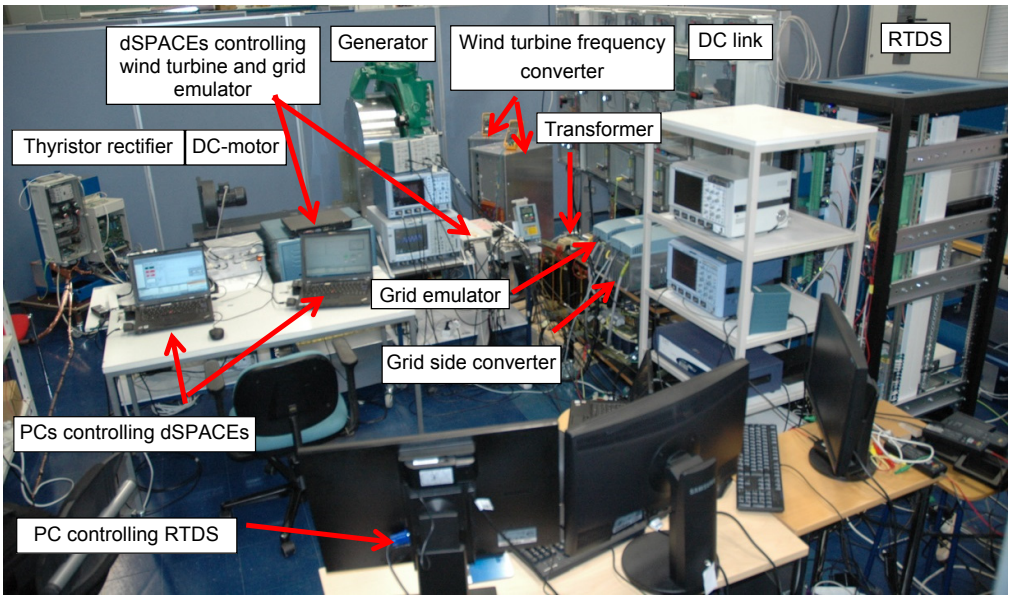

Fig. F.1. Hardware arrangement of the PHIL laboratory test setup.

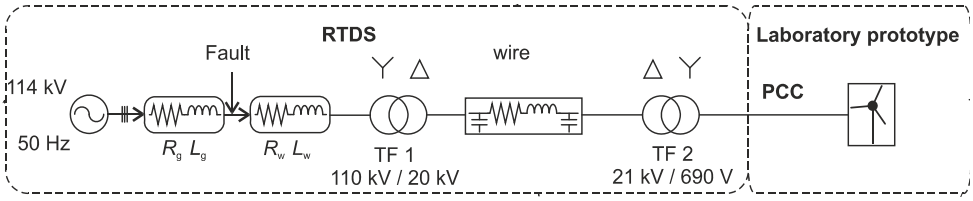

Fig. F.2. Network model.

Table F.1. Wind turbine prototype parameters.

Generator			
p = 12 (pole pairs)	J = 17 kgm^2	n_n = 117 rpm	T_n = 1800 Nm
R_s = 0.22 Ω	$L_d = L_q$ = 9.2 mH	Ψ = 1.2 Wb	
Generator-side converter			
S_n = 10 kVA	f_{sw} = 10 kHz	C_{dc}^{+} = 1.1 mF	C_{dc}^{-} = 1.1 mF
Network-side converter			
S_n = 10 kVA	f_{sw} = 10 kHz	C_{dc}^{+} = 1.1 mF	C_{dc}^{-} = 1.1 mF
DC-link voltage = 750V			
Wind turbine prototype filter			
L_1 = 5 mH	L_2 = 0.6 mH	C_f = 10 μF	R_{damp} = *18* Ω *(parallel with* L_2*)*

Table F.2. Isolation transformer parameters.

S_n = 50 kVA	f_n = 50 Hz	U_1 / U_2 = 400 V / 400 V
L_σ = 0.021 pu	R = 0.043 pu	L_m = 32.4 pu

Table F.3. Grid emulator and NSC parameters.

Grid emulator		
f_{sw} = 10 kHz	S_n = 10 kVA	U_{dc} = 650 V
Network-side converter		
f_{sw} = 3.6 kHz	S_n = 10 kVA	U_{dc} = 650 V
Grid emulator filter		
L_1 = 2.3 mH	C_f = 10 μF	R_{damp} = 2.5 Ω (series with capacitor)

Table F.4. Network model parameters.

Transformer 1 (TF 1)			
S_n = 16 MVA	U_1 / U_2 = 110 / 20 kV	L_σ = 0.109 pu	No load losses = 0.00336pu
Transformer 2 (TF 2)			
S_n = 0.6 MVA	U_1 / U_2 = 21 / 0.69 kV	L_σ = 0.066 pu	No load losses = 0.0005pu
Network impedance			
L_g = 0.1787 H		R_g = 21.19 Ω	
L_w = 0.041 H		R_w = 5.03 Ω	
Wire			
R_{rw} = 2.7 Ω	X_{lw} = 1.9 Ω		B_{cw} = 0.015 mS

Tampereen teknillinen yliopisto
PL 527
33101 Tampere

Tampere University of Technology
P.O.B. 527
FI-33101 Tampere, Finland

ISBN 978-952-15-3978-7
ISSN 1459-2045